Title
Light Transfer Simulation Tools in Photobiological Fuel Production

Author
Lee, Euntaek

Publication Date
2013

University of California

Los Angeles

Light Transfer Simulation Tools in Photobiological Fuel Production

A dissertation submitted in partial satisfaction
of the requirements for the degree
Doctor of Philosophy in Mechanical Engineering

by

Euntaek Lee

2013

ABSTRACT OF THE DISSERTATION

Light Transfer Simulation Tools in Photobiological Fuel Production

by

Euntaek Lee

Doctor of Philosophy in Mechanical Engineering
University of California, Los Angeles, 2013
Professor Prof. Laurent Pilon, Chair

Photobiological carbon dioxide fixation and fuel production have received significant attention in recent years as sustainable solutions to global warming and energy crisis. However, this technology suffers from low production rates, poor solar energy conversion efficiency, and relatively high cost compared with competing technologies. The objective of the present study is to address these limitations by developing efficient and reliable simulation tools to optimize photobiological fuel production systems.

First, an efficient radiative transfer equation (RTE) solver was developed using the discontinuous Galerkin (DG) method and graphics processing units (GPUs). In this study, the RTE solver was validated with benchmark problems related to combustion systems. In addition, this study demonstrated computational benefits of GPUs computing for solving the RTE.

Second, the spectral effective real and imaginary parts of the complex index of refraction of green microalgae *Chlamydomonas reinhardtii* were retrieved from the its experimentally measured radiation characteristics. The microalgae were considered as spherical cells with equivalent diameter distributions. Genetic algorithm and Lorentz-Mie theory were used as inverse and forward method, respectively. In addition, T-matrix was used to predict the radiation characteristics of filamentous cyanobacteria consisting of aligned and connected spheres. This study established that, from a light absorption and scattering point of views, these microorganisms can be treated as infinitely long cylinders with volume-equivalent diameter. The methodology can be used in a wide range of applications and the results can be used to predict the radiation characteristics of PBR suspensions.

Finally, light transfer in photobioreactors (PBRs) containing microalgae *C. reinhardtii* was modeled using the previously developed RTE solver. Then, the light transfer and growth kinetics were combined to estimate the daily biomass productivity of outdoor open ponds, vertical flat-plate PBRs, and tubular PBRs. The effects of growth kinetics models and cellular respiration on daily biomass productivity were investigated. The study demonstrated that the daily productivity per unit of illuminated surface area for PBRs operated in batch mode were identical and depended uniquely on the ratio X_0/a where X_0 is the initial microalgae concentration and a is the illuminated surface area per unit volume of PBR. Similar results were obtained with experimental data and other simulation results reported in the literature, for different microorganisms and PBRs operated in continuous mode. The PBR optical thickness, represented by X_0/a, constitutes a convenient parameter for designing (via a) and operating (via X_0) these PBRs to achieve their maximum performance.

The dissertation of Euntaek Lee is approved.

Prof. Ann Karagozian

Prof. Adrienne Lavine

Prof. Vasilios Manousiouthakis

Prof. Laurent Pilon, Committee Chair

University of California, Los Angeles
2013

Table of Contents

1 Introduction 5

1.1 Photobiological Carbon Dioxide Fixation and Fuel Production . . 5

1.2 Radiation Transfer in Photobioreactors 7

1.2.1 Microbial Light Harvesting Pigments 7

1.2.2 Microorganisms 8

1.2.3 Radiation Transfer 11

1.2.4 Photobioreator Types 12

1.3 Objectives of the Present Study 13

1.3.1 Develop an Integrated Radiation Transfer Solver 13

1.3.2 Measure the Optical Properties of Microalgae 14

1.3.3 Model Coupled Radiation Transfer and Growth Kinetics in Photobioreactors 14

1.4 Organization of the Document 15

2 GPU-Based Radiative Transfer Equation Solver 17

2.1 Introduction 17

2.2 Background 18

2.2.1 Radiative Transfer Equation 18

2.2.2 Gas Radiation Model 19

2.2.3 Discontinuous Galerkin Method For Solving the RTE . . . 22

2.2.4 Graphics Processing Units 24

2.3 Analysis 25

2.3.1 Mathematical Details 25

2.3.2 Matrix-Free Formulation 28
2.3.3 Preconditioner 29
2.4 Validations 31
2.4.1 2D Radiative Transfer in Gray, Emitting, Absorbing, and Non-scattering Media with Black Boundaries Exposed to Diffuse Irradiation 32
2.4.2 2D Radiative Transfer in Non-gray, Emitting, Absorbing, and Non-scattering Media with Black Boundaries Exposed to Diffuse Irradiation 32
2.4.3 3D Radiative Transfer in Non-gray, Emitting, Absorbing, and Non-Scattering Media with Black Boundaries Exposed to Diffuse Irradiation 35
2.4.4 1D Radiative Transfer in Gray, Emitting, Absorbing, and Non-Scattering Media with Reflecting Boundaries Exposed to Diffuse Irradiation 37
2.4.5 2D Radiative Transfer in Gray and Purely Scattering Media with Black Boundaries Exposed to Diffuse Irradiation . . . 39
2.4.6 3D Radiative Transfer in Gray, Emitting, and Absorbing, and Scattering Media with Black and Reflecting Boundaries Exposed to Diffuse Irradiation 41
2.4.7 2D Radiative Transfer in Gray and Purely Scattering Media with Black Boundaries Exposed to Collimated Irradiation . 45
2.5 Speedup of GPU vs. CPU 45
2.6 Conclusions 47
3 Spectral Optical Properties of Spherical Green Microalgae *C. reinhardtii* CC125 and Its Truncated Chlorophyll Antenna Trans-

formants *tla1*, *tlaX*, and *tla1-CW*$^+$ 48

3.1 Introduction 48

3.2 Background 48

3.2.1 Radiation Characteristics of Microalgae 48

3.2.2 Effective Optical Properties of Microorganisms 51

3.3 Analysis 56

3.3.1 Assumptions 56

3.3.2 Equivalent diameter and size distribution 56

3.3.3 Prediction of the Radiation Characteristics of Microalgae . 57

3.3.4 Optimization Algorithm 59

3.3.5 Experimental Uncertainties 61

3.4 Results and Discussion 61

3.4.1 Validation: Retrieving n_λ and d_s of Monodisperse Latex Particles 61

3.4.2 Retrieved Spectral Complex Index of Refraction of Microalgae 63

3.4.3 Discussion 68

3.5 Conclusions 72

4 Radiation Characteristic of Filamentous Microorganisms . . . 73

4.1 Introduction 73

4.2 Background 75

4.2.1 Lorentz-Mie Theory for Infinitely Long Cylinders 75

4.2.2 T-matrix Method for Multiple Connected and Aligned Spheres 77

4.3 Validation 78

4.3.1 Lorentz-Mie theory for Infinitely Long Cylinders 78

4.3.2 T-matrix for Multiple Connected and Aligned Spheres . . 80
4.4 Results and Discussion 81
4.5 Conclusions 83
5 Modeling and Design Guidelines for Outdoor Photobioreactors 84
5.1 Introduction 84
5.2 Background 84
5.2.1 Radiation Transfer in Photobioreactors 84
5.2.2 Method of solution of the RTE 85
5.2.3 Microalgae Growth Kinetics 87
5.2.4 Photobioreactor Modeling 89
5.3 Analysis 92
5.3.1 Problem Statement 92
5.3.2 Assumptions 94
5.3.3 Governing Equations 95
5.3.4 Radiation Characteristics of *C. reinhardtii* 95
5.3.5 Boundary and Initial Conditions 96
5.3.6 Two-Flux Approximation 98
5.3.7 Method of solution 99
5.4 Results and Discussion 102
5.4.1 Open ponds 102
5.4.2 Vertical flat-plate photobioreactor 111
5.4.3 Tubular photobioreactor 115
5.4.4 Comparison of daily biomass productivities 115
5.4.5 Comparison with experimental data and other models . . . 118

5.5 Conclusions 120

6 Conclusions and Recommendations 122

6.1 Summary 122

6.1.1 GPU-Based Radiative Transfer Equation Solver 122

6.1.2 Spectral Optical Properties of Spherical Green Microalgae *C. reinhardtii* CC125 and Its Truncated Chlorophyll Antenna Transformants 123

6.1.3 Radiation Characteristics of filamentous Microorganisms . 123

6.1.4 Modeling and Design Guidelines for Outdoor Photobioreactors 123

6.2 Recommendations for Future Research 124

6.2.1 GPU-Based Radiative Transfer Equation Solver 124

6.2.2 Spectral Optical Properties of Spherical Green Algae *C. reinhardtii* and Its Truncated Chlorophyll Antenna Transformants 125

6.2.3 Radiation Characteristics of Filamentous Microorganisms . 125

6.2.4 Modeling and Design Guidelines for Outdoor Photobioreactors 126

A Spectral Optical Properties Data of microalgae 127

A.1 *Chlamydomonas reinhardtii* CC125 127

A.2 *Chlamydomonas reinhardtii tla1* 128

A.3 *Chlamydomonas reinhardtii tlaX* 129

A.4 *Chlamydomonas reinhardtii* $tla1\text{-}CW^{+}$ 130

References 132

List of Figures

1.1 Illustration of the different biofuels that can be produced by photosynthetic microorganisms (taken from Ref. [1]). 6

1.2 *In vivo* specific absorption coefficient Ea (in m^2/mg) of primary pigments chlorophylls a, b, and c and photosynthetic carotenoids (PSC), and photoprotective carotenoids (PPC) over the spectral region from 400 to 750 nm [2]. 7

1.3 Differential interference contrast and fluorescence micrographs of (a) CC125, (b) *tla1*, (c) *tlaX*, and (d) *tla1-CW*$^+$ (taken from Ref. [3]). 9

1.4 Micrograph image of *A.cylindrica* [4]. 10

1.5 Field demonstration of outdoor photobioreactors (a) open raceway ponds [5], (b) horizontal tubular PBRs [6], (c) vertical flat-plate PBRs [7], and (c) polybag PBRs [8]. 13

1.6 Schematic diagram of the integrated RTE solver developed for simulating outdoor photobioreactors. It indicates each chapter of this thesis describing a specific aspect of this integrated simulation tool. 16

2.1 Non-zero elements for the $(N \times N_p) \times (N \times N_p)$ matrix of a radiative transfer problem with P-3 DG scheme ($N_p = 20$). The grid mesh consists of N = 86 tetrahedron elements (a) full matrix, and (b) close-up view of the matrix. 30

2.2 Comparison of simulation results with Ref. [9] of a 2D 1.0 m × 0.5 m rectangular enclosure with cold and black side walls containing a gas at uniform temperature of 1000 K and uniform absorption coefficient $\kappa = 0.5$ m^{-1}, (a) and (b) heat flux along boundary walls in the x- and y- directions, respectively, and (c) and (d) divergence of radiative heat flux along the center lines in the x- and y- directions, respectively. 33

2.3 Comparison of predicted wall heat flux using SLW and SNBCK gas radiation models in a 2D rectangular enclosure with those reported in Ref. [9]. The enclosure contained H_2O and CO_2 in moral fractions 0.2 and 0.1, respectively. The wall were cold and black walls. The gas temperature was non-uniform and given by Equation (2.25). 34

2.4 Comparison of simulated (a) radiative heat flux along the centerline of a sidewall (x = -1.0, y = 0, z) and (b) divergence of radiative heat flux along the centerline (x = 0, y = 0, z) for a 3D rectangular enclosure containing absorbing, emitting, and non-scattering gas mixture at a specified temperature [Equation (2.26)] with SNBCK gas model and different DG order (P-1, P-2, and P-5), grid size ($\Delta x = \Delta y = \Delta z$), and angular quadratures (S_8 and T_4) with that reported in Ref [10]. 36

2.5 Comparison of divergence of dimensionless radiative heat flux [Equation (2.1)] between DG method solution and the exact solution [11] for 1D absorbing and emitting gray gas at $T_g = 1500$ K with gray diffusely reflecting and emitting walls at $T_w = 500$ K with $\epsilon = 0.5$. The medium optical thickness was (a) $\tau_L = 0.1$, (b) $\tau_L = 1.0$, and (c) $\tau_L = 10.0$. 38

2.6 (a) Dimensionless heat flux $q^*(0.5, y)$ and (b) fluence rate $G^*(0.5, y)$ along the y-axis for center of x-axis in a 2D enclosure containing purely scattering media with isotropic, strongly forward (F1 and F2), and strongly backward (B1 and B2) scattering phase functions. The results are compared with previously reported studies [12, 13] obtained using finite volume method and DOM. Here, $q^*(x, y) = q(x, y)/E_{bw}$ and $G^*(x, y) = G(x, y)/4E_{bw}$. 40

2.7 Geometry, dimension, and simulation results of the net radiative heat flux on the front, side, and back walls of a 3D combustor chamber [14] with absorbing, emitting, (a) non-scattering medium ($\omega = 0.0$) and (b) scattering medium ($\omega = 0.5$). All dimensions are in meter. 42

2.8 Dimensionless radiative heat flux along (a) the bottom wall $q^*(r/R, 0)$ and (b) along the sidewall of the cylindrical enclosure $q^*(R, z/2H)$ with R = H = 1 m containing cold, absorbing, and isotropically scattering medium exposed to collimated radiation incident from the top wall. Case 1 is such that $\epsilon_s = 1.0$, $\kappa = 0.0$ m^{-1}, and $\sigma_s = 1.0$ m^{-1}. Case 2 is such that $\epsilon_s = 0.5$, $\kappa = 0.3$ m^{-1}, and $\sigma_s = 0.7$ m^{-1} [15]. 44

2.9 Speedup of GPU vs. CPU implementation as a function of DG order for a 3D radiative transfer problem in gray, absorbing, emitting, and non-scattering medium at the prescribed temperature field with $\kappa = 0.1$ m^{-1}. Grid 1 and grid 2 consisted of 2,861 and 22,655 tetrahedron elements, respectively. 46

3.1 Number frequency $f(d_s)$ of the equivalent sphere diameter of (a) *C.reinhardtii* CC 125 (c=0.989, ϵ=1.149) and its truncated chlorophyll antenna transformants (b) *tla1* (c=0.996, ϵ=1.073), (c) *tlaX* (c=0.979, ϵ=1.220), and (d) *tla1-CW*$^+$ (c=0.986, ϵ=1.173). The equivalent diameter was estimated from Equation (3.6) and major and minor diameter distributions reported in Figure 2 in Ref. [3]. 55

3.2 Block diagram of the procedure used to retrieve the refraction index n_λ and absorption index k_λ from the absorption and scattering cross-sections $\bar{C}_{abs,\lambda}$ and $\bar{C}_{sca,\lambda}$ at a given wavelength λ for number frequency $f(d_s)$. Individuals N=120 per generation for a maximum of 50 generations were used. n_λ and k_λ were allowed to range from 1.33 to 1.53 and from 10^{-5} to 0.01, respectively. 60

3.3 Comparison of the retrieved refraction and absorption indices between 400 and 750 nm for the green algae *C.reinhardtii* CC 125 using major, minor, and equivalent diameter distributions $f(a)$, $f(b)$, and $f(d_s)$, respectively. 64

3.4 Comparison of the retrieved refraction and absorption indices between 400 and 750 nm for the green algae *C.reinhardtii* CC 125 and its truncated chlorophyll antenna transformants *tla1*, *tlaX*, and *tla1-CW*$^+$ using their number frequency $f(d_s)$. 66

3.5 Comparison of the predicted and experimentally measured [3] average spectral absorption $\bar{C}_{abs,\lambda}$ and scattering $\bar{C}_{sca,\lambda}$ cross-sections of the green algae *C.reinhardtii* CC 125 and its truncated chlorophyll antenna transformants *tla1*, *tlaX*, and *tla1-CW*$^+$. Experimental data [3] for $\bar{A}_{abs,\lambda}$ and $\bar{S}_{sca,\lambda}$ were converted to $\bar{C}_{abs,\lambda}$ and $\bar{C}_{sca,\lambda}$ using Equations (3.10) and (3.11), respectively. 67

3.6 Comparison between the retrieved absorption index k_λ and those predicted by Equation (3.4) for *C.reinhardtii* with $w_a = 16.50$ g/kg, $w_b = 9.68$ g/kg, and $w_{PPC} = 1.98$ g/kg. 69

3.7 Comparison of the prediction by T-matrix and experimental measurement [3] for average spectral absorption $\bar{C}_{abs,\lambda}$ and scattering $\bar{C}_{sca,\lambda}$ cross-sections of the green algae *C.reinhardtii* CC 125. Experimental data [3] for $\bar{A}_{abs,\lambda}$ and $\bar{S}_{sca,\lambda}$ were converted to $\bar{C}_{abs,\lambda}$ and $\bar{C}_{sca,\lambda}$ using Equations (3.10) and (3.11), respectively. 71

4.1 Micrographs of (a) filamentous cyanobacteria *A.cylindrica* [4] and (b) filamentous cyanobacteria *A.variabilis* grown in our laboratory [16]. 74

4.2 Scattering of incident radiation at incident angle of ϕ by a infinitely long cylinder [17]. 75

4.3 Scattering phase function for randomly oriented infinitely long cylinders as a function of the scattering angle for two test cases (1) $m = 1.507 + i0.0$ and $\chi = 6.283$ and (2) $m = 1.05 + i1.08$ and $\chi = 0.684$. 79

4.4 Scattering and absorption cross-sections $\langle C'_{sca}\rangle \, and \, \langle C'_{abs}\rangle$ per unit length (in m) for randomly oriented multiple connected and aligned spheres as a function of the number of spheres N and for infinitely long cylinders of volume-equivalent radius for (a, b) $\chi = 0.01$, (c, d) $\chi = 0.1$, and (e, f) $\chi = 1.0$. 82

5.1 Schematic of the (a) open pond, (b) vertical flat-plate, and (c) tubular photobioreactors simulated in this study along with coordinate systems. 93

5.2 (a) Schematic of the daily solar trajectory in the Los Angeles sky on June 21 and (b) collimated $G_{in,c,\lambda}$ and diffuse $G_{in,d,\lambda}$ solar irradiance spectrum over the PAR at 12:00 pm. 97

5.3 Total specific growth rate μ of *C. reinhardtii* as function of the local fluence rate $G_{PAR}(\mathbf{r})$ measured experimentally [18, 19] and predicted by Equations (5.10) and (5.11) with parameters $\mu_0 = 0.2274$ hr^{-1}, $\mu_s = 0.032$ hr^{-1}, $K_S = 81.38$ μmol photon m$^{-2}\cdot$ s^{-1}, and $K_I = 2500$ μmol photon m$^{-2}\cdot$ s^{-1}. 101

5.4 Computed PAR-averaged local fluence rate $G_{PAR}(\mathbf{r})$ on June 21 at 8:00 am, 10:00 am, 12:00 pm, 2:00 pm, and 4:00 pm in the midplane of an open pond located in Los Angeles, USA (34.04°N, 118.15°W) having diameter $D = 2$ m and depth $L = 0.1$ m with (a) black walls or (b) reflecting walls for initial mass concentration $X_0 = 0.1$ kg/m^3.104

5.5 PAR-averaged local fluence rate $G_{PAR}(\mathbf{r})$ predicted on June 21 in Los Angeles, USA (34.04°N, 118.15°W) at 8:00 am, 12:00 pm, and 4:00 pm in the centerline of an open pond PBR predicted by (i) DG method with DOS-ISW, (ii) two-flux approximation [Equation(5.5)], and (iii) simplified two-flux approximation [Equation(5.26)]. The pond featured black or reflecting walls and had diameter $D = 2$ m and depth $L = 0.1$ m for initial mass concentration $X_0 = 0.1$ kg/m^3. 105

5.6 Comparison of (a, b) the average specific growth rate $\bar{\mu}$ and (c, d) *C. reinhardtii* mass concentration ratio $X(t)/X_0$ as a function of time without and with respiration for initial mass concentration X_0 between 0.05 and 1.0 kg/m^3. The open pond was of depth $L = 0.1$ m located in Los Angeles, USA (34.04°N, 118.15°W) on June 21 and had black walls. 107

5.7 Comparison of (a) the average specific growth rate $\bar{\mu}$ [Equation(5.12)] and $\bar{\mu}'$ [Equation(5.14)] and (b) the corresponding mass concentrations $X(t)$ for open pond with depth $L = 0.1$ m and initial mass concentration $X_0 = 0.1$ and 1.0 kg/m^3 located in Los Angeles, USA (34.04°N, 118.15°W) on June 21 and having black walls. 108

5.8 Comparison of daily areal biomass productivity per unit footprint $P_{f,op}$ of open pond with black walls growing *C. reinhardtii* as function of X_0L without and with in Los Angeles, USA (34.04°N, 118.15°W) on June 21. 110

5.9 Computed PAR-averaged local fluence rate $G_{PAR}(\mathbf{r})$ at 8:00 am, 10:00 am, 12:00 pm, 2:00 pm, 4:00 pm, and 6:00 pm with refraction by the walls in the midplane of a vertical flat-plate located in Los Angeles, USA (34.04°N, 118.15°W) having height $H = 2$ m, width $W = 2$ m, and thickness $L = 0.1$ m with initial mass concentration $X_0 = 0.1$ kg/m^3 on June 21. 113

5.10 PAR-averaged local fluence rate $G_{PAR}(\mathbf{r})$ at 10:00 am, 2:00 pm, and 6:00 pm in the centerline of a vertical flat-plate located in Los Angeles, USA (34.04°N, 118.15°W) predicted by (i) DG method with DOS-ISW, (ii) two-flux approximation [Equation (5.21)], and (iii) simplified two-flux approximation [Equation (5.24)]. The vertical flat-plate (a) without and (b) with refraction by the walls had height $H = 2$ m, width $W = 2$ m, and thickness $L = 0.1$ m with initial mass concentration $X_0 = 0.1$ kg/m^3. $G_{PAR}(\mathbf{r})$ was predicted on June 21. 114

5.11 Computed local PAR-averaged fluence rate $G_{PAR}(\mathbf{r})$ at 8:00 am, 10:00 am, 12:00 pm, 2:00 pm, 4:00 pm, and 6:00 pm in the cross-section of a north-south oriented tubular photobioreactor located in Los Angeles, USA (34.04°N, 118.15°W) having diameter $L = 0.1$ m with initial mass concentration $X_0 = 0.1$ kg/m^3 on June 21. . . 116

5.12 Daily areal biomass productivity per unit illuminated surface area exposed to collimated solar irradiance predicted on June 21 in Los Angeles for open ponds P_{op}, vertical flat-plate PBRs P_{fp}, and tubular PBRs P_{tb} for *C. reinhardtii* as function of X_0a^{-1} with depth or diameter L varying from 0.05 to 1.0 m and initial concentration X_0 between 0.1 and 5.0 kg/m^3. Here, $a_{op} = 1/L$, $a_{fp} = 1/L$, and $a_{tb} = 2/L$. 117

5.13 (a) Experimentally measured and predicted daily areal biomass productivity as a function of X_0a^{-1} [20] for continuous vertical air-lift flat-plate PBR of thickness L equals to 3 or 5.5 cm with *N. oleoabundans*. (b) Collapse of the predicted yearly volumetric biomass productivity shown in Fig. 3 in Ref. [21] plotted as function of X_0a^{-1} for 1 m tall vertical flat-plate PBRs in continuous operation with L varying from 0.05 to 0.1 m and X_0 between 1.0 and 13.0 kg/m^3 for *P. tricornutum* and *T. pseudonana*. 119

List of Tables

4.1 Comparison between the results reported in Ref. [17] and those predicted in this study for the extinction efficiency factor of randomly oriented and infinitely long cylinders with complex index of refraction $m = 2.0 + i0.2$ in vacuum and different size parameters. 78

4.2 Comparison of the absorption and scattering efficiency factors obtained from the T-matrix code for multiple connected and aligned spheres [22] and from the code for bispheres [23] for two connected spheres with size parameters $\chi = 0.01$, 0.1, 1.0, and 10.0. 80

A.1 Spectral Optical Properties Data of *Chlamydomonas reinhardtii* CC125 in the spectral range from 400 to 750 nm. 127

A.2 Spectral Optical Properties Data of *Chlamydomonas reinhardtii* *tla1* in the spectral range from 400 to 750 nm. 128

A.3 Spectral Optical Properties Data of *Chlamydomonas reinhardtii* *tlaX* in the spectral range from 400 to 750 nm. 129

A.4 Spectral Optical Properties Data of *Chlamydomonas reinhardtii* *tla1-CW*$^+$ in the spectral range from 400 to 750 nm. 130

ACKNOWLEDGMENTS

I would like to express my sincere gratitude to my advisor Prof. Laurent Pilon for all his guidance, support, and encouragement during my doctoral studies. He always helped me in my research with his knowledge, enthusiasm, and patience. I would like to express my appreciation to Prof. Ann Karagozian, Prof. Adrienne Lavine, and Prof. Vasilios Manousiouthakis for their contributions as members of my committee. Moreover, I would like to thank Dr. Xing He and Dr. Ramakanth Munipalli for sharing their expertise of numerical methods and GPU computing. I would like to thank Prof. Michael F. Modest and Prof. Jérémy Pruvost for their helpful comments and feedback on my study. I am grateful to Ri-Liang for helpful discussions and assistance.

I also acknowledge my colleagues for their contribution of my works as co-authors. Chapter Two is a version of X. He, E. Lee, L. Wilcox, R. Munipalli, and L. Pilon, 2013. “A High-Order Accurate GPU-Based Radiative Transfer Equation Solver for Combustion and Propulsion Applications”, *Numerical Heat Transfer, Part B: Fundamentals.* Chapter Three is a version of E. Lee, R.-L. Heng, and L. Pilon, 2013. “Spectral optical properties of selected photosynthetic microalgae producing biofuels”, *Journal of Quantitative Spectroscopy and Radiative Transfer*, vol. 114, pp. 122-135. Chapter Five is a version of E. Lee, J. Pruvost, X. He, R. Munipalli, and L. Pilon, “Modeling and Design Guidelines for Outdoor Photobioreactors”, *Biotechnology Progress* recently submitted for publication.

During my studies at UCLA, I had the chance to make friends with many great individuals. I am grateful to all my friends for sharing enjoyable moments.

Finally, I would like to dedicate this dissertation to my parents and sister for all their love.

VITA

1998–2004	B.S. (Mechanical Engineering), Chung-Ang University, Seoul, Korea.
2005–2007	M.S. (Mechanical Engineering), Korea Advanced Institute of Science and Technology, Daejeon, Korea.
2008–present	Graduate Student (Mechanical Engineering), University of California, Los Angeles.

PUBLICATIONS

K. Kim, **E. Lee**, and T.-H. Song, 2008. "Discrete Ordinates Interpolation Method for Radiative Heat Transfer Problems in Three-Dimensional Enclosures filled with Non-gray or Scattering Medium", *Journal of Quantitative Spectroscopy and Radiative Transfer*, vol. 109, pp. 2579-2589.

E. Lee, R.-L. Heng, and L. Pilon, 2013. "Spectral optical properties of selected photosynthetic microalgae producing biofuels", *Journal of Quantitative Spectroscopy and Radiative Transfer*, vol. 114, pp. 122-135.

X. He, **E. Lee**, L. Wilcox, R. Munipalli, and L. Pilon, 2013. "A High-Order Accurate GPU-Based Radiative Transfer Equation Solver for Combustion and Propulsion Applications", *Numerical Heat Transfer, Part B: Fundamentals* (accepted).

R. Kandilian, **E. Lee**, and L. Pilon, “Radiation and Optical Properties of *Nannochloropsis oculata* Grown Under Different Irradiances and Spectra”, *Bioresource Technology* (Under review).

E. Lee, J. Pruvost, X. He, R. Munipalli, and L. Pilon, “Modeling and Design Guidelines for Outdoor Photobioreactors”, *Biotechnology Progress* (Under review).

NOMENCLATURE

A	area, m^2
C	cross section, m^2/mole
E	emissive power, W/m^2
F	blackbody distribution function
G	fluence rate, W/m^2
g	Henyey-Greenstein asymmetric factor
g	cumulative distribution function of absorption
H	height, m
I	radiation intensity, W/m^2 sr
I_b	blackbody radiation intensity, W/m^2 sr
k	absorption coefficient variable, m^{-1}
L	thickness, m
l	test function in DG method
P	pressure, Pa
q	heat flux, W/m^2
R	radius, m
s	path length, m
T	temperature, K
V	volume, m^3
x, y, z	cartesian coordinates, m
Y	molar fraction
$\mathbf{r}$	position vector, m
E_a	*in vivo* specific spectral absorption coefficient, m^2/kg
C	mass concentration, m^2/kg
x_w	volume fraction of water in the cell
w	dry mass fraction of pigment

d_s	equivalent sphere of diameter, μm
n	refractive index
k	absorption index
T	Transmittance
C_c	intracellular carbon concentration, kg/m^3
p'	absorption thickness parameter
a	major diameter, μm
b	minor diameter, μm
N	the number of cells per unit volume of suspension
N_T	total number of cells per unit volume of suspension
c	circularity
A_S	cell's surface area, m^2
P	cell's perimeter, m
f	number frequency
C_{abc}	absorption cross-section, m^2
C_{sca}	scattering cross-section, m^2
A_{abc}	mass absorption cross-section, m^2/kg
S_{sca}	mass scattering cross-section, m^2/kg
X	mass concentration of microorganism, kg/m^3
V_{32}	mean particle volume, m^3
$T(\theta)$	amplitude function
i	angular distribution of the scattered intensity
m	complex index of refraction
r	radius, m
Q_{abc}	absorption efficiency factor
Q_{sca}	scattering efficiency factor
I	radiation intensity, W/m^2 sr
r	location, m

s	direction
G	fluence rate, W/m^2
b	backward scattering fraction
K_S	light half-saturation constant, μmol photon m$^{-2}\cdot$ s^{-1}
K_I	light inhibition constants, μmol photon m$^{-2}\cdot$ s^{-1}
P	areal productivity, kg/m^2/day
t	time, hr
a	specific illuminated area, m

Greek symbols

β	extinction coefficient, m^{-1}
ϵ	emmisivity
θ, ϕ	spherical coordinate
κ	absorption coefficient, m^{-1}
σ	Stefan-Boltzmann constant, W/m^2 K^4
σ_s	scattering coefficient, m^{-1}
τ	optical thickness
Φ	scattering phase function
Ω	solid angle, sr
ω	scattering albedo
ρ_{dm}	density of dry material in the biomass, kg/m^3
χ	size parameter
λ	wavelength
ϵ	aspect ratio
δ	objective function
μ	specific growth rate, hr^{-1}

Subscripts

abs	absorption
b	blackbody

$ext.$	external
g	gas
$int.$	internal
i, j	absorption coefficient indices
n, m	grid element indices
p	order of DG method
w	wall
ν	wavenumber
PAR	photosynthetically active radiation region
av	average
in	incident
c	collimated
d	diffuse

CHAPTER 1

Introduction

The present study aims to develop an efficient radiation transfer equation solver and to model coupled light transfer and growth kinetics in photobioreactors to design and optimize photobiological fuel production systems. This chapter presents the motivations of this study and describes the organization of the document.

1.1 Photobiological Carbon Dioxide Fixation and Fuel Production

Microalgae have received significant attention in recent years as a way (i) to fixate CO_2 generated during fossil fuel combustion and (ii) to produce liquid or gaseous biofuels [24] as well as (iii) food supplement [25] or (iv) protein for human or animal feed [26]. Increasing concentration of carbon dioxide in the atmosphere caused by fossil fuel combustion due to human activity has contributed to world climate change [27]. To address this problem, photobiological CO_2 mitigation is being considered as an economically feasible and environmentally sustainable solution [28]. It consists of consuming CO_2 in the atmosphere or in flue gases by plants and microorganisms using photosynthesis. Figure 1.1 shows the different possible compounds that can be produced by providing light and CO_2 to photosynthetic microorganisms [1]. For example, microalgae have larger photosynthetic efficiency than higher plants (e.g., trees or sugar cane) [29]. Therefore, they possess a greater ability to fixate CO_2 and produce biomass [28]. The concentration of CO_2 in the

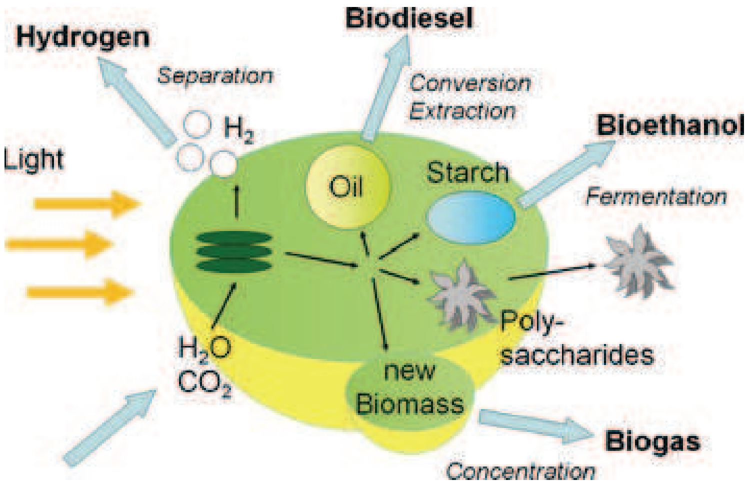

Figure 1.1: Illustration of the different biofuels that can be produced by photosynthetic microorganisms (taken from Ref. [1]).

atmosphere is relatively small (∼400 ppm) and may not be sufficient to maintain the microalgal growth [28]. However, exhaust gases from combustion processes contain more than 15 vol.% of CO_2. This CO_2 source could provide sufficient amounts of CO_2 for large-scale production of microalgae [28]. Therefore, direct utilization of power plant flue gases is a promising method to grow microalgae while consuming CO_2.

Photosynthetic microorganisms use sunlight as their energy source, CO_2 as their carbon source, and water as their electron source. They are typically grown in open ponds and photobioreactors (PBRs) of various designs where sunlight is absorbed and scattered by the microorganisms kept in suspension by stirring and/or bubble sparging [30]. To be economically viable, the production of added-value products requires the highest microorganisms production rate and efficiency. Open ponds or PBRs can be operated in batch or continuous processes. Batch cultures are widely used for their simplicity, flexibility, and low cost [31]. Scaling-up benchtop PBRs to industrial scale remains a challenge [1]. Indeed, optimum

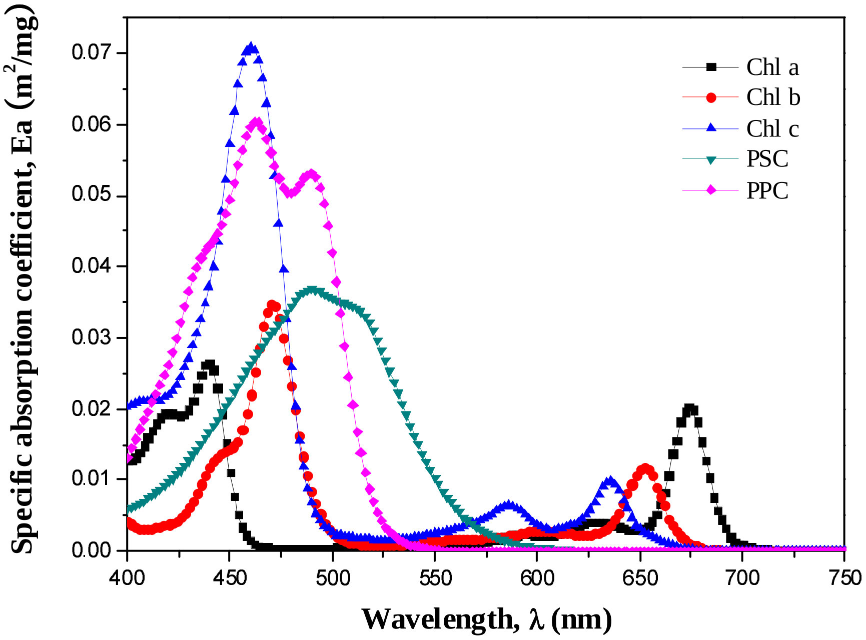

Figure 1.2: *In vivo* specific absorption coefficient Ea (in m^2/mg) of primary pigments chlorophylls a, b, and c and photosynthetic carotenoids (PSC), and photoprotective carotenoids (PPC) over the spectral region from 400 to 750 nm [2].

temperature, mixing, light and mass transfers should be maintained in photobioreactors of any sizes [32]. In particular, sunlight available in photobioreactors is an important parameter that determines the efficiency of PBRs. It affects the microorganisms growth rate and the efficiency of the production process. Current photobioreactors must be improved in order to achieve larger mass concentrations and growth rate and to minimize auxiliary energy use and capital cost [33].

1.2 Radiation Transfer in Photobioreactors

1.2.1 Microbial Light Harvesting Pigments

Photosynthesis begins with the absorption of photons by the photosynthetic apparatus which consists of three major components (i) the reaction center, (ii) the core antenna, and (iii) the peripheral antenna. Photochemical charge separation and electron transport take place in the reaction center [34]. The core antenna contains the photosynthetic pigments chlorophylls or bacteriochlorophylls. It is surrounded by the peripheral antenna which is an assembly of chlorophylls, bacteriochlorophylls, and other accessory pigments such as carotenoids and phycobiliproteins. The peripheral antenna is particularly important in channeling additional photon energy to the reaction center at small light intensities. In microalgae and cyanobacteria, the photosynthetic apparatus is located on the photosynthetic membrane called thylakoid [35].

Different pigment molecules absorb over different spectral bands of the visible and near infrared parts of the spectrum enabling more efficient utilization of solar energy. Figure 1.2 shows the *in vivo* specific absorption coefficient Ea (in m^2/mg) of primary pigments chlorophylls a, b, and c as well as accessory pigments such as photosynthetic carotenoids (PSC), and photoprotective carotenoids (PPC) measured over the spectral region from 400 to 750 nm [2]. It indicates that Chlorophyll a (Chl a) absorbs around 435 and 676 nm while Chlorophyll b (Chl b) absorbs around 475 and 650 nm. Since they do not absorb green light ($\lambda \approx$ 520-570 nm) significantly, these microalgae appear green to the human eye. On the other hand, carotenoids are accessory pigments found in all photosynthetic microorganisms. They absorb mainly in the blue part of the spectrum (400 nm $\leq \lambda \leq$ 550 nm) [34]. Carotenoids serve two major functions (i) shielding the photosynthetic apparatus from photo-oxidation under large light intensities and (ii) increasing the solar light utilization efficiency by expanding the absorption spectrum of the microorganism.

1.2.2 Microorganisms

Microorganisms include unicellular and colonial species. They may assume different shapes e.g., spheres, spheroids, and filamentous and various sizes (1–10 μm) [36]. Their shapes and sizes are determined to serve different functions such

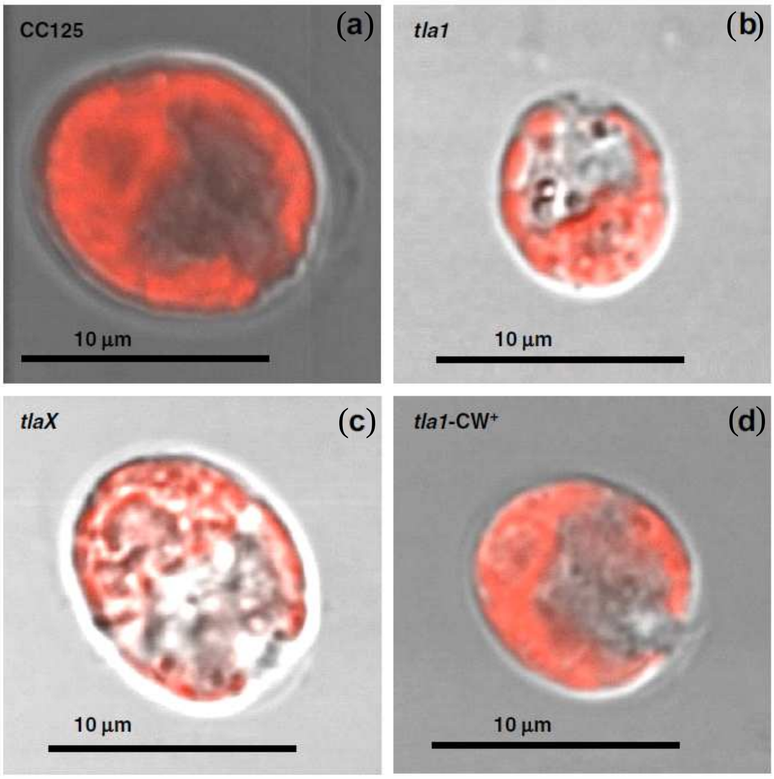

Figure 1.3: Differential interference contrast and fluorescence micrographs of (a) CC125, (b) *tla1*, (c) *tlaX*, and (d) *tla1-CW*$^+$ (taken from Ref. [3]).

as control of settling, nutrients transfer, and collection of sunlight for photosynthesis [36]. The particular species are of interest in this study namely (i) the given microalgae *Chlamydomonas reinhardtii* and (ii) filamentous cyanobacteria *Anabaena cylindrica*.

Figure 1.3 shows *in vivo* differential interference contrast (DIC) and chlorophyll fluorescence micrographs of the green microalgae *Chlamydomonas reinhardtii* strain CC125 and its truncated chlorophyll antenna transformants *tla1*, *tlaX*, and *tla1-CW*$^+$ [3]. *C. reinhardtii* is a unicellular green algae of a spheroidal shape with average diameter around 10 μm. It is one of the best candidates for photobiological hydrogen production as it can produce only H_2 by reversibly shutting down its O_2 production metabolism by sulphur deprivation [37]. They can also

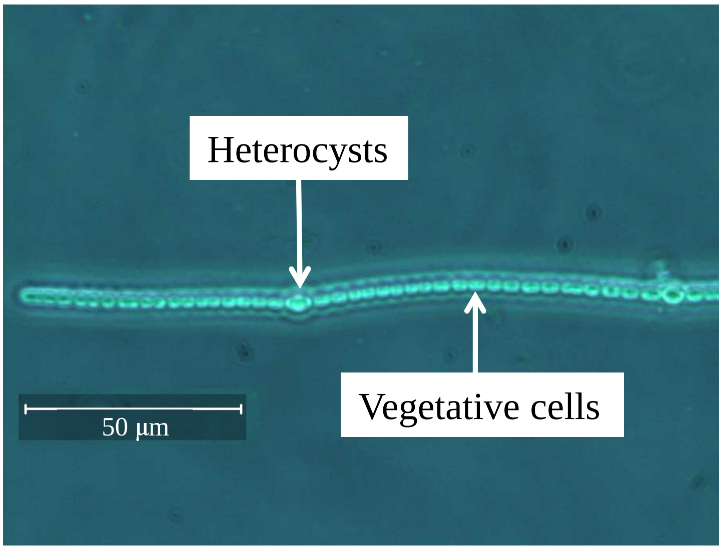

Figure 1.4: Micrograph image of *A.cylindrica* [4].

be genetically modified with truncated light harvesting chlorophyll antenna. In fact, Polle *et al.* [38] genetically engineered *C.reinhardtii* via DNA insertional mutagenesis to obtain the mutant strain *tla1* with permanently reduced number of chlorophyll molecules per photosystem, i.e., truncated light harvesting chlorophyll antenna. This strain did not contain cell wall [38]. However, cell walls protect the cells from excessive shear stress such as that observed in photobioreactors, for example [38]. Thus, Polle *et al.* [38] crossed *tla1* with a cell wall containing strain and isolated the strain $tla1\text{-}CW^{+}$ showing observable characteristics (phenotype) of *tla1* but with a cell wall. In addition, the strain *tlaX* had even a smaller chlorophyll antenna than *tla1*. Finally, the authors reported that the microorganisms with less pigments had higher quantum yield, photosynthesis rate, and light saturation irradiance [38]. *C. reinhardtii* contains Chl *a* and Chl *b* and photoprotective carotenoids (PPC) [39]. Pottier *et al.* [39] measured their mass fraction by acetone extraction and optical density measurements as 1.4 wt.%, 0.7 wt.%, and 0.45 wt.%, respectively.

Moreover, Figure 1.4 shows a micrograph of the cyanobacteria *Anabaena cylin-*

drica [4]. Its filamentous structure is more than 100 μm long. Each filament consists of dozens of connected aspherical heterocysts and vegetative cells, each 2-4 μm in diameter. *A.cylindrica* contains Chl *a* and Chl *b*, accessory pigments phycocyanin (PCCN), and photoprotective or photosynthetic carotenoids (PPC or PSC). It is able to fixate nitrogen and to produce ammonia using its heterocysts [40]. It can also be used to purify contaminated waters by removing nitrates and phosphates and to produce fertilizers by fixating atmospheric nitrogen [41]. *A.cylindrica* can produce hydrogen using photosynthesis under nitrogen-starved conditions. It is also considered for biofuel production because of its large cell structure which requires less energy during harvesting.

1.2.3 Radiation Transfer

Solar radiation is the energy source driving the metabolic activity of photosynthetic microorganisms. As light penetrates in the photobioreactor, it is absorbed and scattered by the microorganisms. Light transfer in photobioreactors is governed by the radiative transfer equation (RTE). The latter is an energy balance on the radiative energy traveling along a particular direction $\hat{s}$ and is expressed as [42]

$$\begin{aligned}\hat{\mathbf{s}} \cdot \nabla I_\lambda(\mathbf{r}, \hat{\mathbf{s}}) = \kappa_\lambda(\mathbf{r}) I_{b\lambda}(\mathbf{r}, \hat{\mathbf{s}}) - \kappa_\lambda(\mathbf{r}) I_\lambda(\mathbf{r}, \hat{\mathbf{s}}) - \sigma_{s\lambda}(\mathbf{r}) I_\lambda(\mathbf{r}, \hat{\mathbf{s}}) + \\ \frac{\sigma_{s\lambda}(\mathbf{r})}{4\pi} \int_{4\pi} I_\lambda(\mathbf{r}, \hat{\mathbf{s}}) \Phi_\lambda(\hat{\mathbf{s}}_i, \hat{\mathbf{s}}) d\Omega_i \quad (1.1)\end{aligned}$$

where κ_λ (in m^{-1}) is the spectral absorption coefficient, $\sigma_{s\lambda}$ (in m^{-1}) is the spectral scattering coefficient, $I_\lambda(\mathbf{r}, \hat{\mathbf{s}})$ is the radiation intensity at location $\mathbf{r}$ in direction $\hat{\mathbf{s}}$ expressed in W/m$^2\cdot$ sr $\cdot$ cm, $I_{b\lambda}$ is the blackbody radiation intensity given by Planck's law. The scattering phase function $\Phi_\lambda(\hat{\mathbf{s}}_i, \hat{\mathbf{s}})$ represents the probability that radiation propagating in the solid angle $d\Omega_i$ direction around $\hat{\mathbf{s}}_i$ be scattered into the solid angle $d\Omega$ around the direction $\hat{\mathbf{s}}$. In addition, β_λ (=$\sigma_{s\lambda} + \kappa_\lambda$) is the spectral extinction coefficient while the single scattering albedo is defined as

$\omega_\lambda = \sigma_{s\lambda}/(\sigma_{s\lambda} + \kappa_\lambda)$.

The absorption and scattering coefficients of microalgae and their scattering phase function are major parameters needed to solve the RTE for simulating, designing, scaling-up, optimizing, and controlling photobioreactors [24]. These characteristics are strongly dependent on wavelength and vary from one species to another. They can be determined either experimentally [3,43] or based on electromagnetic wave theory [39]. This latter approach often assumes that the scatterers have relatively simple shape (e.g., spherical) and ignore their heterogeneous nature by attributing them a uniform effective complex index of refraction [44,45]. Pottier *et al.* [39] recognized that for complex microorganisms shapes (e.g., cylinders and spheroids), advanced numerical tools are required to predict their absorption and scattering coefficients and scattering phase function collectively called radiation characteristics. On the other hand, experimental measurements account for the actual shape, morphology, and size distribution of the microorganisms [24]. However, experimental setups can be expensive and measurements are time consuming.

1.2.4 Photobioreator Types

Photobioreactors can be categorized into three main groups namely (i) open outdoor systems, (ii) closed outdoor systems, and (iii) closed indoor systems [46]. Figure 1.5 shows various types of outdoor photobioreactors including (a) open raceway ponds [5], (b) horizontal tubular PBRs [6], (c) vertical flat-plate PBRs [7], and (c) polybag PBRs [8]. The construction and operating costs of these different PBRs vary widely. The type of photobioreactors is selected based on the microorganisms and the compounds they can produce. Closed systems are characterized by better control of the operating conditions and are less susceptibility to contamination as opposed to open systems. Therefore, closed systems are more suitable for producing valuable products such as pharmaceuticals and pigments [47]. Open

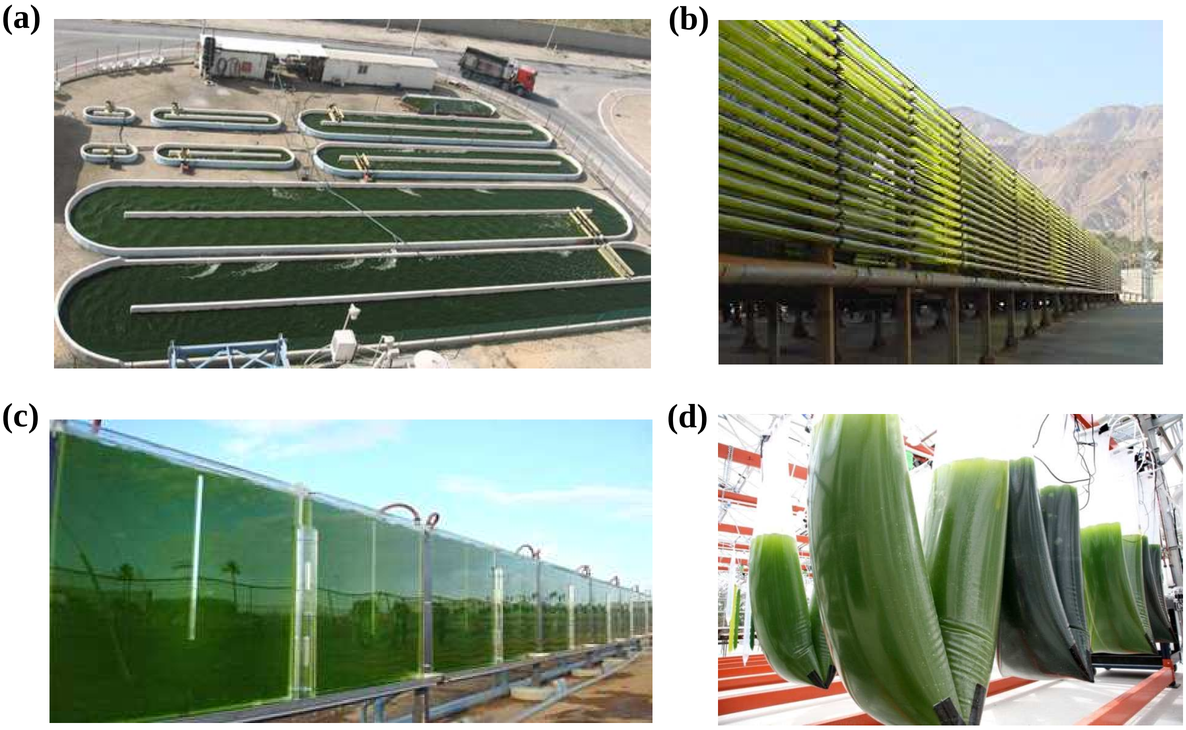

Figure 1.5: Field demonstration of outdoor photobioreactors (a) open raceway ponds [5], (b) horizontal tubular PBRs [6], (c) vertical flat-plate PBRs [7], and (c) polybag PBRs [8].

systems are more economical and easier to construct over large surface areas and to operate than closed systems. Thus, open outdoor systems seem to be the most promising for large scale microalgae production [32, 48].

1.3 Objectives of the Present Study

The objective of this study are discussed in the following sections.

1.3.1 Develop an Integrated Radiation Transfer Solver

This study aimed to develop a fast, robust, and accurate RTE solver implementing high-order discontinuous Galerkin (DG) method based on graphics processing units (GPUs) computing. It was used to simulate light transfer in photobioreactors [24]. It could also be useful in military and aerospace applications related to thermal analysis of combustion and propulsion systems as well as target detection and identification (remote sensing) [42]. It could also be used in the analysis of exhaust gases in stationary power plants [49], and of furnaces to minimize energy loss and pollution emissions [50].

1.3.2 Measure the Optical Properties of Microalgae

The second objective of this study was to retrieve the real part (or refraction index) and imaginary part (absorption index) of the complex index of refraction of microalgae from experimentally measured size distribution and absorption and scattering cross-sections [3, 51]. The results can be enable the prediction of the radiation characteristics of microalgae from first principles instead of carrying out costly and time consuming experiments. It also provides a comprehensive and integrated tools to accurately simulate PBRs. The green algae *Chlamydomonas reinhardtii* strain CC125 and its truncated chlorophyll antenna transformants *tla1*, *tlaX*, and *tla1-CW*$^+$ [3] as well as filamentous cyanobacteria such as *A.cylindrica* were considered in this study.

1.3.3 Model Coupled Radiation Transfer and Growth Kinetics in Photobioreactors

The third objective of this study was to develop accurate numerical simulation tools to obtain design guidelines for the optimization and operation of efficient photobioreactors. To do so, light transfer in outdoor PBRs with various geometries exposed to solar radiation was analyzed on a spectral basis over the spectral region between 400 and 700 nm corresponding to the photosynthetically active radiation (PAR) region. The temporal evolution of microalgae concentration was also predicted using growth kinetics model taking into account the local available light in the photobioreactors at different times of the day. Finally, the daily productivities of (i) open pons, (ii) flat-plate, and (iii) tubular PBRs was computed and compared to identify design rules and operating guidelines.

1.4 Organization of the Document

Figure 1.6 shows a schematic diagram of the different aspect of this study focusing on simulating outdoor photobioreactors and the corresponding chapters. Chapter 2 introduces the RTE solver based on DG method and GPUs computing along with various validation cases. Chapter 3 presents the retrieval method of the complex index of refraction of the green algae *Chlamydomonas reinhardtii.* Chapter 4 presents predictions of the radiation characteristics of filamentous microorganisms by modeling them either as series of connected spheres or as infinitely long cylinders. Chapter 5 describes 3D numerical simulations of commonly used outdoor PBRs under sunlight. The daily productivities and optimum operation conditions were estimated and compared for different geometries of PBRs. Finally, Chapter 6 summarizes the main conclusions of the present study and discusses recommendations and future work.

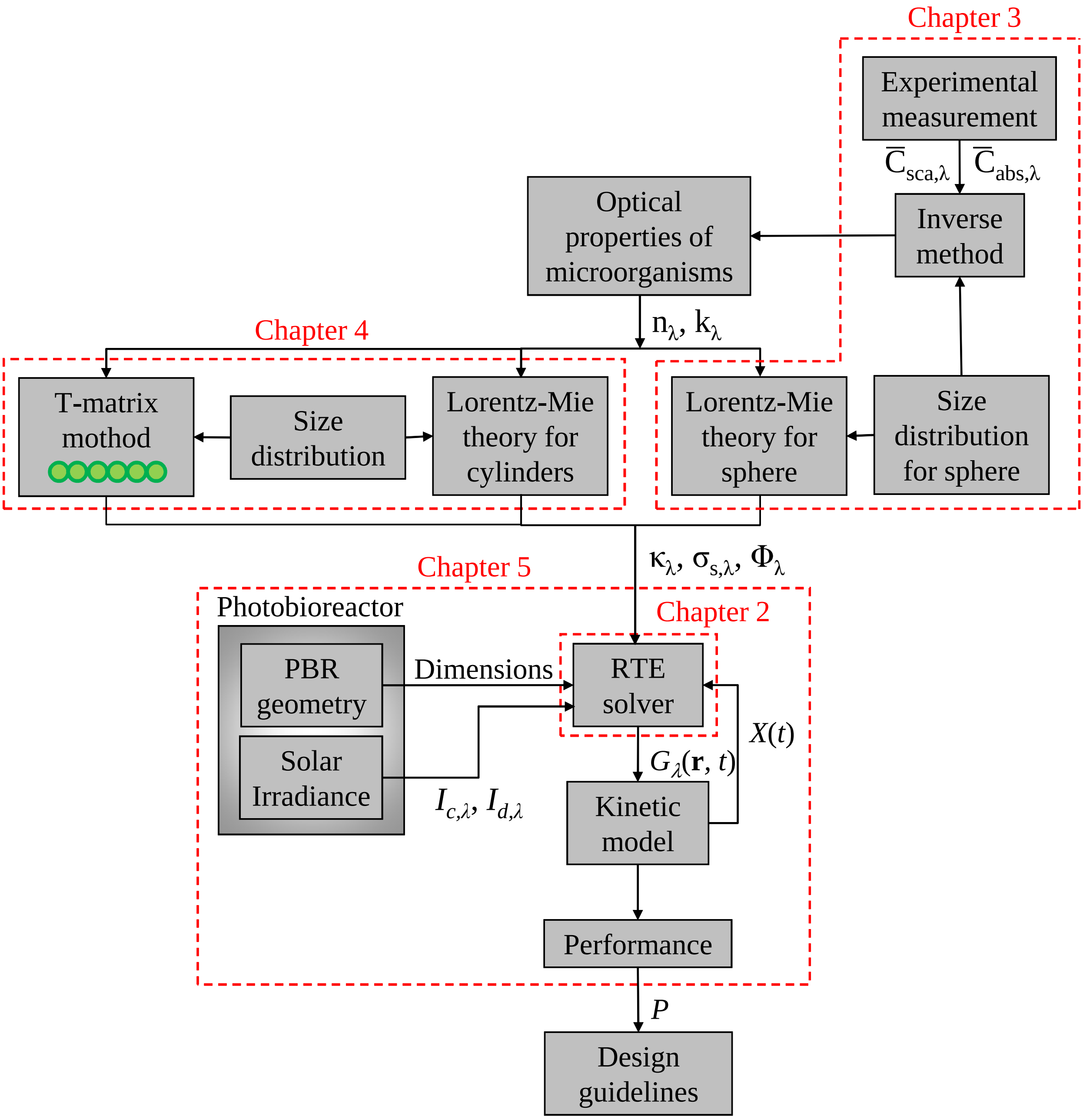

Figure 1.6: Schematic diagram of the integrated RTE solver developed for simulating outdoor photobioreactors. It indicates each chapter of this thesis describing a specific aspect of this integrated simulation tool.

CHAPTER 2

GPU-Based Radiative Transfer Equation Solver

This chapter presents the DG method and GPU computing used to solve the RTE. The code was validated extensively and will be used in Chapter 5 to simulate outdoor PBRs exposed to sunlight.

2.1 Introduction

Thermal radiation is a dominant mode of heat transfer in combustion systems such as rocket engines, scramjets, and industrial furnaces [42, 52, 53]. It must be properly accounted for in preliminary and detailed design phases of systems development to result in a robust and fail-safe design. Hydrocarbon combustion results in exhaust gases, which are dominantly composed of water vapor and carbon dioxide, both of which significantly participate in absorbing and emitting thermal radiation [54]. For designing the rocket nozzle heat shield, quantities such as radiation heat load on the sidewalls, and, more importantly on the nozzle lip which directly faces the exhaust plume, are critical quantities which must be properly estimated [55]. Besides heating, accurate modeling of the thermal radiation emitted by the exhaust plume of a rocket or missile is of utmost importance for military applications for the design of low-observable vehicles and remote-sensing [56].

Empirical correlations used in conjunction with experimental data have been used in the past for the design of such systems [54]. However, increasing complexity and cost has prompted the development of modeling and numerical simulation tools to better understand and design modern combustion systems. Numerical simulation of combustion systems is computationally complex since it involves multi-physics interactions, such as two-phase flow, turbulent mixing, fuel atomization and vaporization, radiative and convective heat transfer, and chemical reaction kinetics [52]. Furthermore, coupling radiative effects in such systems entails the computational burden of addressing multi-scale physical phenomena. Flow, turbulence, combustion, scattering from particles, property gradients (with associated variations in optical thickness) and the propagation of radiation over long distances, represent some multi-scale aspects of the problem. Since the temperature field impacts combustion chemistry, resolution of temporal scales (on the order of μs or less) also adds to the computational complexity. Despite various advancements in numerical methods and computational hardware in recent times, the development of effective physical models and innovative numerical methods remains an important concern. This is particularly important when repeated coupled solutions of flow and radiation are desired in a time evolving calculation, for e.g., in turbulent combustion and plasma dynamics.

2.2 Background

2.2.1 Radiative Transfer Equation

The radiative transfer equation (RTE) was presented in Section 1.2.2. It governs the spectral intensity I_λ and I_ν where ν is the wavenumber given by $\nu = 1/\lambda$. Spectrally and angularly integrated radiative quantities of interest in thermal science and in multiphysics problems, include the total fluence rate $G(\mathbf{r})$, the total radiative heat flux $\mathbf{q}(\mathbf{r})$, and its divergence $\nabla \cdot \mathbf{q}(\mathbf{r})$ respectively defined as [53]

$$\begin{aligned} G(\mathbf{r}) &= \int\limits_{4\pi}\int\limits_{0}^{\infty} I_\nu(\mathbf{r},\hat{\mathbf{s}})d\nu d\Omega, \quad \mathbf{q}(\mathbf{r}) = \int\limits_{4\pi}\int\limits_{0}^{\infty} \hat{\mathbf{s}} I_\nu(\mathbf{r},\hat{\mathbf{s}})d\nu d\Omega, \\ \text{and} \quad \nabla\cdot\mathbf{q}(\mathbf{r}) &= \int\limits_{4\pi}\int\limits_{0}^{\infty} \kappa_\nu(\mathbf{r})\left[I_{b\nu}(\mathbf{r}) - I_\nu(\mathbf{r},\hat{\mathbf{s}})\right] d\nu d\Omega \end{aligned} \tag{2.1}$$

2.2.2 Gas Radiation Model

The absorption coefficients of molecular gases vary significantly as function of temperature, pressure, and wavenumber [42]. This makes radiative transfer calculations in participating gases extremely difficult to carry out. Therefore, gas radiation models have been developed to determine the absorption coefficient κ_ν as a function of gas mixture composition, temperature, and pressure. Water vapor and carbon dioxide are of special importance in combustion of hydrocarbon fuels [42] and also dominate atmospheric radiation [57].

2.2.2.1 Spectral Line-Based Weighted-Sum-of-Gray-Gases (SLW)

Denison and Webb [58–61] developed the spectral line-based weighted-sum-of-gray-gases (SLW) model. This model transforms spectral integration in Equation (2.1) into a summation of a group of fictitious gray gases with specified absorption cross-section C_{abs} and weights a. For a medium with a participating gas of a specified uniform temperature T_g, molar fraction Y_i, and total pressure of gas mixture P_T, the mixture's absorption coefficient or the absorption cross-section can be determined as a function of wavenumber. The blackbody distribution function represents the fraction of blackbody emissive power at a particular temperature T_b for wavenumber such that the cross-section $C'_{abs}(T_g, Y_i, P_T)$ is less than a specific value $C_{abs}(T_g, Y_i, P_T)$. Mathematically, it can be represented as [60]

$$F(T_g, T_b, C_{abs}, Y_i, P_T) = \frac{1}{\sigma T_b^4}\int_{\nu, C'_{abs}<C_{abs}} E_{b\nu}(\nu, T_b)d\nu \tag{2.2}$$

where σ (=5.67 × 10^{-8} W/m^2·K^4) is the Stefan-Boltzmann constant. The weight of blackbody emissive power pertaining to the j^{th} fictitious gray gas component is defined as [60]

$$a_j = F(T_g, T_b, C_{abs,j+1}, Y_i, P_T) - F(T_g, T_b, C_{abs,j}, Y_i, P_T) \quad j = 1, \cdots, N_{C_{abs}} \quad (2.3)$$

where $N_{C_{abs}}$ is the total number of the fictitious gray gas components. Assuming the medium is non-scattering, the RTE along the k^{th} direction $\hat{s}_k$ becomes

$$\hat{s}_k \cdot \nabla I_{j,k} = \kappa_j (I^*_{b,j} - I_{j,k}) \quad \text{with} \quad j = 1, \cdots, N_{C_{abs}} \quad \mathit{and} \quad k = 1, \cdots, N_d \quad (2.4)$$

where $I^*_{b,j} = a_j I_{b,j}$, N_d is total number of the angular directions, and κ_j is the absorption coefficient of the j^{th} fictitious gray gas. Denison and Webb have constructed blackbody distribution functions from HITRAN database [62] for water vapor [59] and carbon dioxide [60]. They also formulated the mathematical correlations between absorption line and distribution function for convenient computer code implementation. Treatments of nonisothermal and nonhomogeneous media were discussed in Ref. [61] by scaling approximation, with the help of reference temperature and the reference gas component fractions. Extension to multicomponent gas mixtures was realized by the multiplication approach described in Refs. [60, 63].

2.2.2.2 Hybrid SNBCK model

The hybrid statistical narrow-band correlated-k (SNBCK) model was proposed by Lacis and Oinas [64]. It was described in detail by Goutière *et al.* [9]. For narrow band gas model, the spectral domain is first divided into a series of narrow bands (in the order of 10 ∼ 100 cm^{-1}). The band width of the i^{th} narrow band is $\Delta\nu_i$, and the RTE for an absorbing, emitting, and non-scattering medium can be written as

$$\mathbf{\hat{s}} \cdot \nabla I_i = \kappa_i (I_{b,i} - I_i) \quad (2.5)$$

where $I_i = I_i(\hat{\mathbf{s}}, \mathbf{r})$ and κ_i are the radiative intensity and absorption coefficient of the i^{th} narrow band, respectively. Note that κ_i may still vary widely in this small spectral window, whereas the blackbody intensity $I_{b,i}$ is a smooth function in term of spectral variable, which can be safely assumed to be constant inside $\Delta\nu_i$ around ν_i. Integration of Equation (2.5) over the spectral region $\Delta\nu_i$ yields,

$$\int_{\Delta\nu_i} \hat{\mathbf{s}} \cdot \nabla I_i d\nu = \int_{\Delta\nu_i} \kappa_i (I_{b,i} - I_i) d\nu \tag{2.6}$$

A cumulative distribution function of absorption, $g_i(k)$, is introduced to represent the fraction in the spectral domain with absorption coefficient less than a specific value and defined as

$$g_i(k) = \int_0^k f_i(k')dk' \tag{2.7}$$

where $f_i(k')$ is the k-distribution function for the absorption coefficient in the spectral interval $\Delta\nu_i$. The function $g_i(k)$ is smooth and varies within $[0, 1]$. Then, Equation (2.6) can be written as

$$\Delta\nu_i \int_0^1 \hat{\mathbf{s}} \cdot \nabla I_i dg_i = \Delta\nu_i \int_0^1 \kappa_i (I_{b,i} - I_i) dg_i \tag{2.8}$$

Since the cumulative function is a smooth function, the integration can be transformed into a quadrature summation, e.g., Gauss quadrature, with N_q quadrature angles. Then, Equation (2.8) becomes

$$\Delta\nu_i \sum_{j=1}^{N_q} (w_j \hat{\mathbf{s}} \cdot \nabla I_{i,j}) = \Delta\nu_i \sum_{j=1}^{N_q} w_j \kappa_{i,j} \left(I_{b,i} - I_{i,j}\right) \tag{2.9}$$

Assuming that the quadrature directions are decoupled, then for each direction one can write [9]

$$\hat{\mathbf{s}} \cdot \nabla I_{i,j} = \kappa_{i,j}(I_{b,i} - I_{i,j}) \quad j = 1, 2, \cdots, N_q \tag{2.10}$$

where $\kappa_{i,j}$ is the absorption coefficient at j^{th} quadrature in i^{th} narrow band and w_j is the weight of the j^{th} Gauss quadrature. For example, the SNBCK model has 44 narrow band (i=1, $\cdots$, 44) in each band 7 Gauss quadrature points (j=1, $\cdots$, 7). Databases of $\kappa_{i,j}$ for water vapor and carbon dioxide in the temperature range 300-2500 K and pressure 1 atm were tabulated by Soufiani and Taine [65].

2.2.3 Discontinuous Galerkin Method For Solving the RTE

The discontinuous Galerkin (DG) method was first used by Reed and Hill [66] to solve the neutron transport equation. It has been applied in recent years, to a large number of problems in computational physics - see, e.g., Hesthaven and Warburton [67] for an exposition of the method. In the DG method the solution is expressed in terms of basis functions which are local to each element and can be discontinuous at element boundaries - as opposed to the traditional finite element method where inter-element continuity of the basis is required. Lagrange polynomials are commonly used as the basis and test functions in the DG method [67]. A DG method of order n is referred to as P_n. In this study, the n-th order Lagrange polynomials were used as basis. High-order accuracy can be achieved by increasing n.

The DG method provides enormous numerical flexibility and is distinguished by the following features: (1) it is elementwise conservative [68], (2) it can provide arbitrarily high-order accuracy and polynomials [68], (3) adaptive variants of the scheme can be developed, where n and mesh resolution may be refined locally [69, 70], (4) the method can be applied to general mesh topologies [71], and (5) it is well suited for parallel computing using graphics processing units (GPUs). This last property results from the observation that high-order DG uses dense local operators, an aspect further explained in Ref. [72].

Cui and Li [68] employed the P-1 DG method for solving the RTE in emitting, absorbing, and anisotropically scattering gray medium. The authors solved the 2D and 3D RTE in square, quadrilateral, and cubic geometries with unstructured triangle and tetrahedral elements. The walls were cold and black. They compared the wall heat flux obtained using the DG method with that obtained by ray-tracing and Monte Carlo methods and found excellent agreement. Moreover, Cui and Li [73] used the P-1 DG method for solving the 2D RTE in emitting, absorbing, and anisotropically scattering gray medium with axisymmetric geometries. The authors found good agreement between the heat flux obtained using the DG method and that predicted by the discrete ordinates method and finite volume method.

Zhao and Liu [71] developed the discontinuous spectral-element method combining the different orders (P-1 to P-14) of DG method with spectral-element method [74] to solve the 2D RTE. In the spectral-element method, orthogonal polynomials such as Chebyshev and Legendre polynomials were used as the interpolation functions of a numerical solution to achieve high-order accuracy [71]. The authors calculated the radiative heat flux for emitting, absorbing, and anisotropically scattering gray medium within 2D square enclosure with blackwalls. They found that the maximum relative error in the radiative heat flux between the discontinuous spectral-element method and discrete ordinates method was less than 0.8%.

Recently, Balima *et al.* [75] solved the 2D RTE in non-emitting, absorbing, isotropically scattering and gray medium using two finite element formulations with the discrete ordinates method. The authors compared the wall heat flux obtained by the least square finite element method and the P-1 DG method. They considered collimated incident radiation and evaluated the accuracy of two different angular quadrature sets namely S_N and T_N. They concluded that the DG method with T_N angular quadrature gave more accurate solutions than least square finite element method with S_N angular quadrature. Balima *et al.* [76] also employed the P-1 DG method for solving the 2D RTE in frequency domain for optical tomography. The medium was gray, non-emitting, absorbing, and anisotropically scattering. The authors also considered collimated incident radiation and used the gradient-based algorithm to retrieve the optical properties of the medium. They concluded that DG method achieved good reconstruction of the optical properties distribution and was well suited for optical tomography.

2.2.4 Graphics Processing Units

The Graphics Processing Unit (GPU) is a highly parallel, multithreaded, and many-core processor (100s of cores) with enormous computing power. Its low cost and high floating-point operation throughput and memory access bandwidth have been attracting more and more researchers in the field of high performance computing [72, 77–80]. In addition, compared with cluster systems that consist of many CPUs, GPU computing is low cost and requires low energy at equivalent performance. Across many disciplines of science and engineering, users have been able to increase performance by several orders of magnitude using GPUs [81].

In the Computational Fluid Dynamics (CFD) community, structured grid Euler solvers for compressible flows on GPU was implemented by Elsen *et al.* [78]. Typically one order of magnitude speedup was achieved by using a single GPU card compared with a single-node CPU implementation. Philips *et al.* [80] implemented a parallel 2D structured grid Euler solver and used a GPU cluster consisting of 8 GPU cards, each having 128 cores. They achieved a speedup of 160 compared with a single CPU implementation. It is worth mentioning that a recent study by Klöckner *et al.* [72] achieved a 40 times speedup when solving Maxwell's equation solver with GPU using the discontinuous Galerkin method and general unstructured 3D grids.

In previous studies solving the RTE using the DG method, the medium was treated as gray and the walls as black. In this chapter, the scope of the prospective applications of the DG-based RTE solver was significantly expanded by considering higher-order method and by including the effects of non-gray media and generalized boundary conditions, as well as by porting the method to GPU computing. In fact, high-order discontinuous Galerkin (DG) method were used to solve the 3D RTE on a spectral basis using the gas radiation models SLW and hybrid SNBCK. Diffuse and collimated incident radiation was considered. Black and diffusely or specularly reflecting walls were also used as boundary conditions to analyze various radiative transfer problems.

2.3 Analysis

2.3.1 Mathematical Details

Efficiently solving the radiative transfer equation in a single direction, even without scattering term, is of critical importance for the overall performance of the RTE solver. For a given direction, the RTE in absorbing, emitting, but non-scattering media takes the following form

$$\hat{\mathbf{s}} \cdot \nabla I_\nu = -\kappa_\nu I_\nu + \kappa_\nu I_{b\nu} \tag{2.11}$$

Under the DG framework [67], multiplying Equation (2.11) with a test function l_m^n and performing volume integration for the n^{th} grid element of volume V^n and surface area A^n yield

$$\int_{V^n} l_m^n \hat{\mathbf{s}} \cdot \nabla I^n dV + \int_{V^n} l_m^n \kappa I^n dV = \int_{V^n} l_m^n \kappa I_b dV \tag{2.12}$$

where the superscript $n \in \{1, \cdots, N\}$ is used to indicate that the integration operation is carried out locally on the n^{th} grid element, out of a total of N grid elements, and l_m^n is the m^{th} test function for the n^{th} grid element $m \in \{1, \cdots, N_p\}$ where N_p is the number of interpolation nodes. For the sake of simplicity, the spectral subscript ν was dropped but it is understood that the radiative intensity and the radiation characteristics presented in all formulations of this sections are wavelength dependent. The *weak* formulation is obtained by applying the Gauss (or divergence) theorem on the first term on the left-hand side (LHS) of Equation (2.12) and is given by

$$\int_{A^n} l_m^n \hat{\mathbf{s}} I^* \cdot d\boldsymbol{A} - \int_{V^n} \nabla l_m^n \cdot \hat{\mathbf{s}} I^n dV + \int_{V^n} l_m^n \kappa I^n dV = \int_{V^n} l_m^n \kappa I_b dV \tag{2.13}$$

where I^* is the numerical radiative intensity to be specified along the boundary of element. Applying the Gauss theorem again on the second term on the LHS of Equation (2.13) yields the *strong* formulation expressed as

$$\int_{V^n} l_m^n \hat{\mathbf{s}} \cdot \nabla I^n dV + \int_{V^n} l_m^n \kappa I^n dV + \int_{A^n} l_m^n (\hat{\mathbf{s}} I^* - \hat{\mathbf{s}} I^-) \cdot d\boldsymbol{A} = \int_{V^n} l_m^n \kappa I_b dV \quad (2.14)$$

The derivation of the weak and strong formulations as well as the introduction of numerical flux through the element boundary is a standard procedure in the DG framework, as detailed in Ref. [67]. The numerical radiative heat flux through the grid element boundary $\hat{\mathbf{s}} I^*$ is a function of radiative intensity along both side of the boundary. The up-wind scheme was employed for numerical flux construction so that

$$\hat{\mathbf{s}} I^* = \begin{cases} \hat{\mathbf{s}} I^+ & \text{if} \quad \hat{\mathbf{s}} \cdot \boldsymbol{A} < 0 \\ \hat{\mathbf{s}} I^- & \text{if} \quad \hat{\mathbf{s}} \cdot \boldsymbol{A} > 0 \end{cases} \quad (2.15)$$

where $\boldsymbol{A}$ is the outward normal vector to the the grid element surface area. The minus superscript ($^-$) refers to variables obtained from the grid element under consideration while the positive superscript ($^+$) is used for variables from adjacent grid elements. Therefore, the third term on the LHS of Equation (2.14) can be written as

$$\int_{A^n} l_m^n (\hat{\mathbf{s}} I^* - \hat{\mathbf{s}} I^-) \cdot d\boldsymbol{A} = \frac{1}{2} \int_{A^n} l_m^n [1 - sign(\hat{\mathbf{s}} \cdot d\boldsymbol{A})] (I^+ - I^-) \hat{\mathbf{s}} \cdot d\boldsymbol{A} \quad (2.16)$$

where the sign function $sign(x)$ is the sign of scalar x. Substituting Equation (2.16) into Equation (2.14) yields

$$\int_{V^n} l_m^n \hat{\mathbf{s}} \cdot \nabla I^n dV + \int_{V^n} l_m^n \kappa I^n dV + \frac{1}{2} \int_{A^n} l_m^n [1 - sign(\hat{\mathbf{s}} \cdot d\boldsymbol{A})] (I^+ - I^-) \hat{\mathbf{s}} \cdot d\boldsymbol{A} = \int_{V^n} l_m^n \kappa I_b dV \quad (2.17)$$

As previously noted, $m \in \{1, \cdots, N_p\}$ and there are N_p relations for the n^{th} grid element. Introducing the vector $L^n = [l_1^n, l_2^n, \cdots, l_{N_p}^n]^T$ and combining Equations

(2.14) to (2.17) yield

$$\int_{V^n} L^n \hat{\mathbf{s}} \cdot \nabla I^n dV + \int_{V^n} L^n \kappa I^n dV + \frac{1}{2} \int_{A^n} L^n [1 - sign(\hat{\mathbf{s}} \cdot d\boldsymbol{A})](I^+ - I^-) \hat{\mathbf{s}} \cdot d\boldsymbol{A} = \int_{V^n} L^n \kappa I_b dV \quad (2.18)$$

Here, the mass matrix can be defined as the matrix of weights used to integrate polynomials whose elements M^n_{mp} for the n^{th} grid element are expressed as functions of Lagrange polynomials

$$M^n_{mp} = \int_{V^n} l^n_m l^n_p dV \quad (2.19)$$

The inverse of this mass matrix can be applied to Equation (2.18) to yield

$$(M^n)^{-1} \int_{V^n} L^n \hat{\mathbf{s}} \cdot \nabla I^n dV + (M^n)^{-1} \int_{V^n} L^n \kappa I^n dV + \frac{1}{2} (M^n)^{-1} \int_{A^n} L^n [1 - sign(\hat{\mathbf{s}} \cdot d\boldsymbol{A})](I^+ - I^-) \hat{\mathbf{s}} \cdot d\boldsymbol{A} = (M^n)^{-1} \int_{V^n} L^n \kappa I_b dV \quad (2.20)$$

The task of the RTE solver is to find $I^n = \sum_{m=1}^{N_p} l^n_m I^n_m$ satisfying Equation (2.20), upon which $N \times N_p$ algebraic equations can be constructed. With these algebraic equations, in theory the solution of the RTE of a particular direction can be found by inverting a $(N \times N_p) \times (N \times N_p)$ matrix. In the RTE solver, the matrix inversion was achieved using an iterative method [82].

The third term in Equation (2.20) is separated into internal and external boundary surfaces since it might involve contribution from domain boundaries which need to be treated as a source term, i.e.,

$$\int_{A^n} = \int_{A^n_{int}} + \int_{A^n_{ext}} \quad (2.21)$$

The external boundary surface integration is separated into

$$\begin{aligned}\frac{1}{2}(M^n)^{-1}\int_{A^n_{bndy}} L^n[1 - sign(\hat{\mathbf{s}}\cdot d\boldsymbol{A})](I^+ - I^-)\hat{\mathbf{s}}\cdot d\boldsymbol{A} = \\ \frac{1}{2}(M^n)^{-1}\int_{A^n_{bndy}} L^n[1 - sign(\hat{\mathbf{s}}\cdot d\boldsymbol{A})](0 - I^-)\hat{\mathbf{s}}\cdot d\boldsymbol{A} + \\ \frac{1}{2}(M^n)^{-1}\int_{A^n_{bndy}} L^n[1 - sign(\hat{\mathbf{s}}\cdot d\boldsymbol{A})](I^+ - 0)\hat{\mathbf{s}}\cdot d\boldsymbol{A}\end{aligned} \tag{2.22}$$

Then, the second part to the RHS of Equation (2.20) is shifted and treated as a source term. If scattering and/or reflecting emissive walls are present, radiative intensities of different direction affect each other and therefore coupling of each direction is required. In the RTE solver, their contribution was treated as a source term using the most recently available intensity solutions and numerical convergence was examined.

2.3.2 Matrix-Free Formulation

The matrix construction was found to consume significant amount of computational resource and time. It was also difficult to efficiently implement it with GPGPUs. The solution adopted in this study consists of writing the algebraic relations of Equation (2.20) for each wavenumber into the classic form

$$\mathbf{Mx} = \mathbf{b} \tag{2.23}$$

where $\mathbf{M}$ is a $(N\times N_p)\times(N\times N_p)$ matrix, $\mathbf{x} = \left[(I^n_m)_{1\leqslant n\leqslant N, 1\leqslant m\leqslant N_p}\right]^T$ is the radiative intensity vector to be solved, and $\mathbf{b}$ corresponds to contribution from blackbody emission, i.e., the RHS term of Equation (2.20) and in-scattering if applicable. Both $\mathbf{x}$ and $\mathbf{b}$ are vectors of size $N\times N_p$. Krylov subspace iteration methods do not require to explicitly build the matrix $\mathbf{M}$ [83]. The ultimate goal of constructing a matrix is for the matrix-vector product computation in Krylov subspace iteration algorithms. By correlating Equation (2.20) and Equation (2.23), the matrix-vector product operation is identical to Equation (2.20)'s LHS. This matrix-vector product can be evaluated using traditional function in the computation framework of the DG method. With an additional vector-vector product function, a matrix free RTE solver can be implemented using the bi-conjugate gradient stabilized (Bi-CGSTAB) method described in Ref. [82]. Based on computational studies on a variety of radiative problems and grids, Bi-CGSTAB method with preconditioner was always able to satisfactorily produce converged solutions for matrix inversions.

2.3.3 Preconditioner

Preconditioner is of equal importance for the iterative method in matrix inversion. The condition number of matrix involved in the RTE solver increases significantly with DG order and grid refinements. Figure 2.1 shows the non-zero elements of the matrix (represented by a + sign) for a problem of $N = 86$ tetrahedron elements with P-3 DG method ($N_p = 20$). A block diagonal pattern is clearly distinguishable. Then, Equation (2.20) can be rewritten as

$$\begin{aligned}(M^n)^{-1}\int_{V^n} L^n\hat{\mathbf{s}}\cdot\nabla I^n dV - \frac{1}{2}(M^n)^{-1}\int_{A^n} L^n[1-sign(\hat{\mathbf{s}}\cdot d\boldsymbol{A})]I^-\hat{\mathbf{s}}\cdot d\boldsymbol{A}\\ +(M^n)^{-1}\int_{V^n} L^n\kappa I^n dV + \frac{1}{2}(M^n)^{-1}\int_{A^n} L^n[1-sign(\hat{\mathbf{s}}\cdot d\boldsymbol{A})]I^+\hat{\mathbf{s}}\cdot d\boldsymbol{A}\\ = (M^n)^{-1}\int_{V^n} L^n\kappa I_b dV \end{aligned} \tag{2.24}$$

The first three terms on the LHS of Equation (2.24) contribute to the diagonal block, while the fourth term contributes to off-diagonal-block elements and source term [Equation (2.22)] for the internal and external boundary, respectively. Then, block Jacobi preconditioner is the natural choice [84]. It depends on direction and gas absorption coefficient present in the second term of Equation (2.24). Since most radiation transfer problems are convection-dominated, the second term can be neglected. Moreover, a gas radiation model independent of preconditioner can be constructed and called partial block Jacobi preconditioner.

Finally, the computational kernels for GPU were implemented using OpenCL

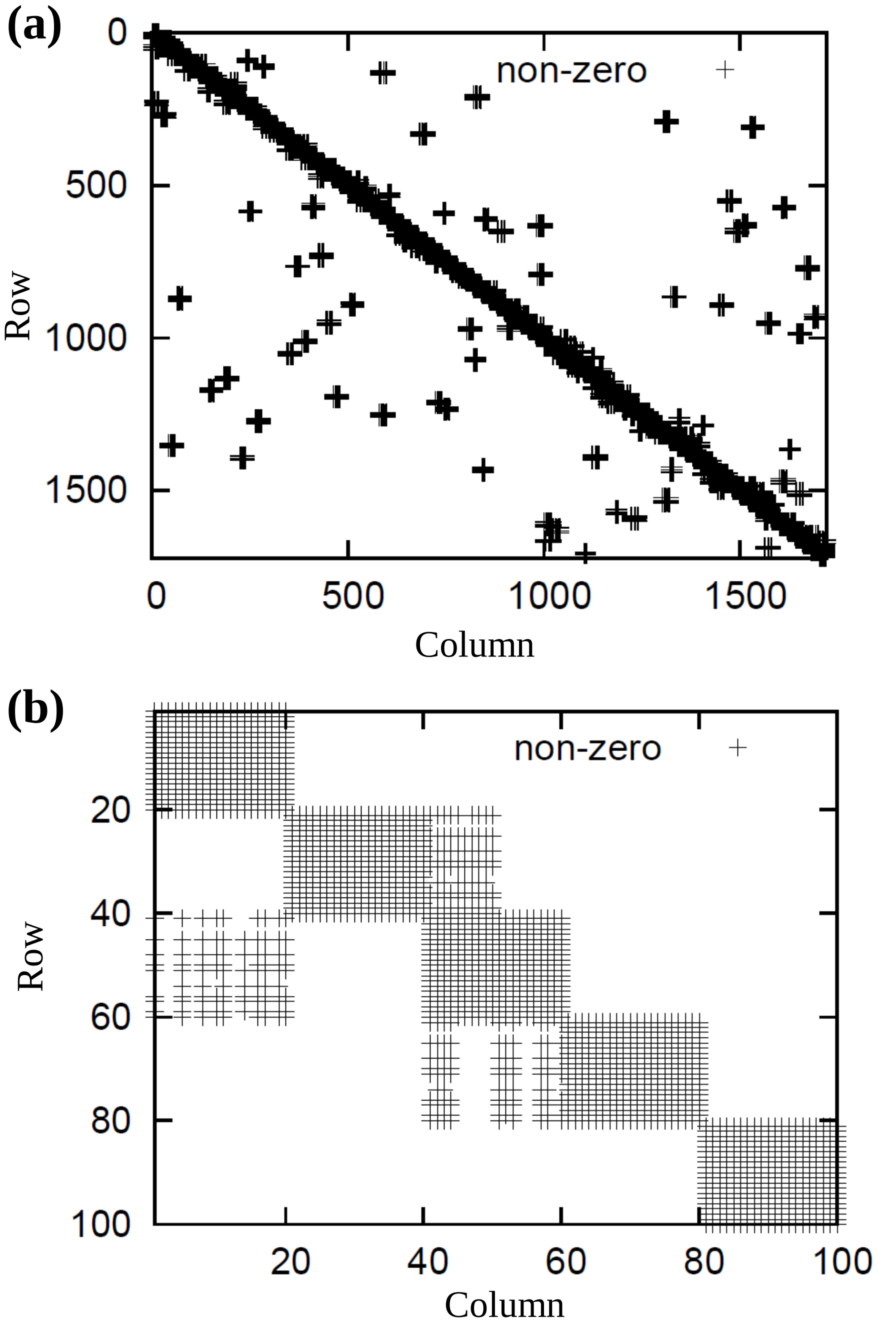

Figure 2.1: Non-zero elements for the $(N \times N_p) \times (N \times N_p)$ matrix of a radiative transfer problem with P-3 DG scheme ($N_p = 20$). The grid mesh consists of N = 86 tetrahedron elements (a) full matrix, and (b) close-up view of the matrix.

[85], which provides portability across multiple computing platforms. To efficiently exploit the GPU's enormous capability of floating point operations, computational tasks should be parallelizable. Most of the computation operators in the DG framework are carried out in an element-local manner. Therefore the RTE solver based on GPU method is well suited for GPU computing [72]. For the GPU kernels of RTE solver, a thread block was typically employed to carry out element-wise calculations, whereas the threads within the same block cooperate efficiently via shared memory. In the GPU computation mode, the entire solution process was performed on the GPU, with the exception of initialization (e.g., problem setup and grid reading and partitioning) and communication of fields on processor boundaries which were performed by the CPU.

2.4 Validations

The RTE solver developed in this study was implemented as a 3D solver employing tetrahedron elements. It can also be employed to investigate 2D or 1D radiative problems which are frequently encountered in the literature [42]. To simulate 2D problems (in the $x - y$ plane), a 3D mesh with one cell in the $z-$direction was generated and the two $x - y$ planes were set to be specularly reflecting. It is evident that specularly reflecting boundary results in direction coupling and increases computational needs/requirements. To diminish the coupling effect, a grid of tall cells with aspect ratio of 50 in the $z-$direction was used. It was realized by scaling up a homogeneous grid in the $z-$direction. Based on the experience, 3 to 5 iterations were sufficient to ensure the convergence of direction coupling using tall cells.

2.4.1 2D Radiative Transfer in Gray, Emitting, Absorbing, and Non-scattering Media with Black Boundaries Exposed to Diffuse Irradiation

Goutière *et al.* [9] solved the 2D RTE in 1.0 m × 0.5 m rectangular enclosure with cold and black side walls containing a gray gas at uniform temperature 1000 K. The absorption coefficient was also uniform and equal to $\kappa = 0.5$ m^{-1}. The domain was discretized in 61 × 31 square cells in the $x-$ and $y-$directions, respectively. The angular discretization T_7 and finite volume spatial discretization were used to solve the 2D RTE.

The same problem was solved by the 3D RTE solver using in the $x - y$ plane. The cell were 20 m long in the $z-$direction to diminish direction coupling introduced by the reflecting walls. Here also, T_7 angular discretization and P-1 DG method were employed. Figure 2.2 compares the radiative heat flux and its divergence as a function of x and y obtained by the solver with those reported in Ref. [9]. The average and maximum relative errors between the numerical results for the wall heat flux along the boundary walls y=0 m and those reported by Goutière *et al.* [9] were 0.6% and 2.2%, respectively. In addition, the average and maximum relative errors for the divergence of radiative heat flux along the center lines were 0.1% and 0.3%, respectively. Overall the results from the DG solver were in good agreement with those reported in Ref. [9].

2.4.2 2D Radiative Transfer in Non-gray, Emitting, Absorbing, and Non-scattering Media with Black Boundaries Exposed to Diffuse Irradiation

This section describes validation of the 3D RTE solver for non-gray gas models contained in a 2D rectangular 1.0 m × 0.5 m enclosure as solved by Goutière *et al.* [9]. The participating gases considered were H_2O and CO_2 in a non-participating

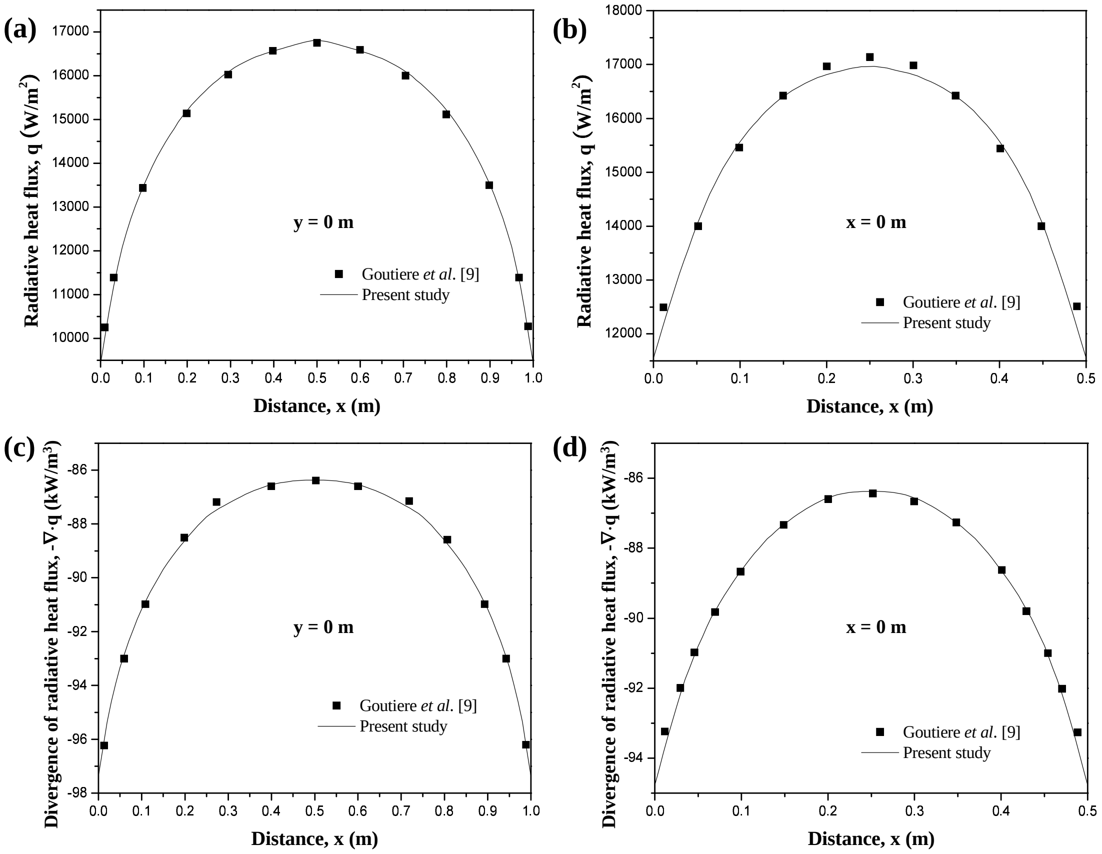

Figure 2.2: Comparison of simulation results with Ref. [9] of a 2D 1.0 m × 0.5 m rectangular enclosure with cold and black side walls containing a gas at uniform temperature of 1000 K and uniform absorption coefficient $\kappa = 0.5\ \mathrm{m}^{-1}$, (a) and (b) heat flux along boundary walls in the x- and y- directions, respectively, and (c) and (d) divergence of radiative heat flux along the center lines in the x- and y- directions, respectively.

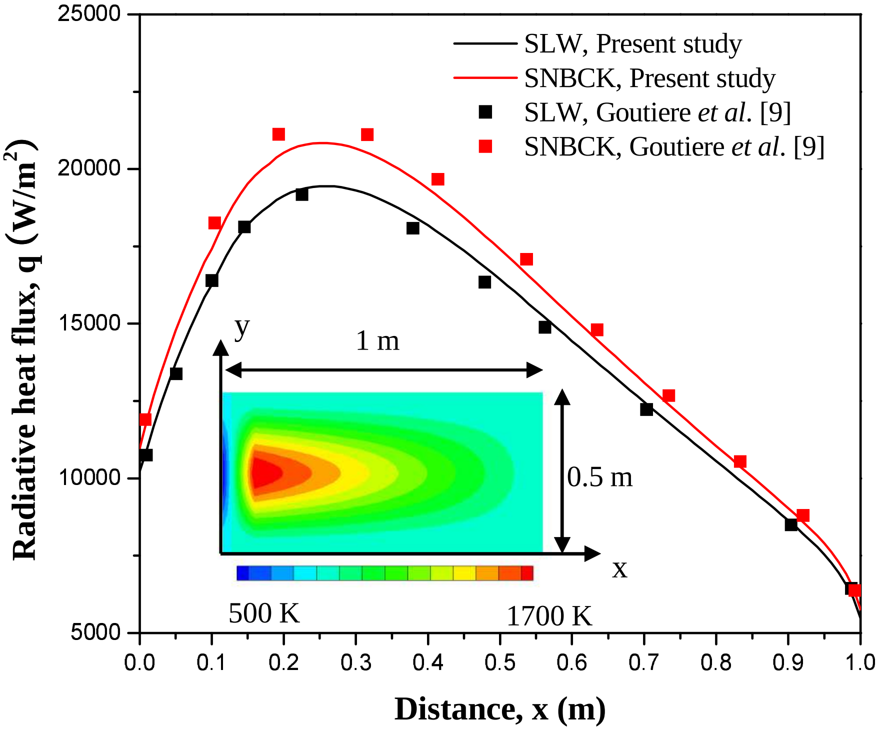

Figure 2.3: Comparison of predicted wall heat flux using SLW and SNBCK gas radiation models in a 2D rectangular enclosure with those reported in Ref. [9]. The enclosure contained H_2O and CO_2 in moral fractions 0.2 and 0.1, respectively. The wall were cold and black walls. The gas temperature was non-uniform and given by Equation (2.25).

gas with uniform mole fractions of 0.2 and 0.1, respectively. The temperature distribution within the enclosure was prescribed as [9]

$$T(x,y)=\begin{cases}(14000x-400)(1-3y_0^2+2y_0^3)+800 & \text{for} \quad 0\le x\le 0.1\ \text{m}\\ -\dfrac{10000}{9}(x-1)(1-3y_0^2+2y_0^3)+800 & \text{for} \quad x>0.1\ \text{m}\end{cases} \qquad (2.25)$$

where $y_0 = 4|0.25-y|$. This temperature profile is a typical representation of furnace combustion. The medium was absorbing, emitting, and non-scattering and all walls were cold and black. Here, the RTE was solved using T_7 angular discretization and finite volume spatial discretization 61×31 square cells in the

$x-$ and $y-$directions. Figure 2.3 compares the predictions for the wall heat flux obtained with the present RTE solver using the gas models SLW and SNBCK with those reported in Ref. [9]. The average and maximum relative errors between the numerical results for the wall heat flux along boundary walls and those reported by Goutière *et al.* [9] were 1.7% and 3.1%, respectively. Overall, the results obtained with the RTE solver using SLW and SNBCK gas radiation models were in good agreement with those reported in Ref. [9].

2.4.3 3D Radiative Transfer in Non-gray, Emitting, Absorbing, and Non-Scattering Media with Black Boundaries Exposed to Diffuse Irradiation

Let us consider a parallelepiped enclosure with the dimension of [-1.0 m, 1.0 m] × [-1.0 m, 1.0 m] × [0.0 m, 4.0 m] in the $x-$, $y-$, and $z-$directions, respectively. All six of the enclosure's sidewalls were black at 300 K. Temperature along the enclosure centerline (x = 0, y= 0, z) was prescribed as

$$T_c(0,0,z) = \begin{cases} T_i + (1800 - T_i)z/0.375 & \text{for} \quad 0 \leq z \leq 0.375\,\text{m} \\ 1800 + (T_e - 1800.0)(z - 0.375)/(4.0 - 0.375) & \text{for} \quad z > 0.375\,\text{m} \end{cases} \tag{2.26}$$

where T_i = 400 K and T_e = 800 K. The gas temperature was symmetric about the centerline with

$$T(r) = (T_c - T_e)f(r/R) + T_e \quad \text{with} \quad f(r/R) = 1 - 3(r/R)^2 + 2(r/R)^3 \tag{2.27}$$

where $r = \sqrt{x^2 + y^2}$ is the distance from the centerline and $R = 1.0$ m. The gas mixture consisted on CO_2 and water vapor in N_2 with uniform mole fractions of 0.1, 0.2, and 0.7, respectively. Simulations were performed using (i) uniform grid resolutions $\Delta x = \Delta y = \Delta z = 0.2$ m corresponding to 10 × 10 × 20 cells (ii) three different DG orders (P-1, P-2, or P-5), and (iii) two different angular quadrature sets (S_8 or T_4). Figure 2.4 shows the computed wall heat flux along the centerline

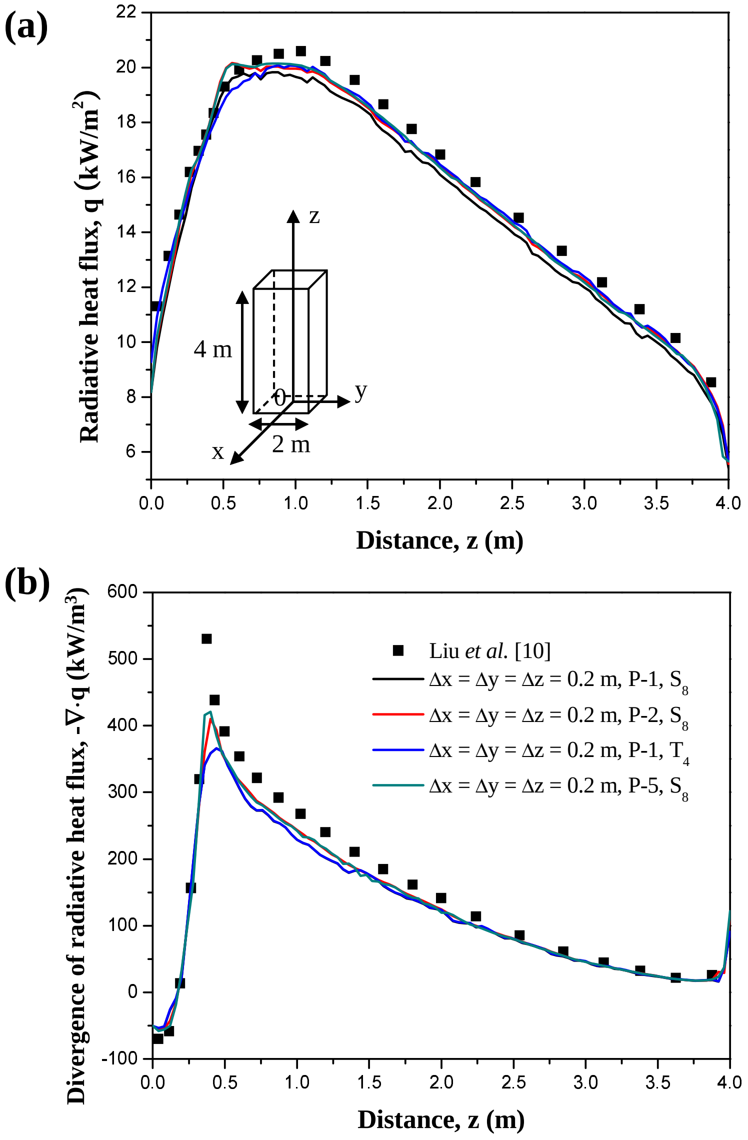

Figure 2.4: Comparison of simulated (a) radiative heat flux along the centerline of a sidewall (x = -1.0, y = 0, z) and (b) divergence of radiative heat flux along the centerline (x = 0, y = 0, z) for a 3D rectangular enclosure containing absorbing, emitting, and non-scattering gas mixture at a specified temperature [Equation (2.26)] with SNBCK gas model and different DG order (P-1, P-2, and P-5), grid size ($\Delta x = \Delta y = \Delta z$), and angular quadratures (S_8 and T_4) with that reported in Ref [10].

of a sidewall (x = -1.0 m, y = 0, z), with different simulation settings and the distribution of divergence of radiative heat flux along the centerline of enclosure (x =0, y = 0, z). The predictions were compared with the results reported in Ref. [10] obtained using T_4 angular discretization and finite volume spatial discretization $17 \times 17 \times 24$ rectangular cells in the $x-$, $y-$, and $z-$directions. The average and maximum relative errors between the numerical results for the radiative heat flux along (-1, 0, z) and those reported by Ref. [10] were 5% and 12%, respectively. In addition, the average and maximum relative errors between the numerical results for the divergence of radiative heat flux along (0, 0, z) and those reported by Ref. [10] were 12% and 19%, respectively. The predictions using different combinations of DG orders, grid resolutions, and angular quadrature types all agree well with those reported in Ref. [10].

This study demonstrates that in order to achieve accurate simulation results using the RTE solver, one can choose to employ coarse grid resolution and higher-order of DG scheme or fine grid resolution and lower order of DG scheme. Based on the testing, the combination of higher-order DG scheme and coarser grid is preferable in terms of accuracy and computational time for problem with smooth solution. However, finer grid resolution is required for area with sharp discontinuity in the solution.

2.4.4 1D Radiative Transfer in Gray, Emitting, Absorbing, and Non-Scattering Media with Reflecting Boundaries Exposed to Diffuse Irradiation

All previous studies using the DG method to solve the RTE considered black walls [68,71,75]. This section discusses the validity of the RTE solver for problems involving non-black diffusive walls and diffusely emitting and reflecting boundaries. The incoming radiative intensity from non-black diffusive walls is determined by the reflected out-going intensity and the blackbody intensity. Here, the

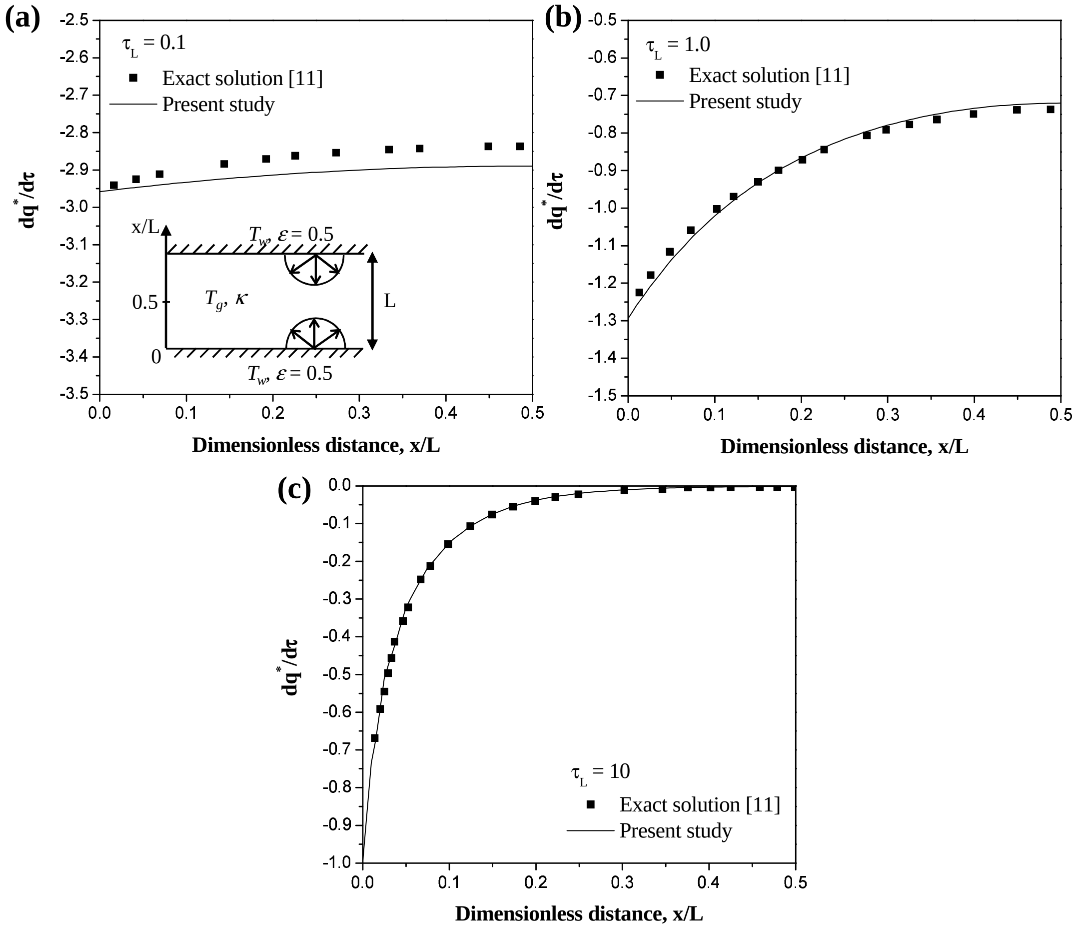

Figure 2.5: Comparison of divergence of dimensionless radiative heat flux [Equation (2.1)] between DG method solution and the exact solution [11] for 1D absorbing and emitting gray gas at $T_g = 1500$ K with gray diffusely reflecting and emitting walls at $T_w = 500$ K with $\epsilon = 0.5$. The medium optical thickness was (a) $\tau_L = 0.1$, (b) $\tau_L = 1.0$, and (c) $\tau_L = 10.0$.

benchmark problems solved analytically in Ref. [11] were used. It consists of a 1D gas layer of thickness L sandwiched between two walls at temperature $T_w = 500$ K with emissivity $\epsilon = 0.5$. The gas was treated as gray, emitting, absorbing, and non-scattering with optical thickness $\tau_L = \kappa L$ equal to 0.1, 1.0, and 10. The gas temperature was uniform and equal to $T_g = 1500$ K. The walls were gray and diffusively emitting and reflecting. Figure 2.5 compares the numerical predictions with the exact solution [11] for the divergence of the dimensionless radiative heat flux as a function of x/L defined as [11]

$$\frac{dq^*}{d\tau} = \frac{dq/d\tau}{\sigma(T_w^4 - T_g^4)} \tag{2.28}$$

The numerical results were obtained using the P-6 DG method and S_8 angular discretization with a grid consisting of 125 tetrahedron elements. They fell within 2% of the exact solution [11] for all optical thicknesses considered. These results demonstrate that the DG method can accurately simulate diffusely emitting and reflecting boundaries.

2.4.5 2D Radiative Transfer in Gray and Purely Scattering Media with Black Boundaries Exposed to Diffuse Irradiation

This section explores the performance of the DG method to deal with different scattering phase functions. Kim and Lee [12] considered a 2D 1 m × 1 m square enclosure filled with a scattering medium and 5 different scattering phase functions, namely (i) isotropic, (ii) two forward with Henyey-Greenstein asymmetric factor g = 0.84534 (F1) and 0.66972 (F2), and (iii) two backward with g = -0.18841 (B1) and -0.4 (B2) (see Fig. 2 in Ref. [12]). Trivic *et al.* [13] simulated similar problems using the finite volume method for angular discretization with 25 × 25 control volumes. Trivic and Amon [86] extended their 2D study [13] to 3D problem, with the same set of scattering phase functions.

In the present study, the medium was purely scattering and all walls were black

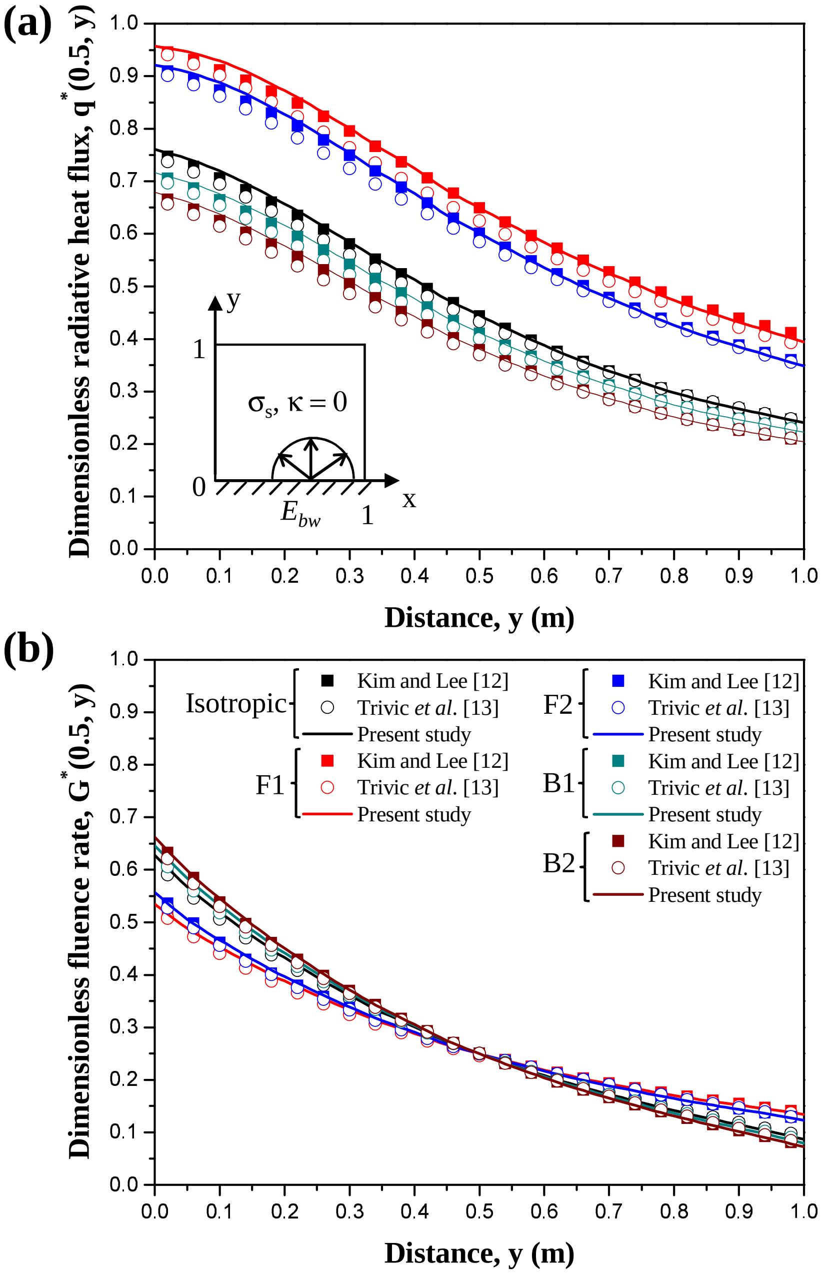

Figure 2.6: (a) Dimensionless heat flux $q^*(0.5, y)$ and (b) fluence rate $G^*(0.5, y)$ along the y-axis for center of x-axis in a 2D enclosure containing purely scattering media with isotropic, strongly forward (F1 and F2), and strongly backward (B1 and B2) scattering phase functions. The results are compared with previously reported studies [12, 13] obtained using finite volume method and DOM. Here, $q^*(x, y) = q(x, y)/E_{bw}$ and $G^*(x, y) = G(x, y)/4E_{bw}$.

and cold except the bottom wall at $(x, y = 0)$ which had blackbody emissive power E_{bw}. In addition, the dimensionless fluence rate G^* was defined as $G^* = G/4E_{bw}$ and the dimensionless radiative heat flux was defined as $q^* = q/E_{bw}$ [12]. The simulations were carried out by using P-1 DG method on a grid consisting of 4810 tetrahedron elements and by using finite volume method for angular discretization with $N_\theta = 4$ and $N_\phi = 60$. Figures 2.6 show the dimensionless heat flux q^* and the fluence rate G^* predicted as a function of distance y along the center line $x =$ 0.5 m. The average and maximum relative errors between the numerical results for the dimensionless heat flux $q^*(0.5, y)$ and those reported by Ref. [12, 13] were 3% and 4%, respectively. In addition, the average and maximum relative errors between the numerical results for dimensionless fluence rate $G^*(0.5, y)$ and those reported by Ref. [12, 13] were 1% and 4%, respectively. Overall, the numerical predictions were in good agreement with the data obtained from Refs. [12, 13] for all scattering phase functions considered.

2.4.6 3D Radiative Transfer in Gray, Emitting, and Absorbing, and Scattering Media with Black and Reflecting Boundaries Exposed to Diffuse Irradiation

This section compares the simulation results for the 3D combustor shown in Figure 2.7 with those provided in Refs. [14, 87]. The geometrical feature of this problem was quite complex and grid generation was challenging as there were five thin baffles located at a corner of the domain. A in-house grid generation tool was used to generate an unstructured body-fitted grid. The medium was gray, emitting, absorbing, and scattering, with the following temperature and absorption

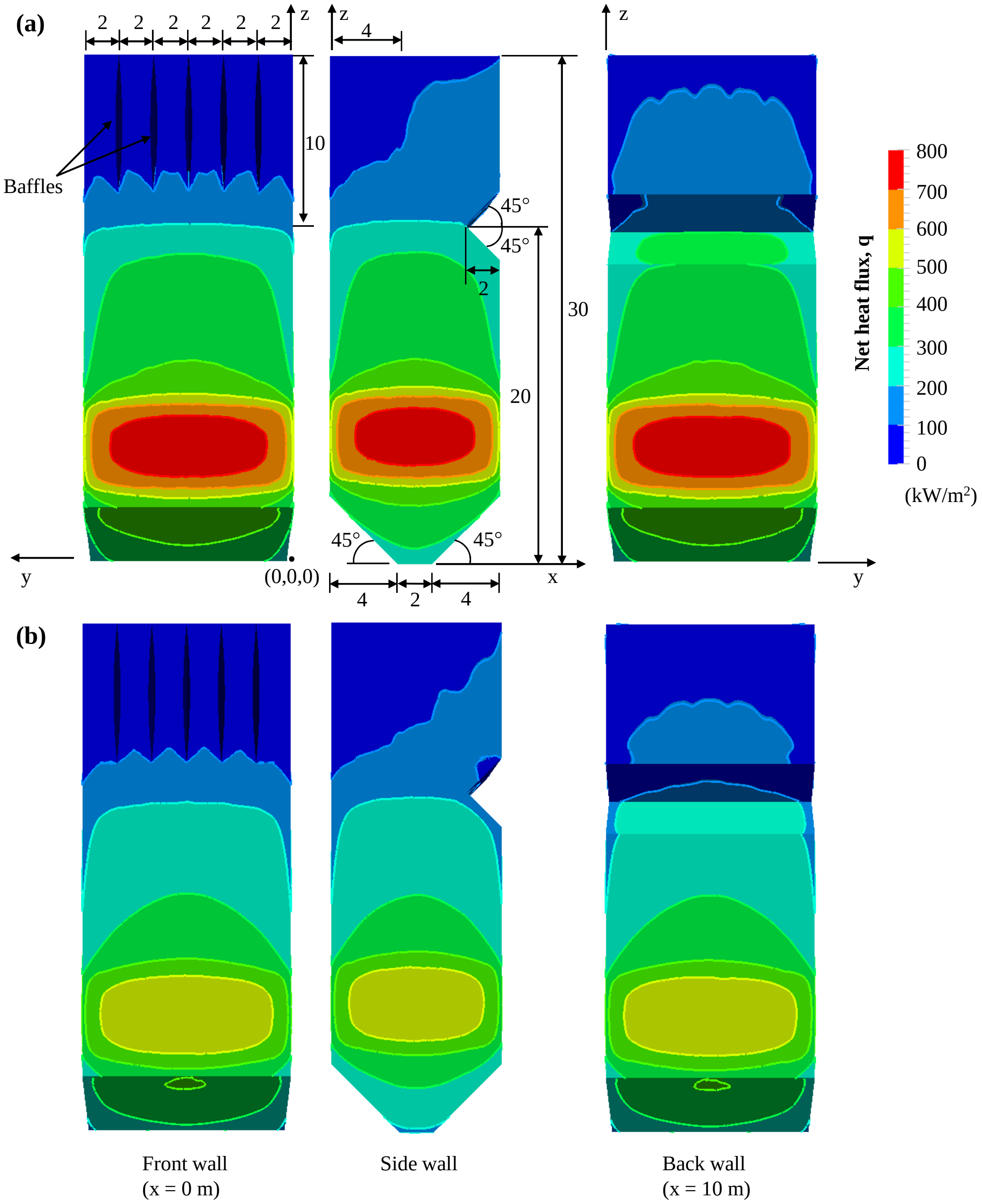

Figure 2.7: Geometry, dimension, and simulation results of the net radiative heat flux on the front, side, and back walls of a 3D combustor chamber [14] with absorbing, emitting, (a) non-scattering medium ($\omega = 0.0$) and (b) scattering medium ($\omega = 0.5$). All dimensions are in meter.

coefficient spatial distributions

$$\begin{cases} \kappa = 0.20\,\mathrm{m}^{-1}, T = 1600\,\mathrm{K} & \text{for} \quad z \leq 5\,\mathrm{m} \\ \kappa = 0.25\,\mathrm{m}^{-1}, T = 2000\,\mathrm{K} & \text{for} \quad 5 \leq z \leq 10\,\mathrm{m} \\ \kappa = 0.20\,\mathrm{m}^{-1}, T = 1600\,\mathrm{K} & \text{for} \quad 10 \leq z \leq 20\,\mathrm{m} \\ \kappa = 0.18\,\mathrm{m}^{-1}, T = 1200\,\mathrm{K} & \text{for} \quad 20 \leq z \leq 30\,\mathrm{m} \end{cases} \tag{2.29}$$

Temperature and emissivity of boundary region located at $x = 10$ m and 22 m $\leq z \leq 30$ m were specified to be 1200 K and 1.0, respectively. The temperature and emissivity at other boundaries, including at the baffle surfaces, were specified to be 800 K and 0.65, respectively. Two cases with different scattering albedos $\omega = 0.0$ and 0.5 were simulated. DOM with S_8 angular discretization scheme and P-3 DG method were employed. The grid consisted of 54266 tetrahedral elements. In Refs. [14, 87], 72000 hexahedral elements were employed with block-off-region procedure to deal with irregular geometrical domain, i.e, non-orthogonal walls were represented with stair-case grid.

Figure 2.7 shows the net radiative heat flux on the front wall, sidewall, and back wall for (a) $\omega = 0.0$ and (b) $\omega = 0.5$ of the 3D combustor. Discrepancies in flux contour can be observed around the concave area compared with the solutions reported in Fig. 10 of Ref. [87] and Fig. 9 of Ref. [14]. The simulations in this study produce better results than that of Refs. [14,87] in these area since boundary conforming mesh was employed instead of block-out technique on Cartesian grid to represent the non-orthogonal boundaries. As pointed out in Ref. [88], the block-off technique introduced significant error in the computed heat flux on non-orthogonal walls.

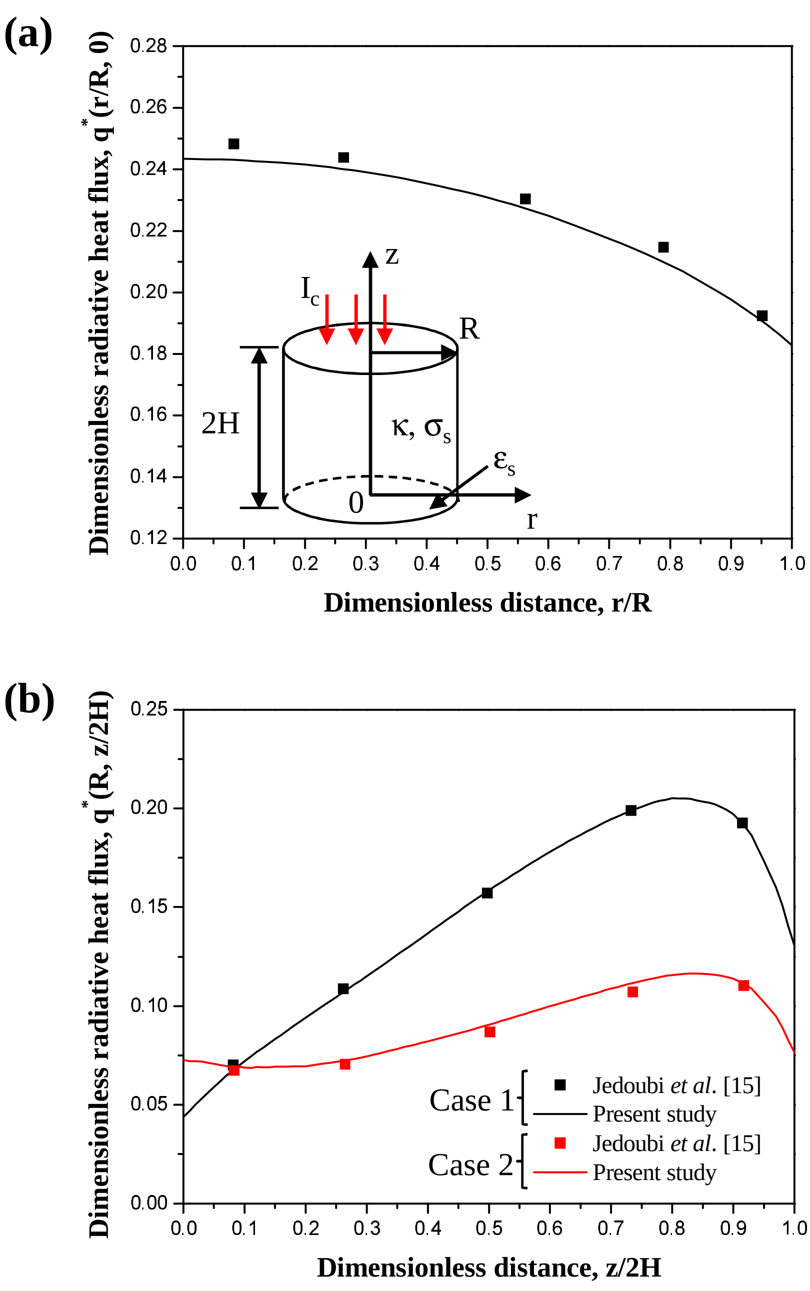

Figure 2.8: Dimensionless radiative heat flux along (a) the bottom wall $q^*(r/R, 0)$ and (b) along the sidewall of the cylindrical enclosure $q^*(R, z/2H)$ with R = H = 1 m containing cold, absorbing, and isotropically scattering medium exposed to collimated radiation incident from the top wall. Case 1 is such that $\epsilon_s = 1.0$, $\kappa = 0.0$ m^{-1}, and $\sigma_s = 1.0$ m^{-1}. Case 2 is such that $\epsilon_s = 0.5$, $\kappa = 0.3$ m^{-1}, and $\sigma_s = 0.7$ m^{-1} [15].

2.4.7 2D Radiative Transfer in Gray and Purely Scattering Media with Black Boundaries Exposed to Collimated Irradiation

This section discusses validation of the RTE solver for applications with collimated incident irradiation. Figure 2.8(a) shows the cylindrical enclosure of radius R and height H such that $R = H = 1.0$ m. Normal collimated radiation ($I_c = 1.0$ W/m^2.sr) was incoming from the top wall. The enclosure was filled with cold, gray, and homogeneous absorbing and isotropically scattering medium with optical radius $\tau_R = (\kappa + \sigma_s)R = 1.0$. The cylindrical sidewall was cold and black ($\epsilon_s = 1.0, T_s = 0$ K). Jendoubi *et al.* [15] studied two cases. Case 1 had bottom wall emissivity $\epsilon_s = 1.0$ while the medium absorption and scattering coefficients were $\kappa = 0.0$ m^{-1} and $\sigma_s = 1.0$ m^{-1}, respectively. Case 2 had bottom wall emissivity $\epsilon_s = 0.5$ and absorption and scattering coefficients $\kappa = 0.3$ m^{-1} and $\sigma_s = 0.7$ m^{-1}, respectively. Angular discretization scheme T_4 and P-3 DG method were employed. The grid consisted of 6872 tetrahedral elements. The dimensionless radiative heat flux was defined as $q^*(r, z) = q(r, z)/E_b$ where E_b is the blackbody emissive power set at $E_b = \pi$. Figure 2.8 compares the numerical predictions for the dimensionless radiative heat flux (a) at the bottom wall $q^*(r/H, z)$ and along the cylinder sidewall $q^*(z/2H, z)$ with those reported by Ref. [15] for Cases 1 and 2. The average and maximum relative errors between them were 3% and 4%, respectively. This demonstration that the DG method can also simulate collimated irradiation problems.

2.5 Speedup of GPU vs. CPU

Let us consider a benchmark problem consisting of a 3D square enclosure 2 m × 2 m × 2 m having cold black walls and containing a gray, absorbing, emitting, and non-scattering medium with the following spatial distributions of the blackbody

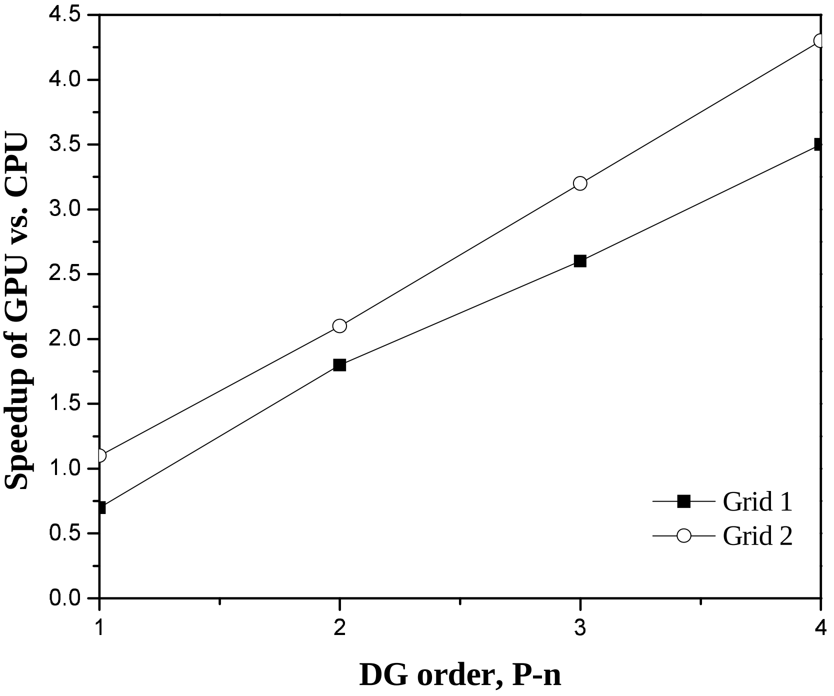

Figure 2.9: Speedup of GPU vs. CPU implementation as a function of DG order for a 3D radiative transfer problem in gray, absorbing, emitting, and non-scattering medium at the prescribed temperature field with $\kappa = 0.1$ m^{-1}. Grid 1 and grid 2 consisted of 2,861 and 22,655 tetrahedron elements, respectively.

radiation intensity

$$\begin{aligned} I_b(x,y,z) &= \frac{\pi}{2\kappa}s_x \cos\left(\frac{\pi}{2}x\right)\left[1+\sin\left(\frac{\pi}{2}y\right)\right]\left[1+\sin\left(\frac{\pi}{2}z\right)\right] \\ &+ \frac{\pi}{2\kappa}s_y \left[1+\sin\left(\frac{\pi}{2}x\right)\right]\cos\left(\frac{\pi}{2}y\right)\left[1+\sin\left(\frac{\pi}{2}z\right)\right] \\ &+ \frac{\pi}{2\kappa}s_z \left[1+\sin\left(\frac{\pi}{2}x\right)\right]\left[1+\sin\left(\frac{\pi}{2}y\right)\right]\cos\left(\frac{\pi}{2}z\right) \\ &+ \left[1+\sin\left(\frac{\pi}{2}x\right)\right]\left[1+\sin\left(\frac{\pi}{2}y\right)\right]\left[1+\sin\left(\frac{\pi}{2}z\right)\right] \end{aligned} \tag{2.30}$$

where the absorption coefficient was $\kappa = 0.1$ m^{-1} and a single angular direction, $\hat{\mathbf{s}} = (s_x, s_y, s_z) = (0.62402, 0.52802, 0.57602)$ was considered. The temperature field can be defined as $T(x,y,z) = [\pi I_b(x,y,z)/\sigma]^{\frac{1}{4}}$ where σ ($= 5.67 \times 10^{-8}$ W/m^2·K^4) is the Stefan-Boltzmann constant. The RTE was solved using the DG method with order ranging from P-1 to P-4 and with two different grids consisting of 2,861 and 22,655 tetrahedron elements. The CPU code was executed on a workstation with Intel® Xeon® CPU E5620 2.40GHz. The GPU code was executed on a NVIDIA® GeForce® GTX 480 card, with OpenCL 1.0 CUDA 3.2.1. The computational time for the solution along one radiative angular direction were used to calculate the speedup associated with using GPU computing. Figure 2.9 shows the speedup of RTE solver in GPU mode vs. CPU mode for a benchmark problem. The speedup was up to 4.0 and increased with increasing DG scheme order. Indeed, higher-order DG requires more floating points and is better suited to GPU computing.

2.6 Conclusions

This study presented high-order discontinuous Galerkin (DG),combined with finite volume (FVM) and discrete ordinates method (DOM) for solving the RTE. DG method was incorporated with non-gray gas radiation models such as spectral line-based weighted-sum-of-gray-gases (SLW) and hybrid SNBCK model. Both diffusively and specularly reflecting walls were modeled along with diffuse and collimated incident irradiation in 3D enclosures. An important aspect of this work is the porting of the DG RTE solver to GPUs demonstrating very attractive computational speedup. Studies have revealed which computations benefit the most from GPU acceleration. The GPU-based high-order accurate solver bears the potential for high computational efficiency in large scale RTE simulations with extensive variations in optical thickness. It will be used in Chapter 5 to compare the design and performance of different outdoor PBRs exposed to sunlight.

CHAPTER 3

Spectral Optical Properties of Spherical Green Microalgae *C. reinhardtii* CC125 and Its Truncated Chlorophyll Antenna Transformants *tla1*, *tlaX*, and *tla1-CW*$^+$

3.1 Introduction

In order to design, optimize, and operate photobioreactors for CO_2 fixation and biofuel production, it would be convenient to have the ability to predict the radiation characteristics of microalgae from first principles instead of carrying out costly and time consuming experiments. If the effective spectral real and imaginary parts of the complex index of refraction as well as the microorganisms shape and size distribution are known to within an acceptable level of uncertainties, the absorption and scattering coefficients can be predicted by Lorentz-Mie theory [89], if the microalgae are spherical, or by the T-matrix method [90], if the particles have more complex shapes.

3.2 Background

3.2.1 Radiation Characteristics of Microalgae

A large body of literature exists on predicting and measuring the absorption and scattering coefficients and the scattering phase function of microalgal suspension

[24,44,91–93].

Bidigare *et al.* [2] used a predictive approach to determine the absorption coefficient in various species of phytoplankton. The cell was modeled as a homogeneous particle in which only the pigments in the cell contributed to the absorption coefficient in the photosynthetically active radiation (PAR) region between 400 and 700 nm. Then, the absorption coefficient (in 1/m) was expressed as [94]

$$\kappa_\lambda = \sum_{i=1}^{N} Ea_i C_i \tag{3.1}$$

where Ea_i (in m^2/kg) is the *in vivo* specific spectral absorption coefficient of pigment i (Figure 1.2) and C_i are their mass concentrations (in kg/m^3).

Pottier *et al.* [39] used a similar approach to predict the spectral absorption coefficient of *C. reinhardtii* by assuming that the pigments were uniformly distributed within the cell and only Chl *a*, Chl *b*, and PPC were present. The authors modified the expression for the absorption coefficient given by Bidigare *et al.* [2] to express it in terms of pigment mass fractions as

$$\kappa_\lambda = \rho_{dm} \frac{1 - x_w}{x_w} \sum_{i=1}^{N} Ea_i w_i \tag{3.2}$$

where ρ_{dm} is the density of dry material in the biomass (in kg/m^3), x_w is the volume fraction of water in the cell, while w_i is the dry mass fraction of pigment i.

Moreover, Quirantes and Bernard [95] modeled algal cells as two-layer particles with an inner core and an external coating. The coating was assumed to be non-absorbing and had a refraction index of 1.36. The inner core was absorbing and featured a larger refraction index than the outer coating. Its value was selected such that the volume-averaged complex index of refraction of the composite particle was equal to that of an equivalent homogeneous scatterer with complex index of refraction of 1.40 + i0.005, considered to be typical of microbial cells [45,96,97]. First, the extinction and absorption efficiency factors of homogeneous spheres and coated spheres were calculated using the Aden-Kerker theory [98] and the modified anomalous diffraction approximation (ADA) [99], respectively. The heterogeneous geometry of the coated spheres was found to increase the back-scattering efficiency by a factor as high as 50 but had negligible effects on the absorption efficiency factor and weak effects on the scattering efficiency factor when compared with those of a homogeneous sphere with the same complex index of refraction. These results were consistent with previous studies using volume-averaged equivalent complex indices of refraction to compare homogeneous and heterogeneous multi-layered spheres [100, 101]. In addition, Quirantes and Bernard [95] considered three different geometries with the same size parameter and equivalent complex refractive index namely (i) off-centered coated spheres, (ii) concentric spheroids, and (iii) concentric spheres. The T-matrix method [102] was used to compute the efficiency factors of the aspherical and non-concentric composite cells. The absorption and scattering efficiency factors showed little dependency on particle shape.

Mishchenko and Travis [23] concluded that particles that were even moderately aspherical could not be approximated as equivalent spheres of diameter d_s when calculating their scattering efficiency factors for size parameter $\chi = \pi n_2 d_s/\lambda$ less that 5-15 where n_2 is the refraction index of the surrounding medium and λ is the wavelength of the incident radiation in a vacuum. In fact, the scattering cross-section of spheroids computed using the T-matrix method was found to be up to 30% smaller than that of equivalent spheres with the same cross-sectional areas for $\chi \approx 1$. The difference in scattering cross-sections between spheroids and equivalent spheres was found to decrease as the size parameter increases. Note that in the present study, the size parameters χ for the different microalgae were larger than 60. Thus, previous studies confirmed the view that treating microalgae with aspect ratio less than 1.5 as spherical can be applied to infer their optical properties from their measured absorption and scattering coefficients

[44, 45, 103–105].

Recently, Berberoğlu and co-workers [3, 43] experimentally measured the radiation characteristics of several H_2 producing microorganisms namely (a) purple non-sulfur bacteria *R.sphaeroides* [43], (b) cyanobacteria *A.variabilis* [43], and (c) green algae *Chlamydomonas reinhardtii* strain CC125 and its truncated chlorophyll antenna transformants *tla1*, *tlaX*, and *tla1-CW*$^+$ [3]. The authors also measured the radiation characteristics of the lipid producing microalgae *C. littorale*, *B. braunii*, and *Chlorella sp.* [51]. Except for the purple bacteria *R.sphaeroides* which absorbs in the near infrared, the absorption coefficients of these microorganisms vanish beyond 750 nm when only scattering contributes to extinction. For example, the wild strain *C.reinhardtii* CC125 absorbs mainly in the spectral region from 300 to 700 nm with absorption peaks at 435 and 676 nm corresponding to absorption peaks of *in vivo* chlorophyll *a*. It also has additional absorption peaks at 475 and 650 nm corresponding to absorption by chlorophyll *b*. Berberoğlu *et al.* [3] also showed that the genetically engineered strains of *C.reinhardtii* have less chlorophyll pigments than the wild strain and thus have smaller absorption cross-sections. In particular, the mutant *tlaX* featured a significant reduction in chlorophyll *b* concentration. For all mutants, the reduction in their absorption cross-section was accompanied by an increase in their scattering cross-section.

3.2.2 Effective Optical Properties of Microorganisms

3.2.2.1 Direct Experimental Measurements

The refraction index n_λ of microalgae can be measured directly [45, 106–108]. However, the experimental measurements are complicated by the polydispersion of the microbial particles and by light absorption. On the other hand and to the best of our knowledge, no method has been reported in the literature to directly measure the absorption index k_λ of microbial particles in suspension.

First, photometric immersion refractometry consists of suspending the cells in a medium of known refraction index and measuring the transmittance T_λ or the optical density (OD) of the suspension defined as $\text{OD}_\lambda = \text{-log}T_\lambda$ [109,110] at a non-absorbing wavelength. For example an aqueous solution of bovine serum albumin (BSA) can be used as the immersion medium as it is not toxic to microorganisms. Solutions with different refraction indices can be prepared by varying the BSA concentration [111]. The OD of the suspension is then measured as a function of BSA concentration. The refraction index of the microbial cells at the wavelength considered is taken as that of the BSA solution corresponding to the minimum OD.

Flow cytometry can also be used to directly measure the refraction index n_λ of microalgae [107, 108]. Collimated laser radiation is directed at a stream of saline solution containing microbial particles. The latter are assumed to be homogeneous spheres despite their potentially irregular morphologies. The intensities of forward scattered light (typically at an angle of 1-19° with respect to the incident beam direction), side scattered light (54-126°), and chlorophyll fluorescence (660-700 nm) are measured [107]. The system is calibrated using standard suspensions consisting of polydisperse spherical particles of known refraction index such as oil globules and glass beads. For every individual cell, different intensities of the forward and side scattered light are measured depending on their size, shape, and refraction index. The refraction index is found by fitting the experimental measurements and comparing with standards suspensions.

Finally, the abundance of refraction index data for various species of phytoplankton has been used to correlate the refraction index n_λ to the intracellular carbon concentration in the form [44]

$$n_\lambda = n_{0,\lambda} + n_{1,\lambda} C_c \tag{3.3}$$

where $n_{0,\lambda}$ and $n_{1,\lambda}$ are constants determined by experimental procedures and

C_c is the intracellular carbon concentration (in kg/m^3). For example, DuRand and Olson [112] reported $n_{0,\lambda} = 1.02$ and $n_{1,\lambda} = 0.000117$ for *Nannochloris sp.* at 665 nm. Unfortunately, most of the above methods measured the refraction index at a single wavelength. It then has to be assumed constant over the PAR for spectral calculations of light transfer in the suspension and estimation of the average fluence rate available in PBRs and necessary in growth kinetic models [39, 44, 113, 114].

The intracellular pigments such as chlorophylls and carotenoids are typically extracted by using organic solvents which penetrates through the cell membrane and dissolves the lipids to extract pigments [115, 116]. Methanol, acetone, and ethanol are usually used as the organic solvents in the pigments extraction process [117, 118]. Overall, measuring the pigment concentration can be very time consuming and suffers from various and sometimes large experimental uncertainties [115].

3.2.2.2 Model-Based Measurements

Despite their heterogeneous morphologies, microalgae have typically been treated as homogeneous with some effective refraction and absorption indices. Stramski and Mobley [93] experimentally measured the size distributions of various marine microbial particles and their spectral radiation characteristics in the PAR region (400 to 700 nm). The experimental data were used as input to an inverse method developed by Bricaud and Morel [45] to predict the complex refractive index of the particles under the assumptions that the particles were homogeneous and spherical. First, the absorption index was determined based on the anomalous diffraction approximation describing the absorption coefficient as a monotonic function of the absorption thickness parameter defined as $p' = 4\chi k_\lambda$ [99,119] where k_λ is the absorption index of the particle and $\chi = \pi d_s n_2/\lambda$ is the size parameter previously defined. For any given wavelength and particle size distribution, the absorption index was uniquely related to the absorption coefficient. Thus, for a given wavelength, the absorption index k_λ was varied iteratively until the calculated absorption coefficient matched its experimental value. Calculations were repeated for each wavelength to obtain the spectral absorption index. On the other hand, the refraction index n_λ was derived through an inverse method described by Stramski *et al.* [105]. Here, the Lorentz-Mie theory [98] was used instead of the anomalous diffraction approximation. The experimental data and the previously retrieved absorption indices were used as input parameters into the Lorentz-Mie theory code [98]. The refraction index was varied iteratively until the calculated extinction coefficient matched its experimental value. It was found that the measured microbial particles had absorption index ranging between 0 and 0.01 and refraction index between 1.38 and 1.42. The refraction index was found to vary by less than 5% in the PAR region for all microorganism species considered.

Pottier *et al.* [39] adopted a simpler approach to retrieve the refraction and absorption indices of *C.reinhardtii.* They measured the normal hemispherical transmittance of a suspension of *C.reinhardtii* at 820 nm where they do not absorb. The corresponding refraction index was found to be 1.527 and assumed to be constant over the PAR. Then, the authors estimated the spectral absorption index k_λ according to [39]

$$k_\lambda = \frac{\kappa_\lambda \lambda}{4\pi} = \frac{\lambda}{4\pi}\rho_{dm}\frac{1-x_w}{x_w}\sum_{i=1}^{N} Ea_i w_i \tag{3.4}$$

where pigment mass fractions w_i were estimated experimentally.

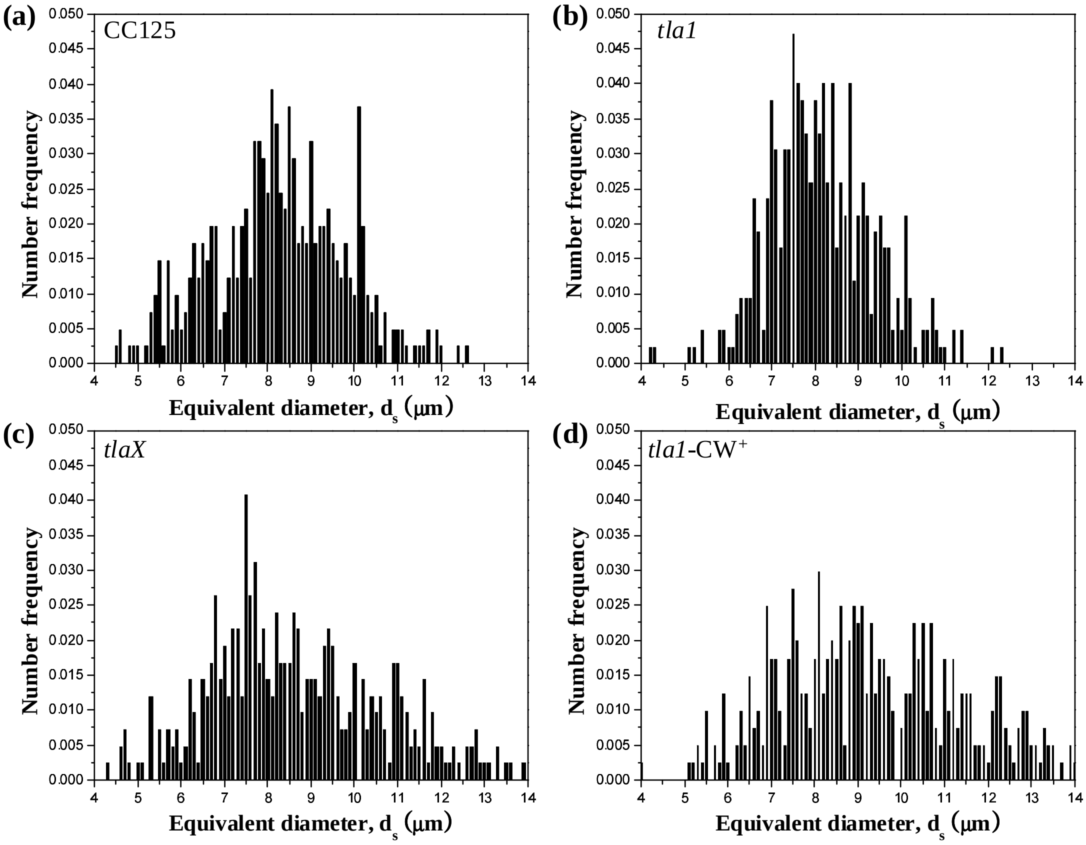

Figure 3.1: Number frequency $f(d_s)$ of the equivalent sphere diameter of (a) *C.reinhardtii* CC 125 (c=0.989, ϵ=1.149) and its truncated chlorophyll antenna transformants (b) *tla1* (c=0.996, ϵ=1.073), (c) *tlaX* (c=0.979, ϵ=1.220), and (d) *tla1-CW^+* (c=0.986, ϵ=1.173). The equivalent diameter was estimated from Equation (3.6) and major and minor diameter distributions reported in Figure 2 in Ref. [3].

3.3 Analysis

3.3.1 Assumptions

In the present study, the different microalgae were assumed to be spherical. This assumption simplifies the calculations of their radiation characteristics by using the Lorentz-Mie theory instead of the T-matrix method. It has been validated by Quirantes and Bernard [95] and its validity for the microalgae of interest will be discussed later. Moreover, despite their heterogeneous structure, microalgae were treated as homogeneous with some effective refraction and absorption indices. Note that n_λ was treated as wavelength-dependent over the PAR, unlike what previous studies have often assumed [39].

3.3.2 Equivalent diameter and size distribution

The different microalgae were treated as homogeneous spheres with an equivalent diameter such that their surface area was identical to that of their actual spheroidal shape assumed to be axisymmetric [95, 120, 121]. The polar radius of an axisymmetric spheroid in the spherical coordinate system is given by [23]

$$r\left(\theta\right) = \frac{a}{2}\left(sin^2\theta + \frac{a^2}{b^2}cos^2\theta\right)^{-1/2} \tag{3.5}$$

where θ is the polar angle, while a and b are the major and minor diameters, respectively. The spheroid aspect ratio is defined as $\epsilon = a/b$. Note that ϵ is always greater than 1.0 since a is the major diameter [23]. The equivalent diameter of the sphere having the same surface area as the spheroid is given by [23]

$$d_s = \frac{1}{2}\left(2a^2 + 2ab\frac{\sin^{-1}e}{e}\right)^{1/2} \qquad \text{where} \qquad e = \frac{\left(\epsilon^2 - 1\right)^{1/2}}{\epsilon} \tag{3.6}$$

Moreover, the number frequency of equivalent diameter d_s denoted by $f(d_s)$ is defined as,

$$f(d_s) = \frac{N(d_s)}{\int\limits_o^\infty N(d_s)\mathrm{d}d_s} = \frac{N(d_s)}{N_T} \tag{3.7}$$

where $N(d_s)$ is the number of cells per unit volume of suspension having diameter between d_s and $d_s + \mathrm{d}d_s$. The denominator on the right-hand side of Equation (3.7) is the total cell concentration N_T expressed in total number of cells per m^3 of suspension.

Berberoğlu *et al.* [3,51] reported the size distribution for the minor and major diameters $N(a)$ and $N(b)$ for each *C.reinhardtii* strain (see Figure 2 in Ref. [3]). Their average circularity is defined as $c = 4\pi \times A_S/P^2$ where A_S and P are the cell's surface area and perimeter. The authors used the image analysis software ImageJ [122] to measure their minor and major diameters assuming the cells to be 2D ellipses. Then, the surface area and perimeter of axisymmetric spheroids were calculated as $A_S = \pi ab/4$ and $P = 2\pi\sqrt{2\left(a^2 + b^2\right)}$, respectively. The circularity of *C.reinhardtii* CC125, *tla1*, *tlaX*, and *tla1-CW*$^+$ was 0.989, 0.996, 0.979, and 0.986, respectively while their average aspect ratio ϵ was 1.149, 1.073, 1.220, and 1.173, respectively. Their circularity was equal to 0.961, 0.965, and 0.975 while their average aspect ratio ϵ was 1.333, 1.301, and 1.212, respectively.

Finally, Figure 3.1 shows the number frequency $f(d_s)$ of the equivalent diameter d_s for *C.reinhardtii* CC125 and its truncated chlorophyll antenna transformants. It was calculated from experimentally measured major and minor diameters using Equation (3.6).

3.3.3 Prediction of the Radiation Characteristics of Microalgae

The Lorentz-Mie theory predicts the absorption and scattering cross-sections denoted by $C_{abs,\lambda}(d_s)$ and $C_{sca,\lambda}(d_s)$ (expressed in m^2) of an individual spherical cell of diameter d_s with complex index of refraction $n_\lambda + ik_\lambda$ submerged in phosphate buffered saline (PBS) solution with refraction index n_{PBS}. Then, the absorption coefficient κ_λ of a microorganism suspension with size distribution $N(d_s)$ is expressed as [42],

$$\kappa_\lambda = \int_o^\infty C_{abs,\lambda}(d_s)N(d_s)\mathrm{d}d_s = \bar{C}_{abs,\lambda}N_T \tag{3.8}$$

Similarly, the effective scattering coefficient of the microorganisms $\sigma_{s,\lambda}$ can be written as [123],

$$\sigma_{s,\lambda} = \int_o^\infty C_{sca,\lambda}(d_s)N(d_s)\mathrm{d}d_s = \bar{C}_{sca,\lambda}N_T \tag{3.9}$$

Here, $\bar{C}_{abs,\lambda}$ and $\bar{C}_{sca,\lambda}$ are the average absorption and scattering cross-sections of the microalgae in suspension (in m^2), respectively. These average cross-sections can effectively be measured for typically polydisperse microalgae population. In fact, Berberoğlu *et al.* [51] measured the average absorption and scattering cross-sections $\bar{C}_{abs,\lambda}$ and $\bar{C}_{sca,\lambda}$ for *B. braunii*, *Chlorella sp.*, and *C. littorale.* Thus, the predictions from Lorentz-Mie theory and Equations (3.8) and (3.9) could be directly compared with experimental data.

Berberoğlu *et al.* [3] measured the average mass absorption and scattering cross-sections of *C.reinhardtii* and its mutants denoted by $\bar{A}_{abs,\lambda}$ and $\bar{S}_{sca,\lambda}$, expressed in m^2/kg, and defined as

$$\bar{A}_{abs,\lambda} = \kappa_\lambda/X \qquad \text{and} \qquad \bar{S}_{sca,\lambda} = \sigma_{s,\lambda}/X \tag{3.10}$$

where X is the microorganism concentration expressed in kilogram of dry cell weight per cubic meter of liquid medium. The average absorption and scattering cross-sections $\bar{C}_{abs,\lambda}$ and $\bar{C}_{sca,\lambda}$ can be calculated from the average mass absorption and scattering cross-sections $\bar{A}_{abs,\lambda}$ and $\bar{S}_{sca,\lambda}$ according to [39],

$$\bar{C}_{abs,\lambda} = \bar{A}_{abs,\lambda}V_{32}\rho_{dm}(1-x_w) \qquad \text{and} \qquad \bar{C}_{sca,\lambda} = \bar{S}_{sca,\lambda}V_{32}\rho_{dm}(1-x_w) \tag{3.11}$$

where the density of *C.reinhardtii* and its mutants ρ_{dm} was taken as 1350 kg/m^3 as reported in the literature [124]. Their mean particle volume V_{32} was computed from their respective Sauter mean diameter as 3.36×10^{-16} m^3 for CC125, 3.04×10^{-16} m^3 for *tla1*, 4.27×10^{-16} m^3 for *tlaX*, and 5.24×10^{-16} m^3 for *tla1-CW*$^+$. Note that Pottier *et al.* [39] used a similar value of $V_{32} = 3.19 \times 10^{-16}$ m^3 for their *C.reinhardtii* strain. Finally, x_w was taken as 0.78 for *C.reinhardtii* and its mutants [39].

3.3.4 Optimization Algorithm

Figure 3.2 shows the schematic diagram of the procedure used to simultaneously retrieve the spectral refraction index n_λ and the absorption index k_λ. The Lorentz-Mie theory [89] was employed in the forward model to calculate the spectral average absorption and scattering cross-sections $\bar{C}_{abs,\lambda}$ and $\bar{C}_{sca,\lambda}$ over the PAR.

Various optimization algorithms can be used to efficiently and simultaneously determine n_λ and k_λ. The objective is to find the values of these parameters that minimize the difference between the predicted and experimentally measured absorption and scattering cross-sections of the microalgal suspension in the least-square sense. Genetic algorithm can find a global minimum of an objective function using the concept of evolution theory [125]. A given set of input parameters [e.g., (n_λ, k_λ)] is called an individual and each parameter is called a gene. The numerical procedure starts with a randomly generated population consisting of numerous individuals. The objective function (or fitness function) is calculated for each individual of the population and estimates some difference between experimental measurements and model predictions. Individuals with the largest value of the objective function are dismissed. Those with the smallest objective function are selected to form a new population. Breeding of the new generation consists of producing new individuals by recombination and random mutation of the genes of an arbitrary pair of individuals. The fitness function is evaluated for each individual and the procedure is repeated generation after generation until the objective function falls below a given convergence criterion. This method tends

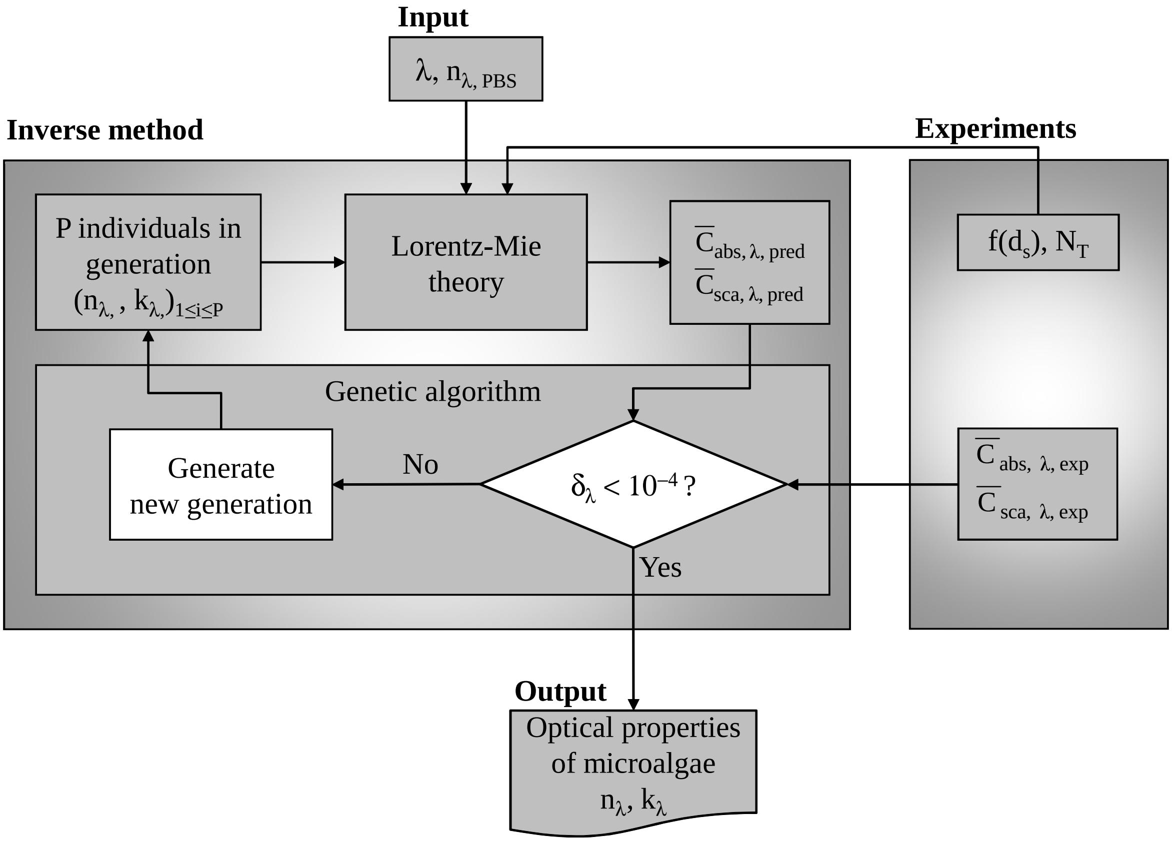

Figure 3.2: Block diagram of the procedure used to retrieve the refraction index n_λ and absorption index k_λ from the absorption and scattering cross-sections $\bar{C}_{abs,\lambda}$ and $\bar{C}_{sca,\lambda}$ at a given wavelength λ for number frequency $f(d_s)$. Individuals N=120 per generation for a maximum of 50 generations were used. n_λ and k_λ were allowed to range from 1.33 to 1.53 and from 10^{-5} to 0.01, respectively.

to be slow but it is robust and eventually converges to the global minimum [126].

In the present study, genetic algorithm was implemented using the general purpose function optimization code PIKAIA [127–129]. Here, the spectral refraction index n_λ was assumed to range from 1.33 to 1.53 based on the literature [39,130]. On the other hand, the absorption index k_λ was allowed to range from 10^{-5} to 0.01. For each wavelength, the objective function δ_λ was defined as,

$$\delta_\lambda = \left(\frac{\bar{C}_{abs,\lambda,pred} - \bar{C}_{abs,\lambda,exp}}{\bar{C}_{abs,\lambda,exp}} \right)^2 + \left(\frac{\bar{C}_{sca,\lambda,pred} - \bar{C}_{sca,\lambda,exp}}{\bar{C}_{sca,\lambda,exp}} \right)^2 \tag{3.12}$$

The genetic algorithm used a maximum of 50 generations with population of P=120 individuals. The convergence criteria was set as $\delta_\lambda < 10^{-4}$.

3.3.5 Experimental Uncertainties

Experimentally, the absorption and scattering cross-sections for each species were measured for three different microalgae concentrations. The maximum experimental uncertainties, with 95% interval confidence, associated with the absorption and scattering cross-sections were 6%, 8%, 16%, and 6% for *C.reinhardtii* CC125, *tla1*, *tlaX*, and *tla1-CW*$^+$, respectively. These experimental uncertainties propagated in the retrieved values of n_λ and k_λ. Thus, for all species, n_λ and k_λ were retrieved at wavelengths 435 and 676 nm, corresponding to Chl *a* absorption peaks, from the cross-sections $\bar{C}_{abs,\lambda} \pm \Delta\bar{C}_{abs,\lambda}$ and $\bar{C}_{sca,\lambda} \pm \Delta\bar{C}_{sca,\lambda}$ where $\Delta\bar{C}_{abs,\lambda}$ and $\Delta\bar{C}_{sca,\lambda}$ were equal to two standard deviations.

3.4 Results and Discussion

3.4.1 Validation: Retrieving n_λ and d_s of Monodisperse Latex Particles

Berberoğlu *et al.* [3] measured the scattering cross-section, between 400 and 800 nm, of monodisperse polystyrene latex spheres 5 μm in diameter in suspension in PBS solution. They used the same experimental procedure and analysis as that used to measure the radiation characteristics of the different microalgae considered in the present study. For validation purposes, the previously described inverse procedure and associated algorithm were used to retrieve the spectral refraction index as well as the diameter of spherical polystyrene latex particles using the measured scattering cross-section [3].

First, the absorption index of PBS in the visible was reported to be that of water [131] which is less than 4.0 $\times 10^{-8}$ [132]. The absorption index of polystyrene was reported to be less than 5.0×10^{-3} [133] between 400 and 700 nm. Thus, in the present study, the absorption index of both polystyrene and PBS were taken as k = 0.0 used as input parameters in the Lorentz-Mie theory. On the other hand, the refraction index of both PBS and polystyrene were modeled by the Cauchy dispersion relation expressed as [134]

$$n_\lambda = A + \frac{B}{\lambda^2} + \frac{C}{\lambda^4} \tag{3.13}$$

For PBS, the parameters A_{PBS}, B_{PBS}, and C_{PBS} were taken as $A_{PBS} = 1.32711$, $B_{PBS} = 2.6\times 10^{-3}$ μm^2, and C_{PBS}=5.0 $\times 10^{-5}$ μm^4 when λ was expressed in μm [131]. Then, the inverse method simultaneously retrieved the particle diameter d_s and the parameters A, B, and C using the objective function

$$\delta_\lambda = \sum_{i=1}^{9} \left(\frac{\bar{C}_{sca,\lambda_i,pred} - \bar{C}_{sca,\lambda_i,exp}}{\bar{C}_{sca,\lambda_i,exp}} \right)^2 \tag{3.14}$$

where the nine wavelengths λ_i were uniformly distributed between 400 and 700 nm. The parameters were found to be respectively d_s = 5.01 μm, A = 1.5555, B = 3.911×10^{-3} μm^2, and C = 3.867×10^{-4} μm^4. First, the polystyrene sphere diameter was retrieved very accurately. The values of parameters A, B, and C should be compared with those reported by Ma *et al.* [133] as A = 1.5725, B = 3.108×10^{-3} μm^2, and C = 3.4779 $\times 10^{-4}$. Comparison (not shown) of the refraction index of polystyrene retrieved here and that reported by Ma *et al.* [133] indicated that the relative error was less than 1.2% for all wavelengths between

400 and 800 nm. This is in excellent agreement and confirms the validity of the methodology and the proper implementation of the genetic algorithm.

3.4.2 Retrieved Spectral Complex Index of Refraction of Microalgae

3.4.2.1 *C.reinhardtii* CC125 and its truncated chlorophyll antenna transformants *tla1*, *tlaX*, and *tla1-CW*$^+$

This section presents the retrieved spectral complex index of refraction of *C.reinhardtii* CC125 and its truncated chlorophyll antenna transformants *tla1*, *tlaX*, and *tla1-CW*$^+$. The spectral complex index of refraction was retrieved at 36 different wavelengths uniformly distributed over the spectral region from 400 to 750 nm with 10 nm increments.

Figures 3.3(a) and 3.3(b) show the retrieved effective refraction and absorption indices of *C.reinhardtii* CC 125 between 400 and 750 nm, respectively. Here, the microalgae were assumed to be spherical with (i) the major diameter number frequency $f(a)$ and (ii) the minor diameter number frequency $f(b)$, or with (iii) the equivalent diameter number frequency $f(d_s)$ shown in Figure 3.1. In all cases, the retrieved value of n_λ of *C.reinhardtii* CC 125 was slightly dependent on wavelength but significantly different from the constant value of 1.527 assumed by Pottier *et al.* [39]. Instead, the retrieved value of n_λ was around 1.36 which is similar to the refraction index of phytoplanktons reported in the literature [130]. Note that the effective refraction index retrieved by using the major and the minor diameter number frequency differed from that obtained using the equivalent diameter distribution by less than 0.3% in the wavelength range considered. Moreover, the maximum relative differences between the retrieved absorption index k_λ using the equivalent diameter d_s and that using the major and the minor diameter distributions was 23%. In other words, the retrieved k_λ was more sensitive to the size distribution than n_λ. For both n_λ and k_λ, the values retrieved using $f(a)$ and $f(b)$

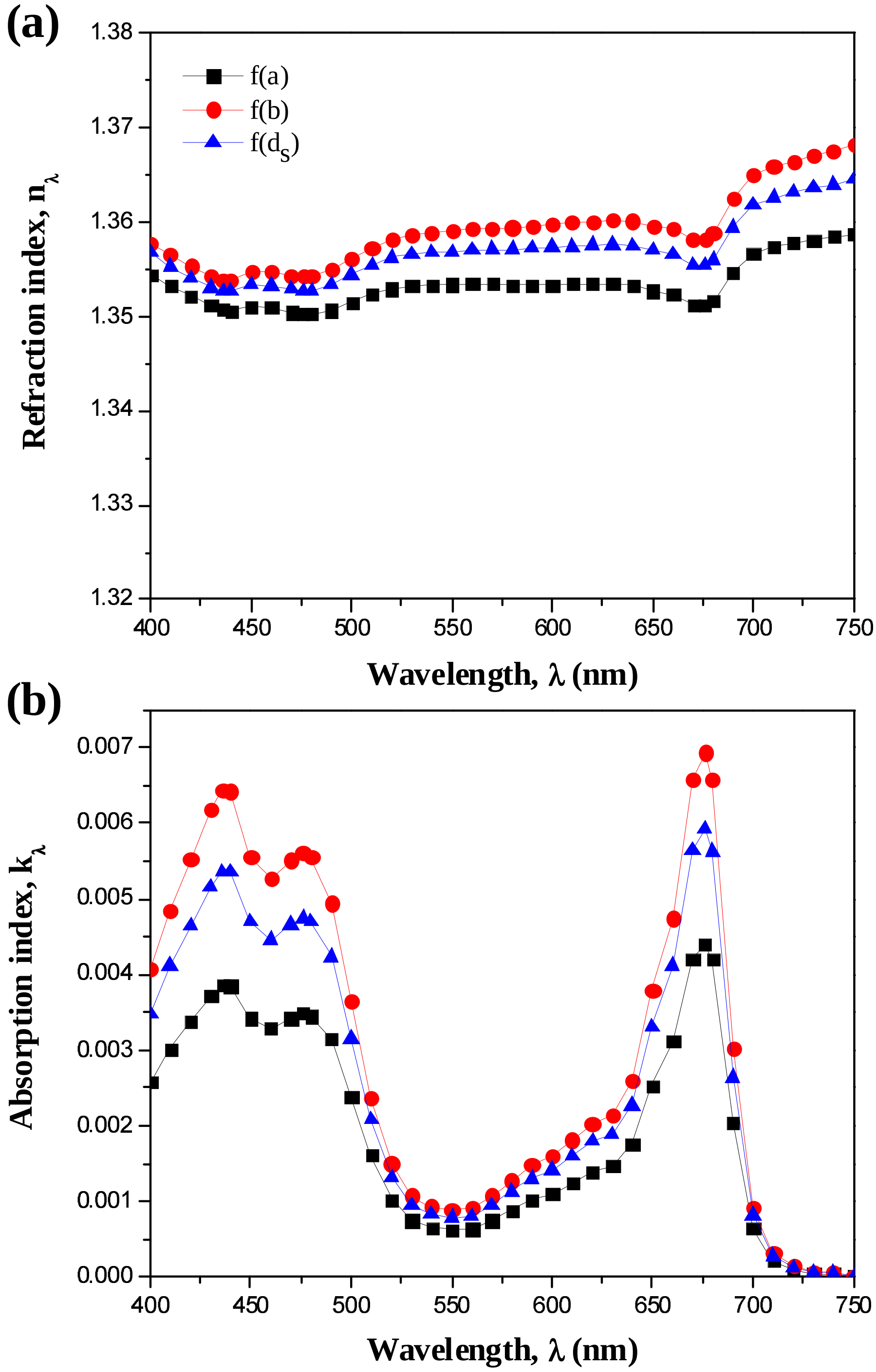

Figure 3.3: Comparison of the retrieved refraction and absorption indices between 400 and 750 nm for the green algae *C.reinhardtii* CC 125 using major, minor, and equivalent diameter distributions $f(a)$, $f(b)$, and $f(d_s)$, respectively.

provided the upper and lower bounds for those retrieved using $f(d_s)$, respectively.

Figure 3.4(a) and (b) respectively compare the effective refraction and absorption indices for *C.reinhardtii* CC 125 and its truncated chlorophyll antenna transformants *tla1*, *tlaX*, and *tla1-CW*$^+$ between 400 and 750 nm. Here, n_λ and k_λ were retrieved using the equivalent diameter distribution $N(d_s)$. Figure 3.4(a) indicates that n_λ ranged between 1.350 and 1.365 between 400 and 750 nm. Overall, n_λ varied slightly from one strain to another. On the other hand, Figure 3.4(b) clearly shows that the absorption index decreases from CC 125 to *tla1-CW*$^+$, *tla1*, and *tlaX* corresponding to a reduction in the size of their chlorophyll antenna. A significant decrease in k_λ was apparent for *tlaX* at wavelength 475 nm corresponding to a decrease in Chl *b* concentration caused by genetic engineering. In addition, *tla1-CW*$^+$ features an absorption index larger than *tla1* possibly due to the presence of a cell wall [38]. It is also interesting to note that (i) the retrieved n_λ and k_λ were continuous functions of wavelength and that (ii) the absorption peaks of *in vivo* Chl *a* at 435 and 676 nm and Chl *b* at 475 and 650 nm were distinctly apparent. This further provides confidence in the inverse method and the results since both n_λ and k_λ were retrieved for each wavelength independently.

Finally, Figure 3.5 compares the spectral absorption and scattering cross-sections measured experimentally and those predicted by Equation (3.8) using the Lorentz-Mie theory and the retrieved value of the optical properties of each *C.reinhardtii* strains between 400 and 750 nm. It shows excellent agreement at all wavelengths. The average relative and maximum errors between experimental measurements and the predictions between 400 and 700 nm were respectively (i) less than 0.3% and 1.4% for the average absorption cross-section $\bar{C}_{abs,\lambda}$ and (ii) less than 0.2% and 0.8% for the average scattering cross-section $\bar{C}_{sca,\lambda}$ for all strains.

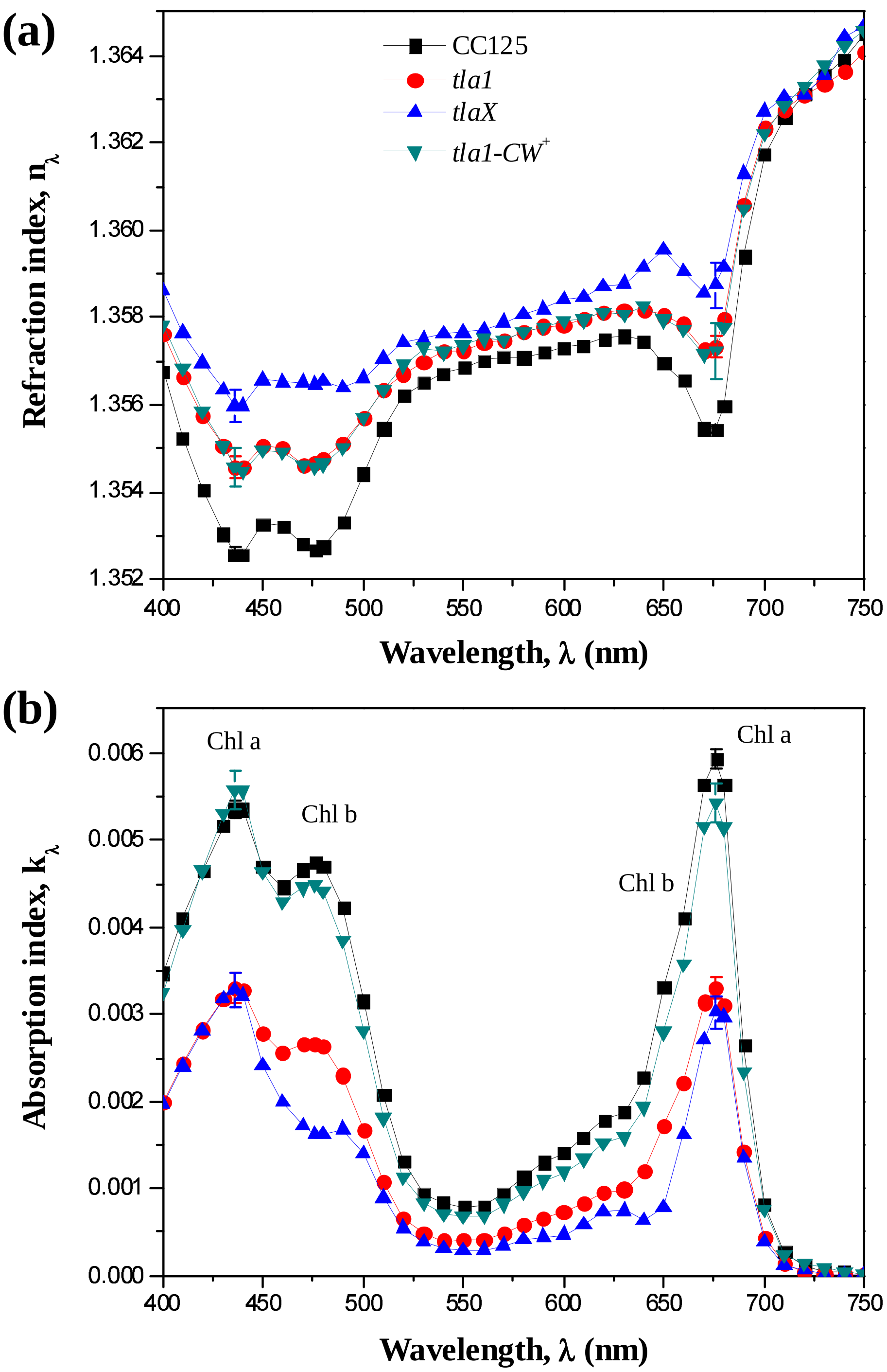

Figure 3.4: Comparison of the retrieved refraction and absorption indices between 400 and 750 nm for the green algae *C.reinhardtii* CC 125 and its truncated chlorophyll antenna transformants *tla1*, *tlaX*, and *tla1-CW*$^+$ using their number frequency $f(d_s)$.

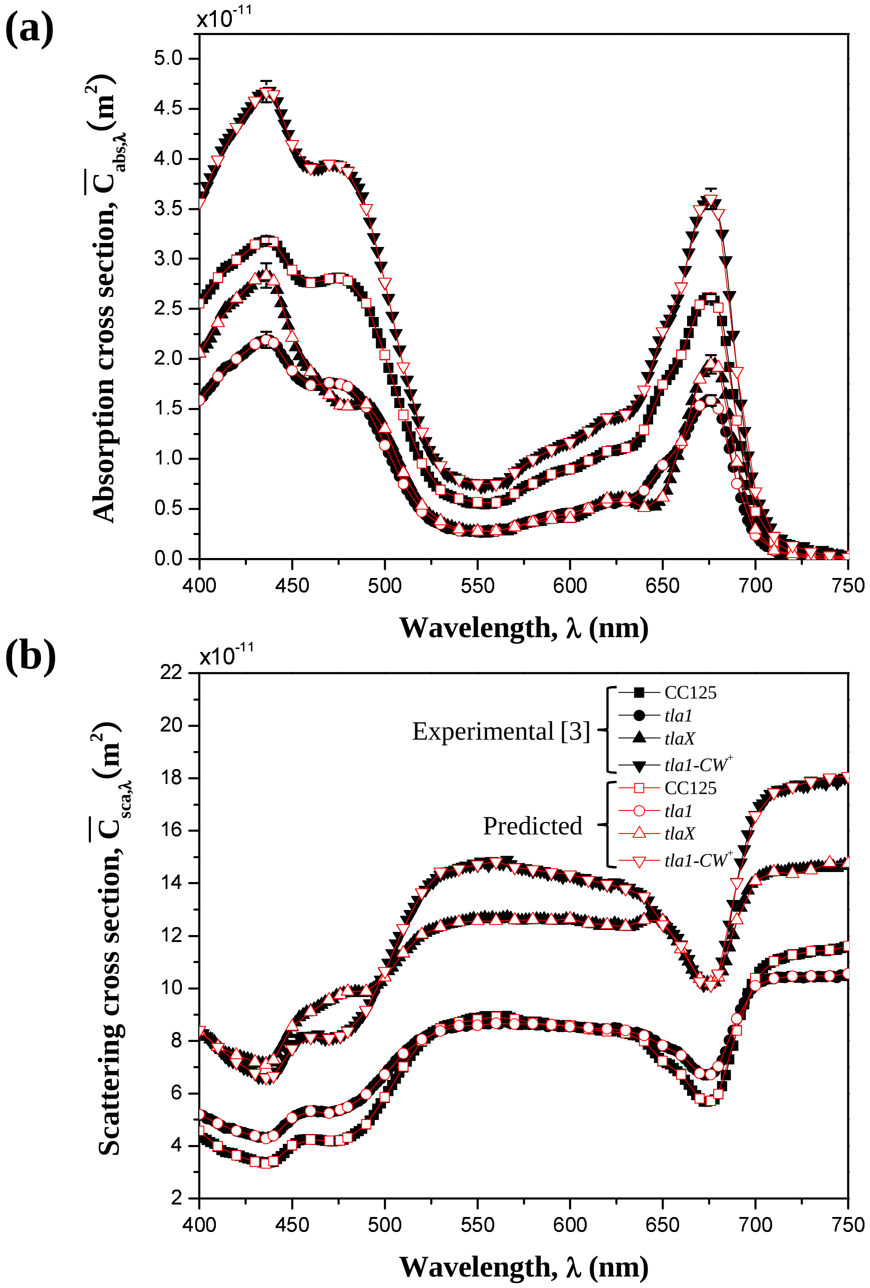

Figure 3.5: Comparison of the predicted and experimentally measured [3] average spectral absorption $\bar{C}_{abs,\lambda}$ and scattering $\bar{C}_{sca,\lambda}$ cross-sections of the green algae *C.reinhardtii* CC 125 and its truncated chlorophyll antenna transformants *tla1*, *tlaX*, and *tla1-CW*$^+$. Experimental data [3] for $\bar{A}_{abs,\lambda}$ and $\bar{S}_{sca,\lambda}$ were converted to $\bar{C}_{abs,\lambda}$ and $\bar{C}_{sca,\lambda}$ using Equations (3.10) and (3.11), respectively.

3.4.3 Discussion

3.4.3.1 Retrieved Optical Properties

Figures 3.4(a) indicates that the refraction index n_λ of all microorganisms features a small dip around 676 nm corresponding to a peak in k_λ caused by Chl *a* absorption. Such a dip was also observed around the same wavelength for various phytoplankton species as illustrated in Figures 6.14 and 6.20 in Ref. [44]. This can be attributed to oscillator resonance around 676 nm. It can also be predicted by optical constant theory such as the Lorentz model [98] or the Helmholtz-Kettler theory [44]. Figures 3.4 also shows the error bars associated with the retrieved values of n_λ and k_λ resulting from the error propagation of uncertainties in the measured $\bar{C}_{abs,\lambda}$ and $\bar{C}_{sca,\lambda}$. The relative error corresponding to 95% confidence interval, associated with n_λ and k_λ was less than 0.1% and 7%, respectively for all the species considered. The absorption index was more sensitive to the experimental uncertainties than the refraction index. Nevertheless, the error propagation from the experimental measurements of $\bar{C}_{abs,\lambda}$ and $\bar{C}_{sca,\lambda}$ to the retrieved complex index of refraction was acceptable.

It is also important to note that the good agreement between measured and predicted cross-sections $\bar{C}_{abs,\lambda}$ and $\bar{C}_{sca,\lambda}$ reported for all species considered could not be obtained when (i) the refraction index n_λ of the microalgae was assumed to be constant over the PAR and (ii) k_λ was retrieved by optimizing the pigment mass fractions w_i for Chl *a*, Chl *b*, and PPC in Equation (3.2). In other words, despite the fact that n_λ varies slightly over the PAR, it should not be treated as constant in predicting the microalgae absorption and scattering cross-sections.

3.4.3.2 Retrieved Pigment Concentrations of Microalgae

The mass fractions of the three pigments Chl *a*, Chl *b*, and photoprotective carotenoids (PPC), denoted by w_a, w_b, and w_{PPC}, were estimated simultaneously

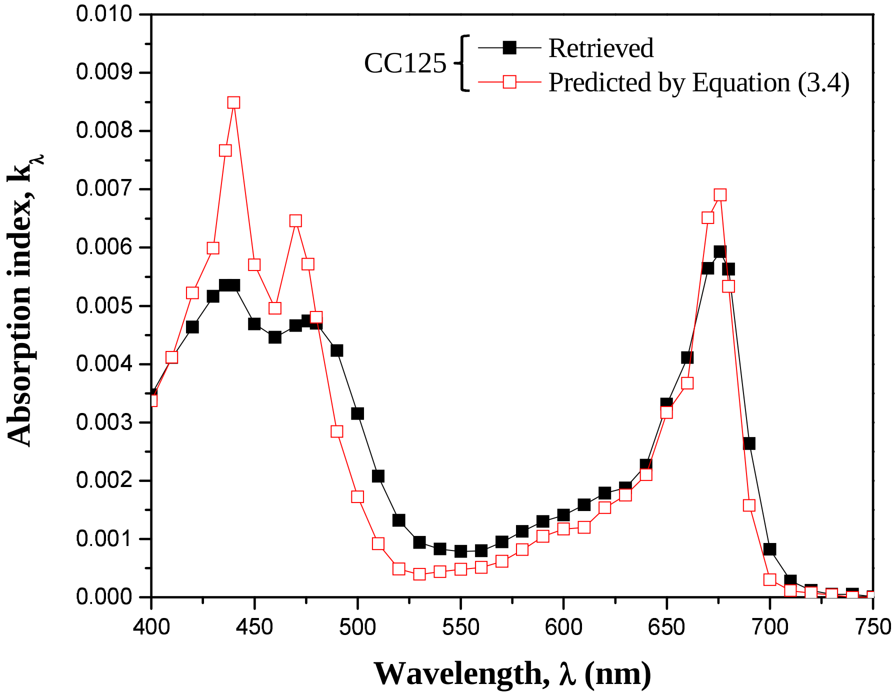

Figure 3.6: Comparison between the retrieved absorption index k_λ and those predicted by Equation (3.4) for *C.reinhardtii* with w_a = 16.50 g/kg, w_b = 9.68 g/kg, and w_{PPC} = 1.98 g/kg.

from the retrieved absorption index k_λ for all species considered. The inverse method was also based on genetic algorithm and PIKAIA to minimize the objective function defined as

$$\Delta_\lambda = \sum_{i=1}^{36} \left(\frac{k_{\lambda_i,pred} - k_{\lambda_i}}{k_{\lambda_i}} \right)^2 \tag{3.15}$$

where $k_{\lambda_i,pred}$ is the absorption index predicted by Equation (3.4) as a function of w_a, w_b, and w_{PPC}. Note that this approach relies on the validity of Equation (3.4) and the database of *in vivo* spectral mass absorption coefficient Ea of various pigments reported in Ref. [2] and shown in Figure 1.2.

Figure 3.6 compares the absorption index previously retrieved and that predicted by Equation (3.4) for *C. reinhardtii* CC 125 based on the fitted values w_a = 16.50 g/kg, w_b = 9.68 g/kg, and w_{PPC} = 1.98 g/kg. These values are in the same range as those measured by Pottier *et al.* [39] as $w_a = 14.00$ g/kg, $w_b = 7.00$ g/kg, $w_{PPC} = 4.50$ g/kg. It indicates that the previously retrieved k_λ and that predicted using the fitted pigment mass fractions were in fair agreement despite the inverse method used to minimize their difference. For example, the relative error between $k_{\lambda,pred}$ and k_λ for *C. reinhardtii* CC 125 at the absorption peaks of Chl *a* at 435 and 676 nm were 43% and 16%, respectively.

It is important to mention that Equations (3.1) and (3.4) are valid for a hypothetical slab of homogeneous and non-scattering microalgae materials for which the absorption coefficient is given by $\kappa_\lambda = 4\pi k_\lambda/\lambda$. The present results suggest that these equations apply only approximately to heterogeneous and spherical or spheroidal microalgae.

3.4.3.3 Compatibility with T-Matrix Method

The above analysis and results rely on the assumptions that the different microalgae can be treated as spherical. However, their circularity and aspect ratio were not exactly unity [3, 51]. Figure 3.6 compares the average absorption and scattering cross-sections $\bar{C}_{abs,\lambda}$ and $\bar{C}_{sca,\lambda}$ for *C. reinhardtii* CC 125 measured experimentally with those predicted by the T-matrix method using the retrieved values of n_λ and k_λ to assess the validity and consequences of this assumption. The predictions used (i) the average aspect ratio ϵ=1.149 for *C. reinhardtii* CC 125, (ii) their equivalent diameter distribution $f(d_s)$ shown in Figures 3.1, and (iii) their refraction and absorption indices retrieved using Lorentz-Mie theory shown in Figures 3.4. The results show that accounting for the non-sphericity of microalgae via the T-matrix method had relatively small effect on both $\bar{C}_{abs,\lambda}$ and $\bar{C}_{sca,\lambda}$. In fact, the maximum relative difference between T-matrix predictions and experimental data for both $\bar{C}_{abs,\lambda}$ and $\bar{C}_{sca,\lambda}$ was 1.8%. Similar or better results were obtained for the other species since their average aspect ratio was closer to unity when Lorentz-Mie theory is valid.

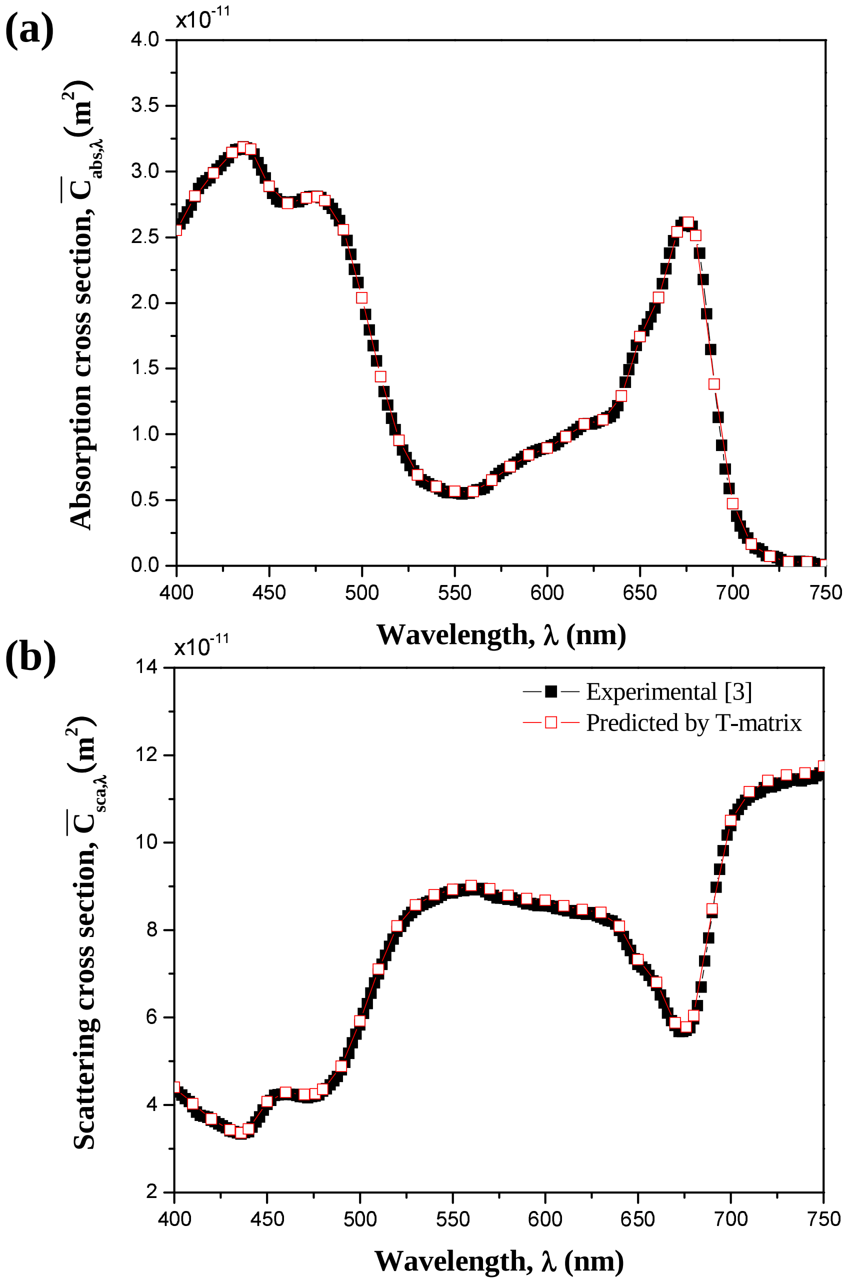

Figure 3.7: Comparison of the prediction by T-matrix and experimental measurement [3] for average spectral absorption $\bar{C}_{abs,\lambda}$ and scattering $\bar{C}_{sca,\lambda}$ cross-sections of the green algae *C.reinhardtii* CC 125. Experimental data [3] for $\bar{A}_{abs,\lambda}$ and $\bar{S}_{sca,\lambda}$ were converted to $\bar{C}_{abs,\lambda}$ and $\bar{C}_{sca,\lambda}$ using Equations (3.10) and (3.11), respectively.

Overall, the effective refraction and absorption indices n_λ and k_λ retrieved over the PAR for all species considered in the present study can be used in the Lorentz-Mie theory or in the T-matrix method along with their size distribution to accurately predict their radiation characteristics.

3.5 Conclusions

This chapter presented and used a methodology to retrieve the spectral refraction and absorption indices of biofuel producing microalgae from experimentally measured average absorption and scattering cross-sections between 400 and 750 nm. The microalgae were treated as spherical particles with equivalent diameter distributions calculated from experimentally measured major and minor diameter distributions. An inverse method was developed combining Lorentz-Mie theory as the forward method and genetic algorithm. The retrieved refraction and absorption indices were continuous function of wavelength with apparent absorption peaks corresponding to those of *in vivo* Chl *a* and *b*. These optical properties can be used to predict the radiation characteristics of the species considered using Lorentz-Mie theory or the T-matrix method for a given size distribution and average aspect ratio.

CHAPTER 4

Radiation Characteristic of Filamentous Microorganisms

In Chapter 3, the green microalgae *C. reinhardtii* were spheroidal. However, there are many other photosynthetic microorganisms with different shapes including filamentous cyanobacteria. This chapter presents predictions of the radiation characteristics of filamentous cyanobacteria using the T-matrix method.

4.1 Introduction

Radiation characteristics of suspended microorganisms depend largely on their size, shape, pigment composition, internal structure, and optical properties [97]. Figure 4.1 shows micrographs of (a) filamentous cyanobacteria *A.cylindrica* consisting of dozens of connected spherical cells 2-4 μm in diameter and (b) filamentous cyanobacteria *A.variabilis* with heterocysts and vegetative cells 4-6 μm in diameter. Their morphology could be modeled as connected, aligned, spherical, and homogeneous cells. Then, their radiation characteristics can be numerically predicted by the T-matrix method [22]. However, the method is very time consuming particularly, for the length and size of these microorganisms. Alternatively, from a radiation standpoint, these microorganisms in a well-mixed suspension could potentially be modeled as infinitely long and randomly oriented cylinders. Then, their absorption and scattering cross-sections could be predicted by Lorentz-Mie theory for cylinders [89]. However, it remains unclear how valid this approach is

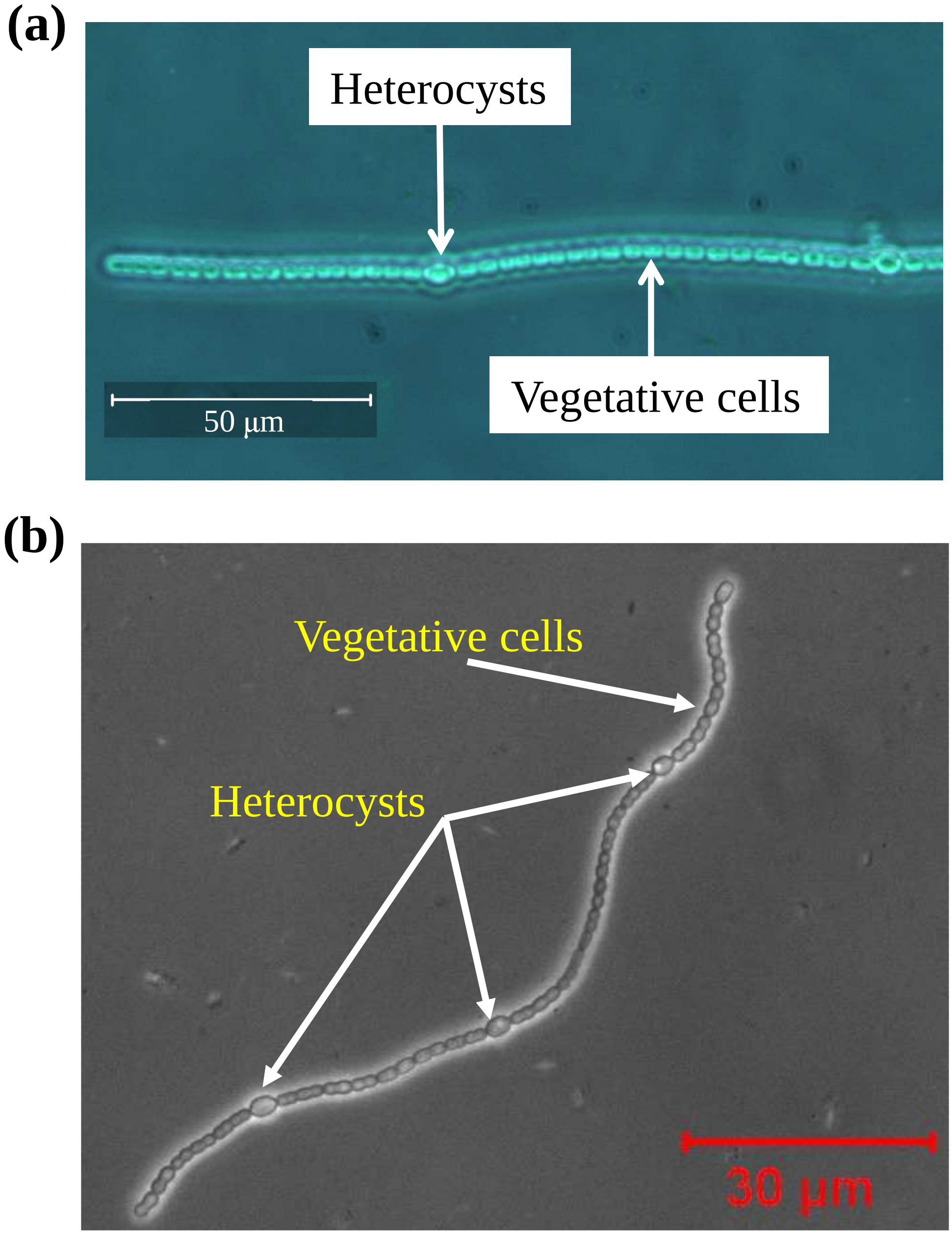

Figure 4.1: Micrographs of (a) filamentous cyanobacteria *A.cylindrica* [4] and (b) filamentous cyanobacteria *A.variabilis* grown in our laboratory [16].

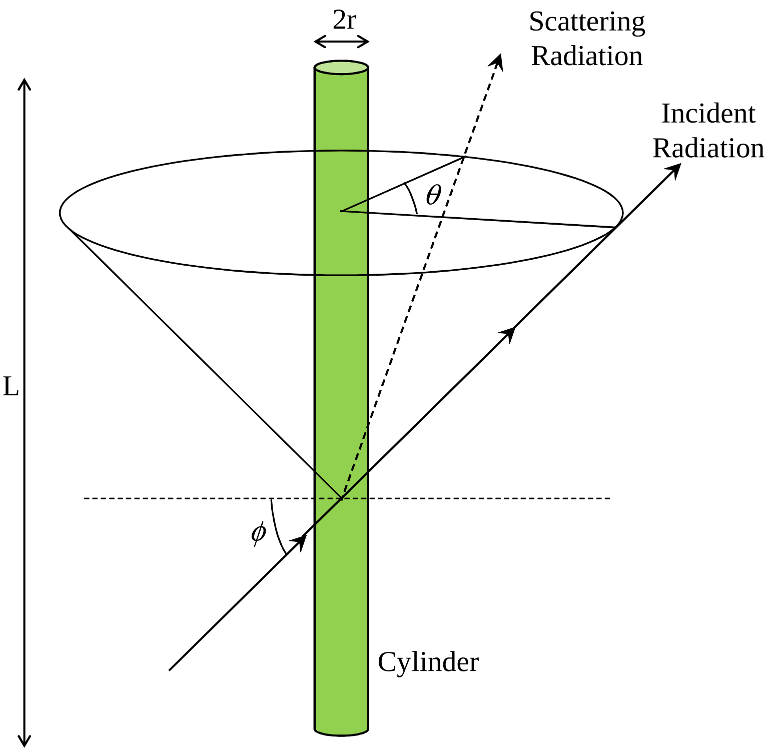

Figure 4.2: Scattering of incident radiation at incident angle of ϕ by a infinitely long cylinder [17].

and what radius the cylinder should have. For example, the radius of the representative cylinder could be such that the cylinder features the same surface area or the same volume as the row of spheres.

4.2 Background

4.2.1 Lorentz-Mie Theory for Infinitely Long Cylinders

The Lorentz-Mie theory used to predict the absorption and scattering cross-sections of infinitely long cylinders is now well established [98]. Cylinders can be treated as infinitely long provided that their length L is much larger than their diameter $2r$, i.e., $L \gg 2r$ [98]. Figure 4.2 illustrates scattering by an infinitely long cylinder of radiation incident at an angle ϕ with respect to the normal of the cylinder axis [17]. The scattered radiation propagates along the conical surface defined by the apex angle of $\pi/2 - \phi$. The direction of the scattered radiation is measured azimuthally relative to the incident radiation by the angle θ. The extinction and scattering cross-sections, denoted by C'_{ext} and C'_{sca}, per unit length (in m^2/m) of a single infinitely long cylinder of radius r for a given incident direction ϕ are defined as [42]

$$C'_{ext}(m\chi, \phi) = 2rQ_{ext}(m\chi, \phi) = \frac{2\lambda}{\pi}\text{Re}\left\{T(\theta = 0)\right\} \tag{4.1}$$

$$C'_{sca}(m\chi, \phi) = 2rQ_{sca}(m\chi, \phi) = \frac{\lambda}{\pi^2}\int_0^{2\pi} i(\theta, \phi)d\theta \tag{4.2}$$

where $m = n + ik$ is the relative complex index of refraction of the cylinder with respect to that of the non-absorbing surrounding medium and $\chi = 2\pi r/\lambda$ is the cylinder size parameter Here, $T(\theta)$ is the scattering amplitude function and $i = |T(\theta)|^2$ is the angular distribution of the scattered intensity. In addition, $Q_{ext}(m\chi, \phi)$ and $Q_{sca}(m\chi, \phi)$ are the extinction and scattering efficiency factors, respectively. The cross-sections $C'_{ext}(m\chi, \phi)$ and $C'_{sca}(m\chi, \phi)$ can be expressed in terms of the Lorentz-Mie scattering coefficients a_n and b_n expressed in terms of Bessel and Hankel functions as [42],

$$C'_{ext}(m\chi, \phi) = \frac{\lambda}{\pi}\text{Re}\left\{b_{0,M} + a_{0,E} + 2\sum_{n=1}^{\infty}(b_{n,M} + a_{n,E})\right\} \tag{4.3}$$

$$C'_{sca}(m\chi, \phi) = \frac{\lambda}{\pi}\left\{|b_{0,M}|^2 + |a_{0,E}|^2 + \sum_{n=1}^{\infty}\left(|b_{n,M}|^2 + |b_{0,E}|^2 + |a_{n,M}|^2 + |a_{n,E}|^2\right)\right\} \tag{4.4}$$

Here, subscripts M and E refer to the transverse magnetic and transverse electric modes, respectively. In addition, the extinction and scattering cross-sections of infinitely long and randomly oriented cylinders can be found be averaging the angular cross-sections over the observation hemisphere according to [17]

$$\langle C'_{ext}(m\chi)\rangle = \int_0^{\pi/2} C'_{ext}(m\chi, \phi)\text{cos}\phi\text{d}\phi \tag{4.5}$$

$$\langle C'_{sca}(m\chi)\rangle = \int_0^{\pi/2} C'_{sca}(m\chi,\phi)\mathrm{cos}\phi \mathrm{d}\phi \tag{4.6}$$

4.2.2 T-matrix Method for Multiple Connected and Aligned Spheres

Particles in combustion processes, atmospheric aerosols, and interstellar dust have complicated morphologies. Many of these particles are aggregates of simple spherical particles [135]. The T-matrix method has been developed for non-spherical particles as well as for randomly oriented clusters made of multiple spheres as described in details in Ref. [136]. This approach is based on the superposition principles. The scattered field from the entire cluster is estimated by summing those from each of the spheres [136]. The scattered fields in sphere-centered coordinate are also transformed into cluster-centered coordinates [136]. The cross-sections for randomly oriented cluster can be obtained by using the matrix relationships for the scattered and incident field and integrating the incident field over all propagation and polarization directions [22]. The corresponding scattering matrix can be obtained analytically from operations on the T-matrix [22]. The extinction cross-section of a cluster of connected and aligned spheres is defined as [136],

$$\langle C_{ext}(m\chi)\rangle = \frac{\lambda}{2\pi}\frac{E_{mn}}{E_{kl}}\left(T^0_{mnMklE}T^{0*}_{mnMklE}\right) \tag{4.7}$$

where T^0 denotes the cluster-centered complex T-matrix. The indices m and n are the order and degree of the outgoing wavevector spherical harmonic [135]. In addition, the indices M and E refer to the TM and TE modes, respectively. The notation * corresponds to the complex conjugate. Moreover, k and l are indices related to the number of order and degree in the expansion of the scattered fields [136]. In addition, the scattering cross-section is expressed as [136],

$$\langle C_{sca}(m\chi)\rangle = \frac{\lambda}{2\pi}\mathrm{Re}\left\{T^0_{mnMmnM}\right\} \tag{4.8}$$

Table 4.1: Comparison between the results reported in Ref. [17] and those predicted in this study for the extinction efficiency factor of randomly oriented and infinitely long cylinders with complex index of refraction $m = 2.0 + i0.2$ in vacuum and different size parameters.

Size parameter	Lee [17] Q_{ext}	Present study Q_{ext}	Relative error
$\chi = 3$	1.809	1.7597	1.7 %
$\chi = 6$	1.809	1.7985	0.6 %
$\chi = 12$	1.7267	1.7431	0.9 %

Mackowski and Mishchenko [22] defined the average scattering and absorption cross-sections of a cluster of spheres (in m^2) as

$$\langle C_{sca}(m\chi)\rangle = \pi r_{eq,V}^2 \langle Q_{sca}\rangle \qquad \text{and} \qquad \langle C_{abs}(m\chi)\rangle = \pi r_{eq,V}^2 \langle Q_{abs}\rangle \tag{4.9}$$

where $r_{eq,V} = rN^{1/3}$ is the equivalent radius of a single sphere of volume identical to that of the cluster of N spheres.

4.3 Validation

The computer codes for (i) Lorentz-Mie theory for randomly oriented and infinitely long cylinders and (ii) the T-matrix method for randomly oriented multiple connected and aligned spheres used in this study were obtained from Refs. [22, 137] and were carefully validated, as discussed in this section.

4.3.1 Lorentz-Mie theory for Infinitely Long Cylinders

Lee [17] calculated the extinction efficiency factor Q_{ext} of a randomly oriented and infinitely long cylinder with complex index of refraction $m = 2.0 + i0.2$ in

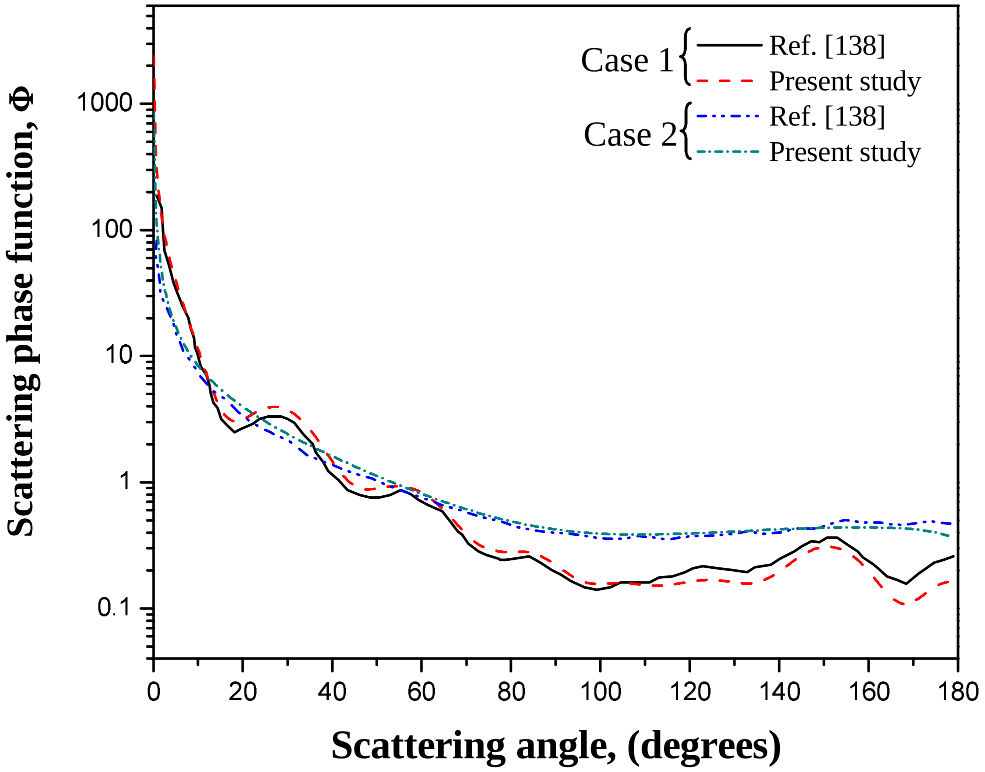

Figure 4.3: Scattering phase function for randomly oriented infinitely long cylinders as a function of the scattering angle for two test cases (1) $m = 1.507 + i0.0$ and $\chi = 6.283$ and (2) $m = 1.05 + i1.08$ and $\chi = 0.684$.

vacuum (n=1) for different size parameters $\chi = 3$, 6, and 12. Table 4.1 compares the extinction efficiency factors between the results reported in Ref. [17] and those predicted in this study for these size parameters. The relative error was less than 2.0% and, overall, good agreement was found.

Moreover, Lee [138] calculated the scattering phase function of a randomly oriented and infinitely long cylinder for two cases (1) the cylinder has complex index of refraction $m = 1.507 + i0.0$ (non-absorbing) and size parameter $\chi = 6.283$ and (2) the cylinder has complex index of refraction $m = 1.05 + i1.08$ (strongly absorbing) and size parameter $\chi = 0.684$. In both cases, the surrounding medium was vacuum. Figure 4.3 shows the scattering phase function for randomly oriented and infinitely long cylinders as a function of the scattering angle reported in Ref. [138] and predicted in this study. Good agreement was found confirming the validity of the computer code implementing the Lorentz-Mie theory for randomly oriented infinitely and long cylinders.

4.3.2 T-matrix for Multiple Connected and Aligned Spheres

Table 4.2: Comparison of the absorption and scattering efficiency factors obtained from the T-matrix code for multiple connected and aligned spheres [22] and from the code for bispheres [23] for two connected spheres with size parameters $\chi = 0.01, 0.1, 1.0$, and 10.0.

	Q_{abs} [22]	Q_{abs} [23]
$\chi = 0.01$	1.002×10^{-4}	1.002×10^{-4}
$\chi = 0.1$	1.002×10^{-3}	1.002×10^{-3}
$\chi = 1.0$	1.012×10^{-2}	1.012×10^{-2}
$\chi = 10.0$	9.877×10^{-2}	9.877×10^{-2}
	Q_{sca} [22]	Q_{sca} [23]
$\chi = 0.01$	8.353×10^{-12}	8.352×10^{-12}
$\chi = 0.1$	8.266×10^{-8}	8.266×10^{-8}
$\chi = 1.0$	3.809×10^{-4}	3.809×10^{-4}
$\chi = 10.0$	7.421×10^{-2}	7.421×10^{-2}

The results obtained from the code for bispheres developed in Ref. [23] were used to validate the T-matrix code for multiple connected and aligned spheres [22]. Mishchenko and Mackowski [23] compared the elements of Stokes scattering matrix for randomly oriented prolate spheroids with an aspect ratio of 2 with those of randomly oriented connected bispheres and calculated the corresponding absorption and scattering efficiency factors. Here, size parameter was defined as $\chi = 2\pi r/\lambda$ where r is the radius of the spheres and χ varied from 0.01 to 10. Table 4.2 compares the absorption and scattering efficiency factors of two connected spheres obtained from our T-matrix code [22] and the results reported in the literature for bispheres [23]. The relative error was very small confirming the validity of the T-matrix code used in this study.

4.4 Results and Discussion

In order to compare the scattering and absorption cross-sections of a randomly oriented clusters of connected and aligned N spheres of radius r with those of a randomly oriented infinitely long cylinders, the cross-sections per unit length (in m) can be defined as

$$\langle C'_{sca}(m\chi)\rangle = \frac{\pi r}{2N^{1/3}}\langle Q_{sca}\rangle \qquad \text{and} \qquad \langle C'_{abs}(m\chi)\rangle = \frac{\pi r}{2N^{1/3}}\langle Q_{abs}\rangle \tag{4.10}$$

Figure 4.4 shows the absorption and scattering cross-sections per unit length of randomly oriented clusters of multiple connected and aligned spheres as functions of the number of spheres. Here, the complex index of refraction of the spheres and of the equivalent cylinder was $m_2 = 1.355 + i0.004$ while that of the surrounding medium was $m_1 = 1.333 + i0.0$. Three size parameters were considered namely $\chi = 0.01, 0.1$, and 1.0. The results were compared with those of a randomly oriented and infinitely long cylinder with the same complex index of refraction and equivalent radius $r_{eq,V} = \sqrt{2/3}r$ such that the volume of the cylinders was identical to that of randomly oriented multiple connected and aligned spheres. In addition, the results were also compared with those of a randomly oriented and infinitely long cylinder with surface-equivalent radius $r_{eq,S} = r$.

Figure 4.4 indicates that the scattering cross-section of multiple spheres increased as the number of spheres increased for all size parameters considered. In addition, as the number of sphere increased, the scattering cross-section asymptotically converged to that of randomly oriented and infinitely long cylinders with

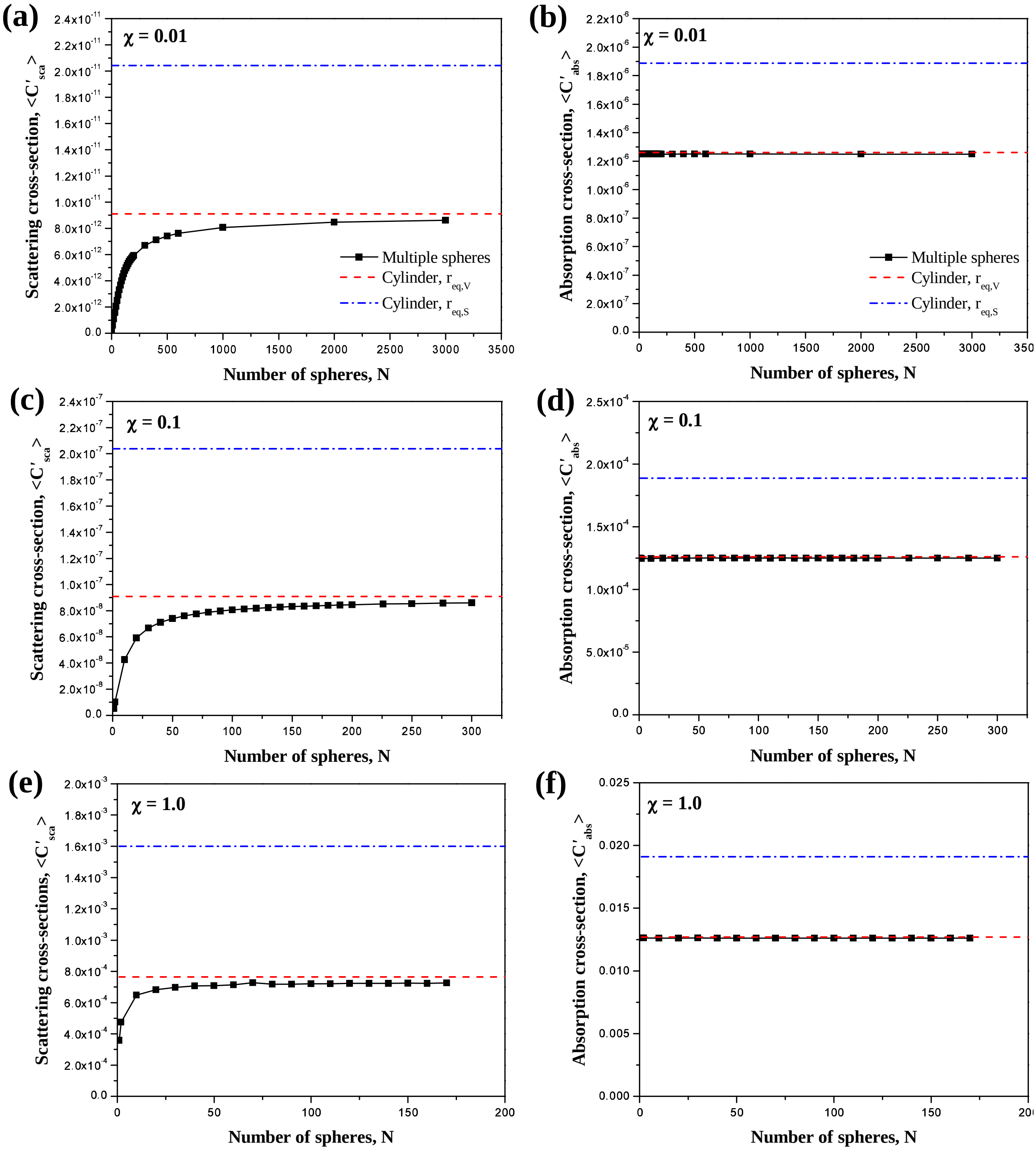

Figure 4.4: Scattering and absorption cross-sections $\langle C'_{sca}\rangle \, and \, \langle C'_{abs}\rangle$ per unit length (in m) for randomly oriented multiple connected and aligned spheres as a function of the number of spheres N and for infinitely long cylinders of volume-equivalent radius for (a, b) $\chi = 0.01$, (c, d) $\chi = 0.1$, and (e, f) $\chi = 1.0$.

volume-equivalent radius. However, the cross-sections of multiple spheres were much smaller than those of the randomly oriented and infinitely long cylinder with surface-equivalent radius.

Moreover, the absorption cross-section of multiple spheres was equal to that of an infinitely long cylinder with volume-equivalent radius regardless of the number of spheres. The relative error between the scattering cross-sections of multiple spheres and those of infinitely long cylinders was less about 4.7, 2.9, and 4.9 % for $N = 3500, 800$, and 170 for $\chi = 0.01, 0.1$, and 1.0, respectively. For size parameters larger than 1.0, twenty or more, connected and aligned spheres can be approximated as infinitely long cylinders. These results establish that the radiation characteristics of randomly oriented clusters of multiple connected and aligned spheres can be approximated as randomly oriented and infinitely long cylinders with volume-equivalent radius. Then, their radiation characteristics can be computed using simpler Lorentz-Mie for infinitely long and randomly oriented cylinders, thus, simplifying significantly the computational effort.

4.5 Conclusions

This chapter presented predictions of the radiation characteristics of multiple connected and aligned spheres. The scattering cross-sections per unit length of randomly oriented clusters of multiple connected and aligned spheres asymptotically converged to those of randomly oriented infinitely long cylinders. The results established that scattering and absorption by randomly oriented clusters of multiple connected and aligned spheres can be approximated as those of randomly oriented and infinitely long cylinders with volume-equivalent radius provided that there is a sufficiently large number of spheres. These results will be useful in retrieving the optical properties of filamentous cyanobacteria based on a method similar to that presented in Chapter 3, for example.

CHAPTER 5

Modeling and Design Guidelines for Outdoor Photobioreactors

5.1 Introduction

Photobiological carbon dioxide (CO_2) fixation and biofuel production have received major academic and industrial interest in recent years due to rising concerns over global warming, fossil fuel cost, as well as energy security. The technology consists of providing CO_2 and sunlight to selected species of microorganisms grown in photobioreactors. These microorganisms, in turn, grow and may produce (i) gases such as methane and hydrogen or (ii) lipids which can be converted to liquid fuels, depending on the species and growth conditions. To achieve economic viability, photobioreactors must be scaling-up and optimized for the mass production of microorganisms.

5.2 Background

5.2.1 Radiation Transfer in Photobioreactors

The radiative transfer equation (RTE) is an energy balance for the radiation intensity $I_\lambda(\mathbf{r}, \hat{\mathbf{s}})$ at location $\mathbf{r}$ traveling along direction $\hat{\mathbf{s}}$. In absorbing, scattering, but non-emitting PBRs, the RTE is expressed as [42]

$$\hat{\mathbf{s}} \cdot \nabla I_\lambda(\mathbf{r}, \hat{\mathbf{s}}) = -\kappa_\lambda(\mathbf{r}) I_\lambda(\mathbf{r}, \hat{\mathbf{s}}) - \sigma_{s,\lambda}(\mathbf{r}) I_\lambda(\mathbf{r}, \hat{\mathbf{s}}) + \frac{\sigma_{s,\lambda}(\mathbf{r})}{4\pi} \int_{4\pi} I_\lambda(\mathbf{r}, \hat{\mathbf{s}}) \Phi_{T,\lambda}(\hat{\mathbf{s}}_i, \hat{\mathbf{s}}) d\Omega_i \tag{5.1}$$

where the effective absorption and scattering coefficients of the suspension are denoted by κ_λ and $\sigma_{s,\lambda}$ (in m^{-1}), respectively. The effective scattering phase function of the suspension is denoted by $\Phi_{T,\lambda}(\hat{\mathbf{s}}_i, \hat{\mathbf{s}})$. It represents the probability that radiation traveling in the solid angle $d\Omega_i$ around direction $\hat{\mathbf{s}}_i$ will be scattered into the solid angle $d\Omega$ around direction $\hat{\mathbf{s}}$.

The local spectral fluence rate, denoted by $G_\lambda(\mathbf{r})$, and the local fluence rate average over the PAR region between 400 and 700 nm, denoted by $G_{PAR}(\mathbf{r})$, available to microalgae at location $\mathbf{r}$ are respectively defined as [42],

$$G_\lambda(\mathbf{r}) = \int\limits_{4\pi} I_\lambda(\mathbf{r}, \hat{\mathbf{s}}) \mathrm{d}\Omega \quad \text{and} \quad G_{PAR}(\mathbf{r}) = \int_{400}^{700} G_\lambda(\mathbf{r}) \mathrm{d}\lambda \tag{5.2}$$

The average fluence rate G_{av} over the entire PBR of volume V can be estimated from the local PAR-averaged fluence rate $G_{PAR}(\mathbf{r})$ as,

$$G_{av} = \frac{1}{V} \int\limits_V G_{PAR}(\mathbf{r})\, dV = \frac{1}{V} \int\limits_V \left(\int_{400}^{700} G_\lambda(\mathbf{r})\, d\lambda \right) dV \tag{5.3}$$

5.2.2 Method of solution of the RTE

Various solution methods have been developed to solve the RTE in photobioreactors including (i) Beer-Lambert's law [139, 140], (ii) the Schuster-Schwarzschild two-flux approximation [113, 114, 141], (iii) finite volume method combined with discrete ordinate method (DOM) [123, 142], and (iv) Monte Carlo method [143, 144].

The two-flux approximation assumes one-dimensional radiation transfer and can account for in-scattering terms as well as anisotropic scattering [42] and provides a simple analytical expression for the local spectral fluence rate $G_\lambda(z)$

[113, 114]. In cases when the PBR is exposed to both collimated and diffuse irradiances $G_{in,c,\lambda}$ and $G_{in,d,\lambda}$, the total local spectral fluence rate $G_\lambda(z)$ (in W/m^2) can be estimated by summing its collimated and diffuse components as [145],

$$G_\lambda(z) = G_{c,\lambda}(z) + G_{d,\lambda}(z) \tag{5.4}$$

Pottier *et al.* [39] solved the radiative transfer equation (RTE) using the two-flux approximation to model light transfer in a one-dimensional flat-plate photobioreactor with a transparent front window and a diffusely reflecting back side with spectral reflectance ρ_λ. The authors derived an analytical expression for the local spectral fluence rate $G_{c,\lambda}(z)$ (in W/m^2) in such PBRs exposed to solar irradiance $G_{in,c,\lambda}$ incident onto the photobioreactor at an angle θ_c with respect to the surface's normal direction as [39],

$$\frac{G_{c,\lambda}(z)}{G_{in,c,\lambda}} = 2\sec\theta_c \frac{[\rho_\lambda(1+\alpha_\lambda)e^{-\delta_\lambda L} - (1-\alpha_\lambda)e^{-\delta_\lambda L}]e^{\delta_\lambda z} + [(1+\alpha_\lambda)e^{\delta_\lambda L} - \rho_\lambda(1-\alpha_\lambda)e^{\delta_\lambda L}]e^{-\delta_\lambda z}}{(1+\alpha_\lambda)^2 e^{\delta_\lambda L} - (1-\alpha_\lambda)^2 e^{-\delta_\lambda L} - \rho_\lambda(1-\alpha_\lambda^2)e^{\delta_\lambda L} + \rho_\lambda(1-\alpha_\lambda^2)e^{-\delta_\lambda L}} \tag{5.5}$$

where the parameters α_λ and δ_λ are expressed as [39],

$$\alpha_\lambda = \sqrt{\frac{\bar{A}_{abs,\lambda}}{\bar{A}_{abs,\lambda} + 2b_\lambda \bar{S}_{sca,\lambda}}} \quad \text{and} \quad \delta_\lambda = X\sec\theta_c \sqrt{\bar{A}_{abs,\lambda}(\bar{A}_{abs,\lambda} + 2b_\lambda \bar{S}_{sca,\lambda})} \tag{5.6}$$

Here, $\bar{A}_{abs,\lambda}$ and $\bar{S}_{sca,\lambda}$ are the average mass absorption and scattering cross-sections (in m^2/kg) while X is the microorganism mass concentration X expressed in kg dry cell weight cells per m^3 of suspension (or kg/m^3). They are such that [3],

$$\kappa_\lambda = \bar{A}_{abs,\lambda} X \quad \text{and} \quad \sigma_{s,\lambda} = \bar{S}_{sca,\lambda} X \tag{5.7}$$

The backward scattering fraction, denoted by b_λ, is defined as [39],

$$b_\lambda = \int_{\pi/2}^{\pi} \Phi_{T,\lambda}(\theta)\sin\theta \mathrm{d}\theta \tag{5.8}$$

The local diffuse spectral fluence rate $G_{d,\lambda}(z)$ can be estimated from Equations (5.5) and (5.6) by replacing $\sec\theta_c$ by a factor 2.

Numerical methods such as finite volume method with DOM [142] and Monte Carlo method [144] can be used to solve multidimensional RTE in PBRs with more complex geometries. In the present study, the discontinuous Galerkin (DG) method will be used to solve the 3D RTE in different PBRs. This method was first used by Reed and Hill [66] to solve the neutron transport equation. It has recently been used for solving the radiative transfer equation [68,73,146]. A major feature of the DG method is that the constraint of the field variable continuity across the inter-element boundaries in a computational domain is not enforced [73] unlike in conventional Galerkin method. Thus, the DG method allows for a wide range of interpolation functions for the solution of many problems, particularly if the solution has sharp discontinuity in the variable field [68]. Lagrange polynomial is generally used as the interpolation function in the local finite elements [147]. The n^{th} order of Lagrange polynomial represents the order of DG method referred to as P_n. A high order accuracy can be achieved by increasing the order of the DG method [71]. The advantage of the DG method is that (1) it is elementwise conservative and stable [68], (2) it can use high order accuracy and polynomials of arbitrary order with a local mesh adaptive algorithm [68], (3) the method can be applied to structured and unstructured meshes [71]. To accelerate the computation, the DG method can conveniently be implemented on Graphics Processing Units (GPU) instead of CPU [146].

5.2.3 Microalgae Growth Kinetics

The time rate of change of microalgae mass concentration X can be modeled as [148],

$$\frac{dX}{dt} = \bar{\mu}X \tag{5.9}$$

where $\bar{\mu}$ is the average total specific growth rate expressed in hr^{-1}. Various growth kinetics models have been developed to predict the local specific growth rate μ. Fouchard *et al.* [18] expressed the photosynthetic growth rate for *C. reinhardtii* as a function of local fluence rate $G_{PAR}(\mathbf{r})$ at location $\mathbf{r}$, accounting for light limitation and inhibition as

$$\mu_p(\mathbf{r}) = \mu_0 \left(\frac{G_{PAR}(\mathbf{r})}{K_S + G_{PAR}(\mathbf{r}) + G_{PAR}^2(\mathbf{r})/K_I} \right) \tag{5.10}$$

where μ_0 is the so-called maximum specific growth rate while the coefficients K_S and K_I are the light half-saturation and inhibition constants, respectively. The authors also considered reduction in growth rate due to cellular respiration as the catabolic process. Then, the local total specific grow rate $\mu(\mathbf{r})$ can be expressed as [18]

$$\mu(\mathbf{r}) = \mu_p(\mathbf{r}) - \mu_s \tag{5.11}$$

where μ_s is the respiration rate and was assumed to be constant at all times and locations [18]. In addition, the average total specific growth rate $\bar{\mu}$ over the PBR volume can be estimated as [18]

$$\bar{\mu} = \frac{1}{V} \int\limits_V \mu(\mathbf{r}) dV \tag{5.12}$$

Alternatively, Grima *et al.* [149] used the Monod model in terms of the average fluence rate G_{av} [Equation (5.3)] accounting for light limitation to estimate μ_p for marine microalgae *Isochrysis galbana.* The authors also consider a constant respiration rate. In addition, Barbosa *et al.* [150] expressed the Monod model as a function of the average fluence rate G_{av} to account for light limitation for green algae *Dunaliella tertiolecta.* The photosynthetic growth rate as a function of average fluence rate G_{av} accounting for light limitation and inhibition was expressed as [151]

$$\mu_p(G_{av}) = \mu_0 \left(\frac{G_{av}}{K_S + G_{av} + G_{av}^2/K_I} \right) \tag{5.13}$$

Here also, cellular respiration can be accounted for by defining the average total specific growth rate as

$$\bar{\mu}' = \mu_p(G_{av}) - \mu_s \tag{5.14}$$

Note that $\bar{\mu}'$ can differ significantly from $\bar{\mu}$ for large microalgae concentrations as discussed later.

5.2.4 Photobioreactor Modeling

Modeling of PBR typically consists of solving the RTE coupled with a growth kinetics model. Aiba [143] calculated the light intensity distribution and absorptance in one-dimensional flat-plate photobioreactor with microalgae *Rhodopseudomonas spheroides* using Monte Carlo method. The author considered anisotropic scattering and neglected reflection at the walls. He compared the absorptance obtained by the Monte Carlo method with that obtained by Beer-Lambert's law as a function of cell concentration. Beer-Lambert's law was found to overestimate the absorptance in the photobioreactor because it does not consider in-scattering [143]. This was also established in Ref. [16].

Cornet *et al.* [113] calculated the local fluence rate as a function of dimensionless thickness within one-dimensional flat-plate photobioreactor with cyanobacterium *Spirulina platensis* using the two-flux approximation. The authors also coupled light transfer and Monod growth kinetics model to estimate the biomass volumetric production rate. They introduced the concept of working illuminated volume which, combined with their models, can be used to retrieve the growth kinetic parameters. Moreover, Cornet and Albiol [152] calculated the local fluence rate in a one-dimensional flat-plate PBR using the two-flux approximation. The authors predicted the temporal evolution of biomass concentration of photoheterotrophic bacteria *Rhodospirillum rubrum* using the Monod model. They also experimentally measured the biomass concentrations in a rectangular PBR as a function of time for different carbon sources and incident collimated irradiances. Good agreement was observed between experimental measurements and model predictions.

Fouchard *et al.* [18] cultivated *C. reinhardtii* in a torus photobioreactor with continuous injection of N_2 and CO_2 gases and white light provided by fluorescent tubes. The authors calculated the light intensity inside the torus photobioreactor using the two-flux approximation [39]. They retrieved the parameters of the kinetics model considering biomass concentration, extracellular sulfur concentration, and intracellular quota. They also examined the model behavior and sensitivity to different model parameters. Cornet and Dussap [153] experimentally measured the temporal evolution of the biomass concentration of *Arthrospira* (*Spirulina*) *platensis* in various photobioreactors. The authors calculated the fluence rate using the two-flux approximation [39] and employed the Monod model [Equation (5.10)] to predicted the biomass concentration as a function of time. The predicted and experimentally measured biomass concentrations fell within 15% of each other for different shape and volume of photobioreactors and incident irradiance.

Wheaton and Krishnamoorthy [142] simulated light transfer coupled with fluid hydrodynamics within an air-lift tubular photobioreactor illuminated from inside by fluorescent lamps. The authors identified the effects of angular discretization, scattering phase function, air mass flow rate, and bubble size on the local fluence rate. They used finite volume method to solve the 3D RTE based on spectrally averaged incident radiation and radiation characteristics of cyanobacterium *Synechococcus sp.* over three spectral bands in the PAR region. They concluded that scattering by bubbles resulted in redistribution of the light but was negligible at high microalgae concentrations, as previously reported [123].

Murphy and Berberoğlu [154] coupled light transfer with photosynthetic rate model for *C. reinhardtii* wild strain and transformant *tla1* within plane parallel

PBR considering photoinhibition. The authors solved the one-dimensional RTE using the discrete ordinates method with Gaussian quadrature to estimate the local fluence rate. They calculated the local specific and total oxygen production as function of optical thickness for different incident irradiances.

Slegers *et al.* [21] simulated outdoor vertical flat-plate PBRs operated in a continuous manner and containing *Phaeodactylum tricornutum* or *Thalassiosira pseudonana*. The authors coupled light transfer with growth kinetics model to estimate volumetric daily and yearly biomass productivity. They used Beer-Lambert's law to calculate the fluence rate within the PBR and a growth kinetic model based on pI-curves and accounting for respiration [155]. Here, the average total specific growth rate was taken as $\bar{\mu}$ [Equation (5.12)]. They investigated the effect of thickness of PBRs and biomass concentration on the volumetric productivity in the Netherlands.

Huang *et al.* [156] simulated annular PBR with *Porphyridium cruentum* operated in a continuous or batch culture. The authors integrated hydrodynamics, radiation transfer, and growth kinetics models to predict biomass concentration as a function of time. The 3D RTE was solved using finite volume method and discrete ordinate method to estimate the light intensity within the annular PBR. The box model with two boxes was used to account for spectral radiation in normal diffuse incident irradiance and radiation characteristics of microalgae to estimate the light intensity within the annular PBR. Good agreement was observed between the numerically prediction of biomass concentration and experimental data reported in the literatures [157].

Finally, Pruvost *et al.* [145] simulated outdoor rectangular PBR exposed to solar irradiance with cyanobacterium *Arthrospira platensis* operated in continuous culture. The authors coupled light transfer with growth kinetics model to estimate areal biomass productivity per unit illuminated surface area. They calculated the fluence rate using the two-flux approximation and biomass concentration for whole-year running. They also identified the effects of the location of PBR and inclination of PBR surface on the maximum areal biomass productivity. The location close to equator had larger biomass productivity than other higher latitude location. In addition, the areal biomass productivity with solar tracking system was larger the that with fixed inclination system.

Previous studies often used spectrally averaged incident irradiance and radiation characteristics [113, 143]. In addition, light transfer in PBRs has frequently been treated as one-dimensional [39, 113, 153] and estimated using either Beer-Lambert's law [21] or the two-flux approximation [113, 114, 141]. Most studies also considered constant and normally collimated incident irradiance [39,153,158]. However, solar irradiance fluctuates in direction and intensity during the day. Also, radiation characteristics of microalgae depend strongly on wavelength. In addition, actual PBRs may have complex geometries for which simplified radiation model may not be valid. In this study, light transfer was accurately simulated by solving the three-dimensional RTE on a spectral basis using experimentally measured spectral radiation characteristics [3]. Both spectral diffuse and collimated solar irradiances with different incident angle corresponding to different times of the day were considered. It was coupled with the Monod growth kinetics model accounting for photolimitation, photoinhibition, and cellular respiration. The fluence rate, biomass concentration, and daily productivity of open ponds, vertical flat-plate, and tubular PBRs were compared and discussed.

5.3 Analysis

5.3.1 Problem Statement

Algal biomass production in photobioreactors depends on numerous parameters including (i) the cultivation location, (ii) the day of the year and the time of the day along with (iii) the corresponding solar irradiance, (iv) the microalgae

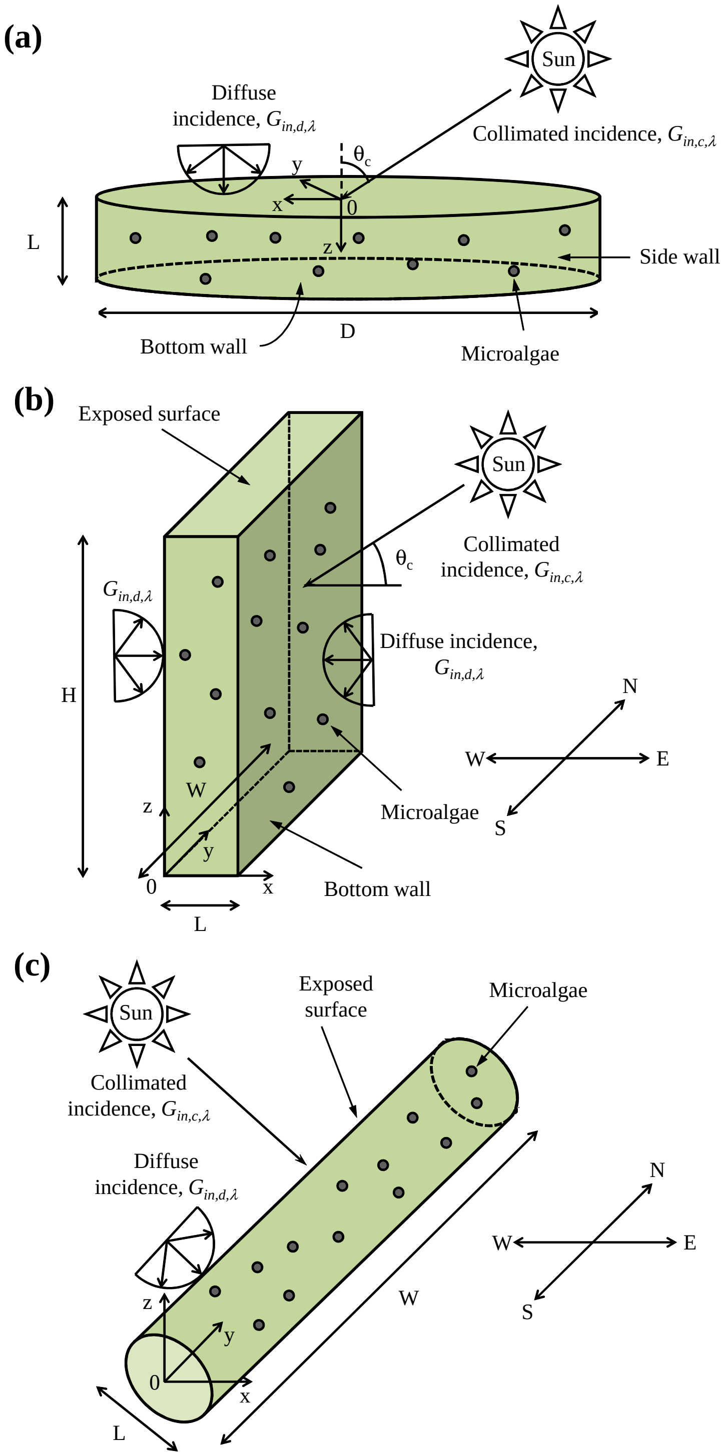

Figure 5.1: Schematic of the (a) open pond, (b) vertical flat-plate, and (c) tubular photobioreactors simulated in this study along with coordinate systems.

species, (v) the initial mass concentration, (vi) the photobioreactor geometry, and (vii) its wall reflection and refraction. The present study simulates light transfer and microalgae growth in photobioreactors located in Los Angeles, CA USA (34.04°N, 118.15°W). Simulations were performed for open pond, vertical flat-plate, and tubular photobioreactors. The photobioreactors were aligned along the north-south direction and exposed to solar irradiance comprised of both a collimated and a diffuse component. Figure 5.1 shows the geometries, dimensions, and boundary conditions of the PBRs simulated in this study along with the associated coordinate systems. The open pond had depth L varying from 0.05 to 1.0 m. The thickness L of the vertical flat-plate PBR ranged from 0.05 to 1.0 m while the diameter L of the tubular PBR varied from 0.1 to 1.0 m. *C. reinhardtii* were simulated for illustration purposes and because its growth kinetic parameters were known [18].

5.3.2 Assumptions

In order to predict light transfer and the temporal evolution of microalgae concentration in the different photobioreactors considered, it was assumed that: (1) the microalgae were well mixed, randomly oriented, and uniformly distributed in the photobioreactor. In practice, this is achieved by stirring the PBR with paddle wheels or gas sparging, for example. (2) The liquid medium was non-emitting (cold) and non-scattering over the PAR region. (3) The absorption coefficient of the medium was the same as that of water. (4) The photobioreactor was neither mass transfer nor nutrient limited and operated at constant temperature. (5) The radiation characteristics of *C. reinhardtii* remained the same throughout the day. (6) The photosynthetic specific growth rate μ_p was only a function of the local and average fluence rate available in the PBRs and given by Equations (5.10) or (5.13). (7) Bubbles potentially used for stirring purposes featured interfacial area concentration smaller than 450 m^{-1} so their effect on light transfer could be neglected [123].

5.3.3 Governing Equations

The radiation intensity $I_\lambda(\mathbf{r}, \hat{\mathbf{s}})$ in direction $\hat{\mathbf{s}}$ at location $\mathbf{r}$ can be decomposed as the sum of a collimated $I_{c,\lambda}(\mathbf{r}, \hat{\mathbf{s}})$ and a diffuse $I_{d,\lambda}(\mathbf{r}, \hat{\mathbf{s}})$ component so that [42],

$$I_\lambda(\mathbf{r}, \hat{\mathbf{s}}) = I_{c,\lambda}(\mathbf{r}, \hat{\mathbf{s}}) + I_{d,\lambda}(\mathbf{r}, \hat{\mathbf{s}}) \tag{5.15}$$

The steady-state RTE for the collimated intensity can be written as [42],

$$\hat{\mathbf{s}} \cdot \nabla I_{c,\lambda}(\mathbf{r}, \hat{\mathbf{s}}) = -\kappa_\lambda I_{c,\lambda}(\mathbf{r}, \hat{\mathbf{s}}) - \sigma_{s,\lambda} I_{c,\lambda}(\mathbf{r}, \hat{\mathbf{s}}) \tag{5.16}$$

Similarly, the steady-state RTE for the diffuse intensity $I_{d,\lambda}(\hat{r}, \hat{s})$ can be written as [42],

$$\begin{aligned}\hat{\mathbf{s}} \cdot \nabla I_{d,\lambda}(\mathbf{r}, \hat{\mathbf{s}}) &= -\kappa_\lambda I_{d,\lambda}(\mathbf{r}, \hat{\mathbf{s}}) - \sigma_{s,\lambda} I_{d,\lambda}(\mathbf{r}, \hat{\mathbf{s}}) + \frac{\sigma_{s,\lambda}}{4\pi} \int\limits_{4\pi} I_{d,\lambda}(\mathbf{r}, \hat{\mathbf{s}}_i) \Phi_\lambda(\hat{\mathbf{s}}_i, \hat{\mathbf{s}}) d\Omega_i \\ &\quad + \frac{\sigma_{s,\lambda}}{4\pi} \int\limits_{4\pi} I_{c,\lambda}(\mathbf{r}, \hat{\mathbf{s}}_i) \Phi_\lambda(\hat{\mathbf{s}}_i, \hat{\mathbf{s}}) d\Omega_i\end{aligned} \tag{5.17}$$

5.3.4 Radiation Characteristics of *C. reinhardtii*

The effective absorption coefficient κ_λ of the suspension can be expressed in terms of the microorganism mass concentration X as [159],

$$\kappa_\lambda = \kappa_{L,\lambda}(1 - \nu X) + \bar{A}_{abs,\lambda} X \tag{5.18}$$

where ν is the specific volume of microorganisms assumed to be equal to 0.001 m^3/kg. The absorption coefficient of the liquid phase $\kappa_{L,\lambda}$ is expressed in m^{-1} and given by [42],

$$\kappa_{L,\lambda} = \frac{4\pi k_\lambda}{\lambda} \tag{5.19}$$

where k_λ was taken as the absorption index of water reported by Hale and Querry [132]. On the other hand, the effective scattering coefficient $\sigma_{s,\lambda}$ of the suspension can be expressed as [43],

$$\sigma_{s,\lambda} = \bar{S}_{sca,\lambda} X \tag{5.20}$$

The average mass absorption and scattering cross-sections $\bar{A}_{abs,\lambda}$ and $\bar{S}_{sca,\lambda}$ along with the Henyey-Greenstein asymmetry factor of *C. reinhardtii* between 400 and 750 nm were reported in the literature [3]. Alternatively, they could have been predicted by Lorentz-Mie theory using the complex index of refraction retrieved by Lee *et al.* [160].

5.3.5 Boundary and Initial Conditions

The solar spectrum incident on Earth depends on the latitude, longitude, and altitude. In this study, the Simple Model of the Atmospheric Radiative Transfer of Sunshine (SMARTS) [161] was used to predict the incident collimated and diffuse solar irradiances at sea level in Los Angeles, CA on June 21 at different times of the day. Figure 5.2a shows the daily path of the sun on June 21 in Los Angeles. Figure 5.2b shows examples of the incident collimated and diffuse solar irradiances, denoted by $G_{in,c,\lambda}$ and $G_{in,d,\lambda}$, in the PAR at noon. These irradiances were used in the boundary conditions necessary to solve Equations (5.16) and (5.17) according to $I_{c,\lambda}(\mathbf{r}_{wall}, \hat{\mathbf{s}}) = G_{in,c,\lambda}$ and $I_{d,\lambda}(\mathbf{r}_{wall}, \hat{\mathbf{s}}) = G_{in,d,\lambda}/2\pi$.

The other boundary conditions depend on the PBR geometry. The open pond was assumed to have transparent top surface and black ($\rho_\lambda = 0$) or diffusely reflecting ($\rho_\lambda = 1$) bottom and side walls. The panels of the vertical flat-plate PBR simulated were assumed to be transparent with a constant index of refraction of 1.49 over the PAR. The tubular PBR was assumed to be transparent and refraction by the tube wall was ignored.

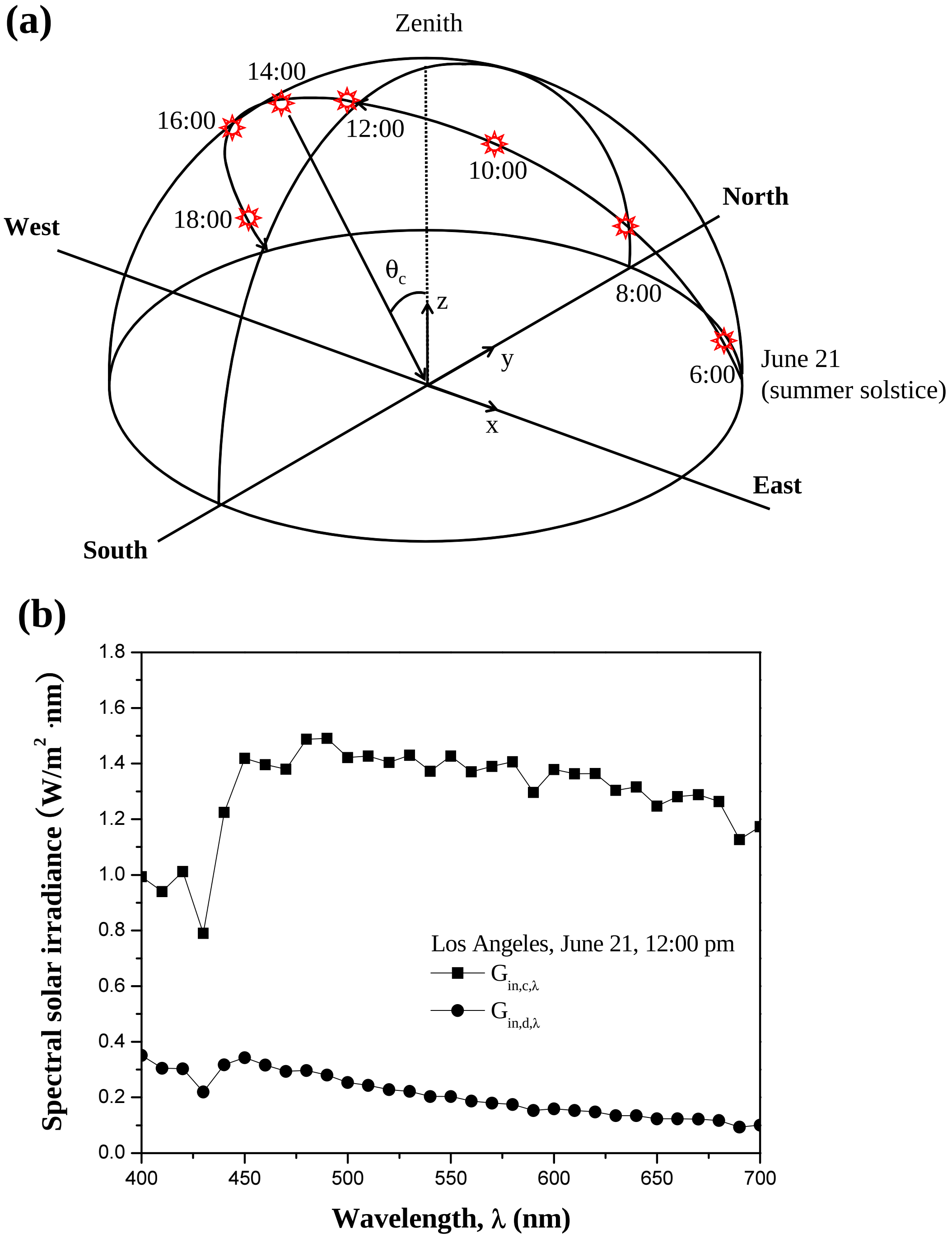

Figure 5.2: (a) Schematic of the daily solar trajectory in the Los Angeles sky on June 21 and (b) collimated $G_{in,c,\lambda}$ and diffuse $G_{in,d,\lambda}$ solar irradiance spectrum over the PAR at 12:00 pm.

5.3.6 Two-Flux Approximation

The analytical expression derived by Cornet *et al.* [113] for predicting the local fluence rate G_λ(z) in vertical flat-plate PBRs exposed to collimated solar irradiance with reflecting back wall [Equation (5.5)] can be extended to vertical flat-plate PBRs with transparent faces, one exposed to direct collimated and diffuse incident solar irradiance $G_{in,c,\lambda}$ and $G_{in,d,\lambda}$ and the other exposed only to diffuse solar irradiance $G_{in,d,\lambda}$. Then, the local spectral fluence rate at time t can be expressed as

$$G_\lambda(z,t) = G_{in,c,\lambda}(t) f_c(z) + G_{in,d,\lambda}(t) f_d(z) + G_{in,d,\lambda}(t) f_d(L-z) \tag{5.21}$$

where $f_c(z)$ is defined as

$$f_c(z) = 2 \sec\theta_c(t) \frac{(1+\alpha_\lambda)e^{\delta_\lambda L}e^{-\delta_\lambda z} - (1-\alpha_\lambda)e^{-\delta_\lambda L}e^{\delta_\lambda z}}{(1+\alpha_\lambda)^2 e^{\delta_\lambda L} - (1-\alpha_\lambda)^2 e^{-\delta_\lambda L}} \tag{5.22}$$

and $f_d(z)$ is expressed as

$$f_d(z) = 4 \frac{(1+\alpha_\lambda)e^{\delta_{d,\lambda} L}e^{-\delta_{d,\lambda} z} - (1-\alpha_\lambda)e^{-\delta_{d,\lambda} L}e^{\delta_{d,\lambda} z}}{(1+\alpha_\lambda)^2 e^{\delta_{d,\lambda} L} - (1-\alpha_\lambda)^2 e^{-\delta_{d,\lambda} L}} \tag{5.23}$$

Here, α_λ and δ_λ are given by Equation (5.6) while $\delta_{d,\lambda} = 2X\sqrt{\bar{A}_{abs,\lambda}(\bar{A}_{abs,\lambda} + 2b_\lambda \bar{S}_{sca,\lambda})}$.

Moreover, Berberoğlu *et al.* [3] reported that the Henyey-Greenstein asymmetry factor of *C. reinhardtii* was 0.98 corresponding to strongly forward scattering, typical of microalgae. Then, the backward scattering fraction b_λ given by Equation (5.8) can be assumed to be zero and $\alpha_\lambda \approx 1$. Then, the fluence rate in vertical flat-plate PBR exposed to collimated and diffuse incident radiation simplifies to

$$G_\lambda(z,t) = \sec\theta_c(t) G_{in,c,\lambda}(t) e^{-\delta_\lambda z} + 2G_{in,d,\lambda}(t) e^{-\delta_{d,\lambda} z} + 2G_{in,d,\lambda}(t) e^{-\delta_{d,\lambda}(L-z)} \tag{5.24}$$

where δ_λ and $\delta_{d,\lambda}$ simplify to $\delta_\lambda = \bar{A}_{abs,\lambda} X(t) \text{sec}\theta_c(t)$ and $\delta_{d,\lambda} = 2\bar{A}_{abs,\lambda} X(t)$. Similarly, the fluence rate in open ponds with reflecting back wall can be expressed as

$$G_\lambda(z,t) = G_{in,c,\lambda}(t) f_c(z) + G_{in,d,\lambda}(t) f_d(z) \tag{5.25}$$

If $\alpha_\lambda \approx 1$, the two-flux approximation for open-ponds simplifies to

$$G_\lambda(z,t) = G_{in,c,\lambda}(t)\sec\theta_c(t)\left[e^{-\delta_\lambda z} + \rho_\lambda e^{-\delta_\lambda(2L-z)}\right] + 2G_{in,d,\lambda}(t)\left[e^{-\delta_{d,\lambda} z} + \rho_\lambda e^{-\delta_{d,\lambda}(2L-z)}\right] \tag{5.26}$$

These expressions apply also in the case of open ponds with black walls with $\rho_\lambda = 0$.

5.3.7 Method of solution

5.3.7.1 Discontinuous Galerkin (DG) method

The 3D RTE given by Equations (5.16) and (5.17) were solved numerically for $I_\lambda(\mathbf{r}, \hat{\mathbf{s}})$ using the discontinuous Galerkin method.

Sunlight incident on the PBRs consists of a collimated and a diffuse component. The direction $\theta_c(t)$ of collimated incidence changed during the course of the day. Unfortunately, conventional angular discretization methods such as discrete ordinate S_N [162] and T_N [163] approximations typically use fixed discrete directions. Therefore, the discretization would need to be changed for simulating different hours of the day [164]. Discrete ordinate scheme with infinitely small weight (DOS+ISW) has been proposed as a way to solve problems involving collimated radiation [164]. It consists of adding a discrete direction, corresponding to the direction of collimated irradiance, directly to a conventional discrete ordinate quadrature. The weight associated with this new discrete direction is set to be infinitely small [164]. Thus, the new discrete direction has no effect on the zeroth, first, and second order moments of the intensity [164]. This method was employed in this study to simulate the collimated part of sunlight incident on the PBRs during the course of the day. Finally, unstructured tetrahedral elements were employed for spatial discretization. The number of elements varied depending on the size of PBRs. The maximum number of elements in simulating open ponds, vertical flat-plate, and tubular photobioreactors was 95633, 91257, and 112464, respectively. The S_4 angular discretization, consisting of 6 discrete ordinate directions per quadrant, was used. The PAR region, defined from 400 to 700 nm, was discretized in 10 nm increments for a total of 31 wavelengths. To obtain a numerically converged solution of the RTE, the order of the DG method was increased incrementally from P-1 to P-4 until the difference in the average total specific growth rate between two consecutive refinements fell below 2%. This criterion was met between P-3 and P-4. Thus, P-3 order was used in all simulations.

5.3.7.2 Growth kinetics

In the present study, the growth kinetics model described by Equations (5.9) to (5.12) was used to determine the temporal evolution of microalgae concentration in photobioreactors. Fouchard *et al.* [18] measured the average specific growth rate $\bar{\mu}$ of the green algae *C. reinhardtii*. The authors estimated the parameters μ_0, μ_s, K_S, and K_I to be 0.2274 hr^{-1}, 0.032 hr^{-1}, 81.38 μmol photon m$^{-2}\cdot$ s^{-1}, and 2500 μmol photon m$^{-2}\cdot$ s^{-1}, respectively for local irradiance $G_{PAR}(\mathbf{r})$ ranging from 0 to 400 μmol photon m$^{-2}\cdot$ s^{-1} [18]. Figure 5.3 shows the average total specific growth rate $\bar{\mu}$ of *C. reinhardtii* measured experimentally [18,19] and that predicted by Equations (5.10) to (5.12) using the above parameters. The same parameters were used in the present study. Here, K_S and K_I, expressed in μmol photon m$^{-2}\cdot$ s^{-1}, were converted in W/m^2 using the conversion factor, 1 μmol photon m$^{-2}\cdot$ s^{-1} $\simeq$ 0.2174 W/m^2 over the PAR region [165].

5.3.7.3 Solution Procedure

The mass concentration of microalgae as a function of time was obtained by the following procedure. First, the initial mass concentration of microalgae was set as $X(t = 0) = X_0$ at initial time 8:00 am. The corresponding effective absorption

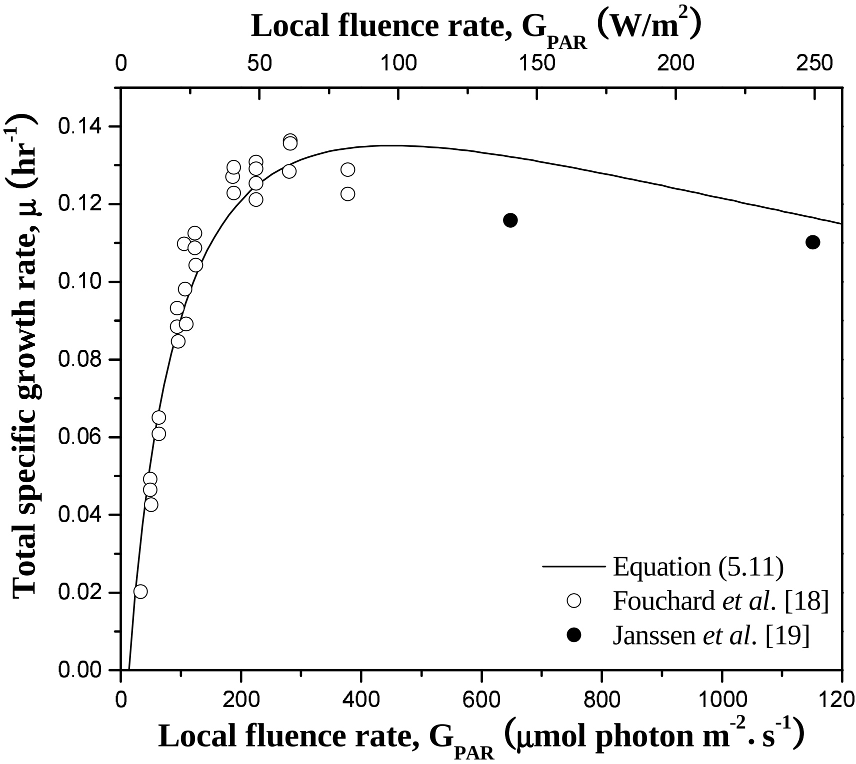

Figure 5.3: Total specific growth rate μ of *C. reinhardtii* as function of the local fluence rate $G_{PAR}(\mathbf{r})$ measured experimentally [18,19] and predicted by Equations (5.10) and (5.11) with parameters $\mu_0 = 0.2274$ hr^{-1}, $\mu_s = 0.032$ hr^{-1}, $K_S = 81.38$ μmol photon m$^{-2}\cdot$ s^{-1}, and $K_I = 2500$ μmol photon m$^{-2}\cdot$ s^{-1}.

coefficient κ_λ and the scattering coefficient $\sigma_{s,\lambda}$ were estimated using Equations (5.18) and (5.20), respectively. Then, Equations (5.16) and (5.17) were solved for $I_{\lambda,c}$ and for $I_{\lambda,d}$ using the DG method. Then, the local fluence rate was estimated using Equation (5.2). The corresponding local photosynthetic specific growth rate μ_p was estimated [Equation (5.10)] and used to calculate the average total specific growth rate $\bar{\mu}$ [Equation (5.12)] and the microalgae mass concentration $X(t)$ [Equation (5.9)] at subsequent time. This procedure was repeated by increment of 2 hours. During that time interval, the local fluence rate and average total specific growth rate were assumed to be constant. To assess the validity of this assumption, the temporal evolution of the concentration in open ponds was predicted for 12 hours with initial mass concentration $X_0 = 0.1$ kg/m^3 using the two-flux approximation and the same growth kinetics model. The local fluence rates obtained for time intervals of 30 minutes, 1 hour, and 2 hours were compared at 8:00 am, 10:00 am, 12:00 pm (noon), 2:00 pm, 4:00 pm, 6:00 pm, and 8:00 pm. The maximum relative errors in $\bar{\mu}(t)$ and $X(t)$ throughout the day were less than 3% and 2%, respectively. Thus, a 2 hours time increment was judged appropriate for simulating coupled radiation transfer and microalgae growth kinetics in the PBR throughout the day.

5.4 Results and Discussion

Simulations were performed for commonly used photobioreactors including (i) open ponds, (ii) vertical flat-plate, and (iii) tubular PBRs exposed to collimated and diffuse solar irradiances and containing *C. reinhardtii* with initial concentration X_0. The local fluence rate was computed as a function of time and the validity of the two-flux approximation for open pond and flat-plate PBRs was assessed. In addition, the effects of respiration on the microalgae growth were evaluated. Finally, the daily biomass productivities of the different PBRs considered were compared.

5.4.1 Open ponds

5.4.1.1 Fluence rate

Figure 5.4 shows the local PAR-averaged fluence rate $G_{PAR}(\mathbf{r})$ in the east/west center plane of the open pond with either (a) black or (b) reflecting side and bottom walls at times 8:00 am, 10:00 am, 12:00 pm (noon), 2:00 pm, and 4:00 pm. Here, the pond diameter D, depth L, and initial mass concentration X_0 were taken as 2 m, 0.1 m, and 0.1 kg/m^3, respectively. By comparing Figures 5.4a and 5.4b, it is evident that the reflecting walls increased the local fluence rate in the PBR, particularly before 4:00 pm. However, the relative difference, in terms of mass concentration $X(t)$, between open ponds with black and reflecting walls was less than 1% after a day of growth. In both cases, the local fluence rate was nearly one-dimensional except near the side walls where shadows were apparent in the early morning and late afternoon. Note that even though, on June 21 in Los Angeles, the sun rises at 05:42 am and sets at 8:08 pm, the average total specific growth rate $\bar{\mu}$ at times earlier than 8:00 am and later than 8:00 pm was less than 0.01 hr^{-1} and growth was negligible.

Moreover, Figure 5.5 compares the local fluence rate $G_{PAR}(z)$ at the centerline of the open pond with black walls (top) and reflecting walls (bottom) at times 8:00 am, 12:00 pm (noon), and 4:00 pm. It also compares the numerical predictions obtained using the DG method with predictions by the two-flux approximation [Equation (5.5)] and by the simplified two-flux approximation [Equation (5.26)]. The average relative difference between the numerical predictions using DG method with DOS-ISW and the two-flux approximation for $G_{PAR}(z)$ at the centerline of the open pond ranged between 4 and 10% depending on the time of the day and the location inside the PBR. However, prediction by the two-flux approximation was not able to predict the shadow and other multidimensional effects in the open pond. Moreover, the average total specific growth rate $\bar{\mu}$ predicted based on $G_\lambda(z)$ and $G_{PAR}(z)$ predicted by the two-flux approximation fell within 1 to 7% of its numerically predicted value [Equation (5.12)]. These results suggest that the two-flux approximation can be used to determine $G_{PAR}(z)$ and the corresponding $\bar{\mu}$ in open ponds or race ponds with dimensions larger than 2 m when shadow effects become less and less significant. This can be very useful in the design and real time control and operation of open ponds.

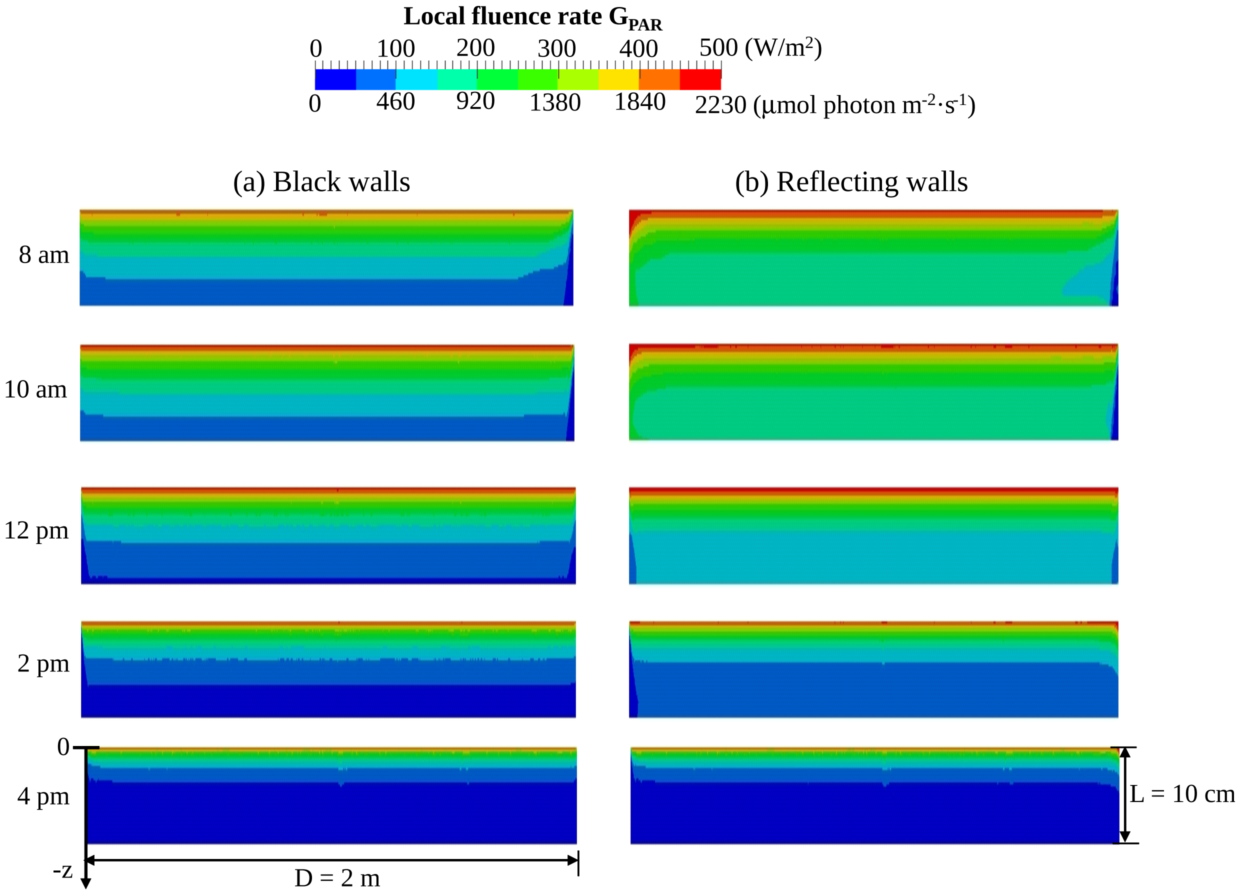

Figure 5.4: Computed PAR-averaged local fluence rate $G_{PAR}(\mathbf{r})$ on June 21 at 8:00 am, 10:00 am, 12:00 pm, 2:00 pm, and 4:00 pm in the midplane of an open pond located in Los Angeles, USA (34.04°N, 118.15°W) having diameter $D = 2$ m and depth $L = 0.1$ m with (a) black walls or (b) reflecting walls for initial mass concentration $X_0 = 0.1$ kg/m^3.

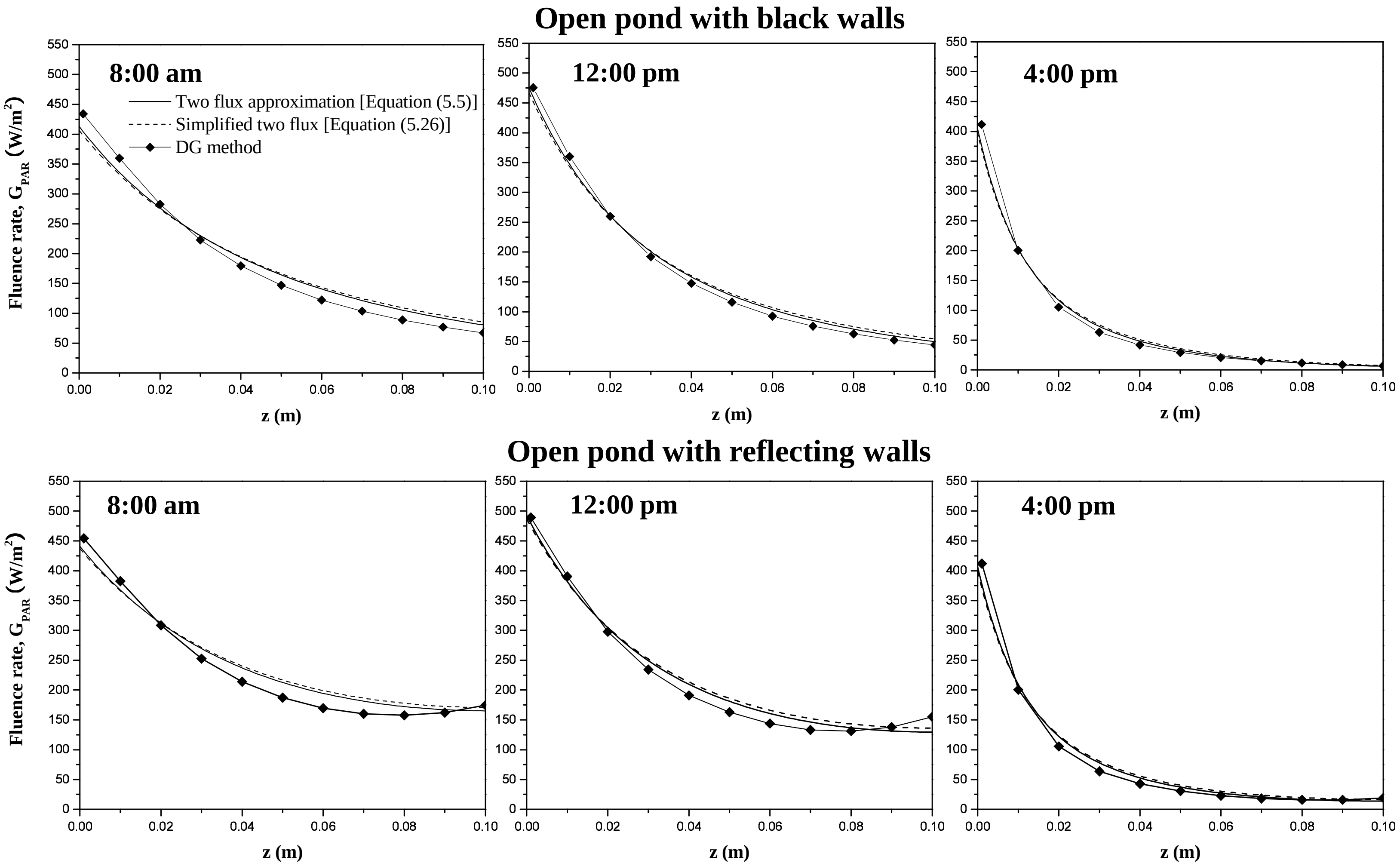

Figure 5.5: PAR-averaged local fluence rate $G_{PAR}(\mathbf{r})$ predicted on June 21 in Los Angeles, USA (34.04°N, 118.15°W) at 8:00 am, 12:00 pm, and 4:00 pm in the centerline of an open pond PBR predicted by (i) DG method with DOS-ISW, (ii) two-flux approximation [Equation(5.5)], and (iii) simplified two-flux approximation [Equation(5.26)]. The pond featured black or reflecting walls and had diameter $D = 2$ m and depth $L = 0.1$ m for initial mass concentration $X_0 = 0.1$ kg/m^3.

5.4.1.2 Effect of cellular respiration

Figure 5.6 shows (a, b) the average specific growth rate $\bar{\mu}$ and (c, d) the mass concentration ratio X/X_0 of *C. reinhardtii* as function of time obtained without and with accounting for cellular respiration in open pond of depth $L = 0.1$ m with black walls. The initial mass concentrations X_0 were varied from 0.05 to 1.0 kg/m^3. The local fluence rate $G_\lambda(z)$ was estimated by the two-flux approximation and the average specific growth rate was calculated by Equations (5.10) to (5.12). Figures 5.6a and 5.6b indicate that at low initial mass concentration $X_0 = 0.05$ kg/m^3, the relative difference in the specific growth rate without and with respiration varied between 11 and 21% depending on the time of the day. However, at high initial mass concentration $X_0 = 1.0$ kg/m^3, it varied between 58 and 70%. Therefore, the effect of cellular respiration on the average specific growth rate was more significant for high initial mass concentration.

Figures 5.6c and 5.6d show that at low initial mass concentration $X_0 = 0.05$ kg/m^3, the mass concentration ratio in the open ponds after 12 hours without and with respiration increased by a factor of about 4.0 and 5.7, respectively. The mass concentration achieved accounting for respiration was 30% smaller than when ignoring respiration. Similar relative decrease in mass concentration was observed for $X_0 = 1.0$ kg/m^3 when accounting for respiration. These results demonstrate that cellular respiration must be accounted for in simulating coupled light transfer and growth kinetics in PBRs.

5.4.1.3 Comparison of growth kinetics models

Figure 5.7 compares (a) the average total specific growth rates $\bar{\mu}$ and $\bar{\mu}'$ based on the average fluence rate [Equation (5.14)] and (b) the corresponding microalgae mass concentration $X(t)$ as a function of time for open pond with depth $L = 0.1$ m and initial mass concentration X_0 equal to 0.1 and 1.0 kg/m^3. The local

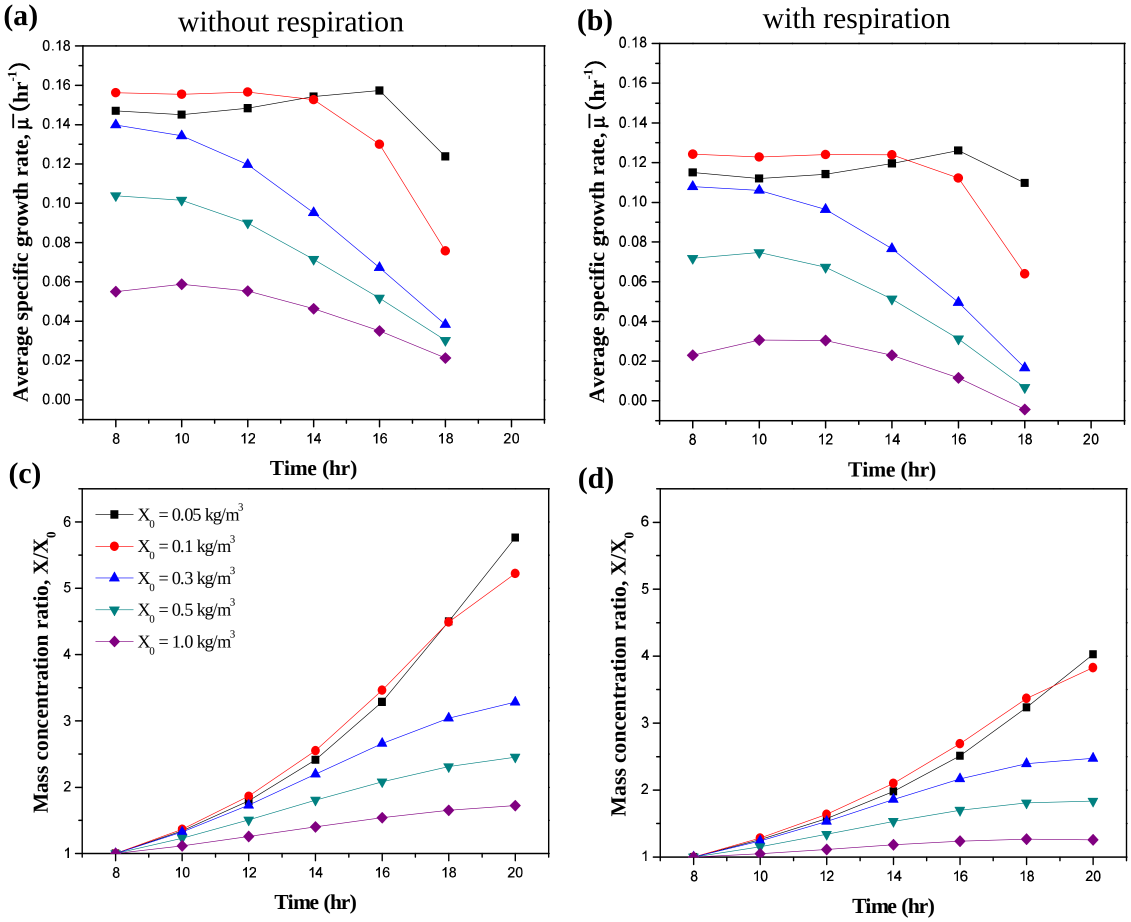

Figure 5.6: Comparison of (a, b) the average specific growth rate $\bar{\mu}$ and (c, d) *C. reinhardtii* mass concentration ratio $X(t)/X_0$ as a function of time without and with respiration for initial mass concentration X_0 between 0.05 and 1.0 kg/m^3. The open pond was of depth $L = 0.1$ m located in Los Angeles, USA (34.04°N, 118.15°W) on June 21 and had black walls.

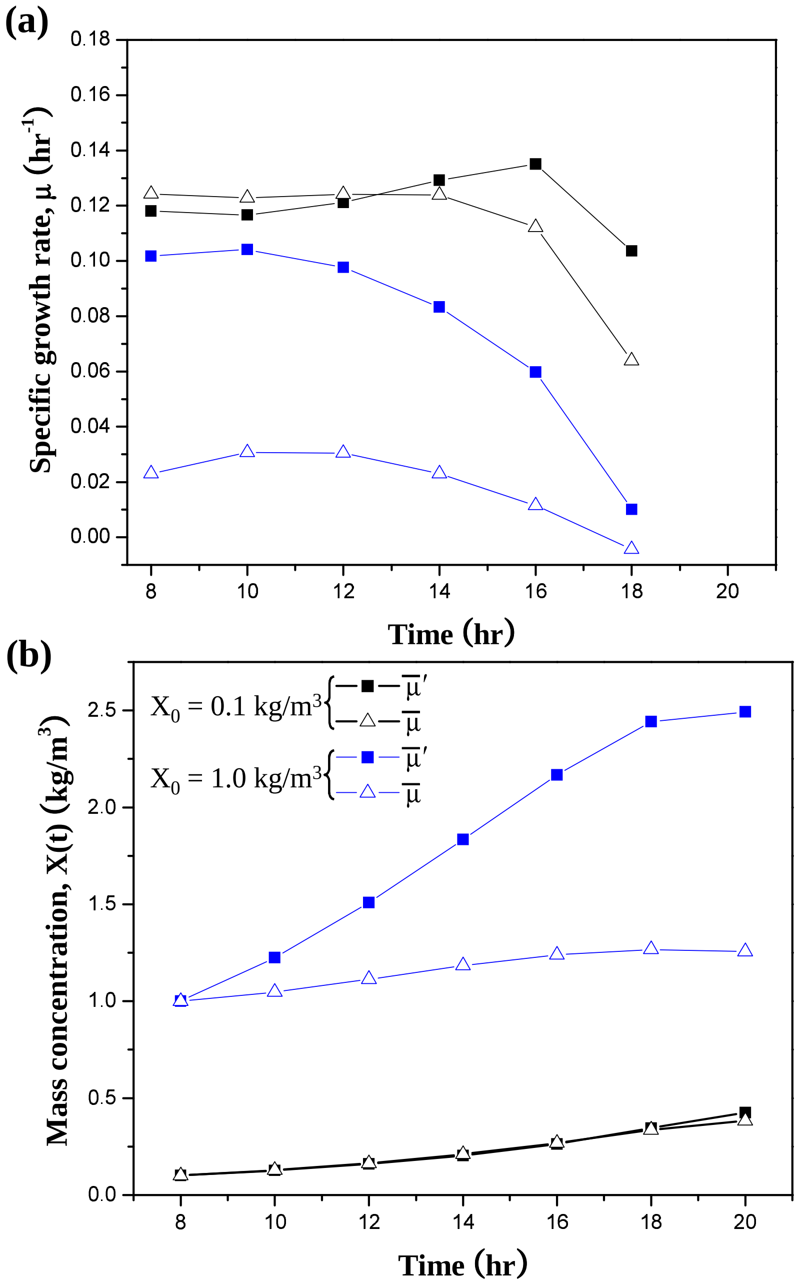

Figure 5.7: Comparison of (a) the average specific growth rate $\bar{\mu}$ [Equation(5.12)] and $\bar{\mu}'$ [Equation(5.14)] and (b) the corresponding mass concentrations $X(t)$ for open pond with depth $L = 0.1$ m and initial mass concentration $X_0 = 0.1$ and 1.0 kg/m^3 located in Los Angeles, USA (34.04°N, 118.15°W) on June 21 and having black walls.

fluence rate was calculated by the two-flux approximation. At low initial mass concentration $X_0 = 0.1$ kg/m^3, the relative difference between the average total specific growth rates $\bar{\mu}$ and $\bar{\mu}'$ was less than 5% until 2:00 pm when $X(t)$ was about 0.2 kg/m^3. However, after 2:00 pm, $\bar{\mu}$ and $\bar{\mu}'$ differed by 20% resulting in mass concentration at 8:00 pm of 0.38 and 0.42 kg/m^3, respectively. Furthermore, at high initial mass concentration $X_0 = 1.0$ kg/m^3, $\bar{\mu}$ and $\bar{\mu}'$ were significantly different throughout the day and the associated final mass concentration at 8:00 pm were 1.2 and 2.5 kg/m^3, respectively. The specific growth rate based on the average fluence rate $\bar{\mu}'$ overestimated the volume-averaged growth rate $\bar{\mu}$ because it did not account for the local light limitation and/or inhibition since it averages $G_{PAR}(z)$ over the entire PBR volume. However, at high mass concentration local light limitation and inhibition can be severe. These results demonstrated that the more rigorous expression of the average specific growth rate $\bar{\mu}$ given by Equation (5.12) must be used to predict microalgae growth at high mass concentration.

5.4.1.4 Daily occupied areal productivity

The daily areal biomass productivity of a PBR, expressed in kg/m^2/day, is defined as the mass of microalgae produced after 12 hours of exposure to sunlight per unit illuminated surface area exposed to collimated solar irradiance. It is expressed as

$$P_{op} = \frac{(X_f - X_0)V}{St_f} = \frac{(X_f - X_0)}{at_f} \tag{5.27}$$

where S and V are the illuminated surface area and volume of the PBR while X_f is the final mass concentration and t_f is equal to 1 day. The specific illuminated area of the PBRs, denoted by a (in m^{-1}), is defined as $a = S/V$ [153]. For an open pond of diameter D, thickness L, and illuminated surface area $S = \pi D^2/4$, the specific illuminated area is equal to $a_{op} = 1/L$. In addition, the initial optical thickness of open ponds is expressed as $\beta_\lambda L = (\bar{A}_{abs,\lambda} + \bar{S}_{sca,\lambda})X_0 L$ where the average mass cross-sections $\bar{A}_{abs,\lambda}$ and $\bar{S}_{sca,\lambda}$ are intrinsic properties of the microalgae species.

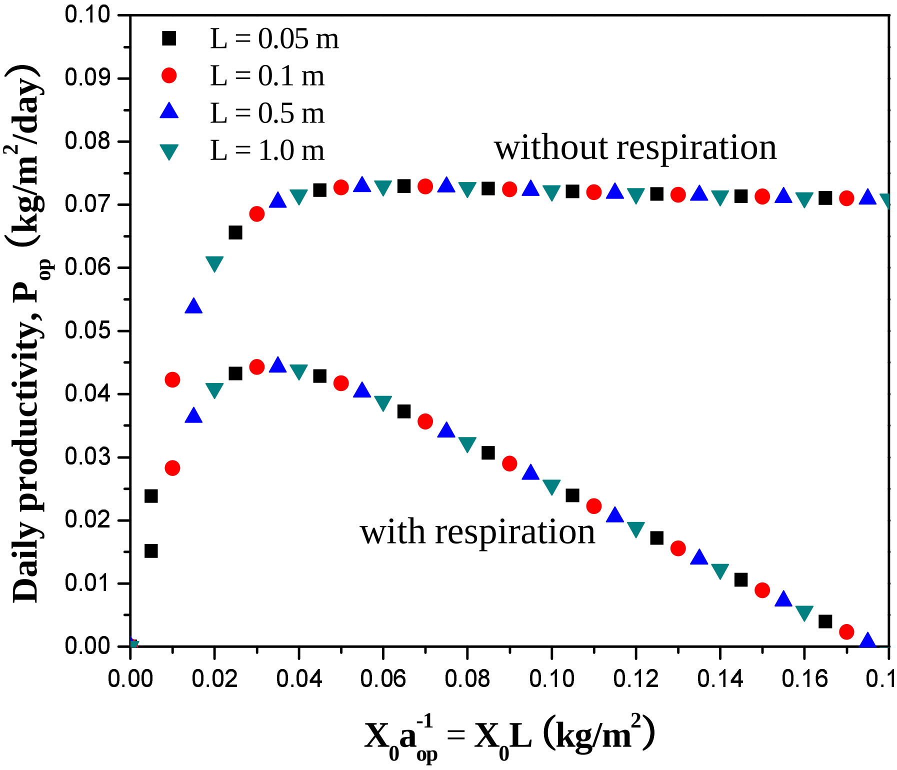

Figure 5.8: Comparison of daily areal biomass productivity per unit footprint $P_{f,op}$ of open pond with black walls growing *C. reinhardtii* as function of X_0L without and with in Los Angeles, USA (34.04°N, 118.15°W) on June 21.

Thus, $X_0L = X_0a_{op}^{-1}$ can be considered as representative of the PBR's initial optical thickness.

Figure 5.8 shows the daily areal biomass productivity per unit illuminated surface area of the open pond P_{op} without and with cellular respiration as a function of $X_0a_{op}^{-1}$ for depth L varying from 0.05 to 1.0 m and initial concentration X_0 between 0.1 and 5.0 kg/m^3. It is interesting to note that P_{op} depended uniquely on the product $X_0a_{op}^{-1} = X_0L$ and not on X_0 and $a_{op}^{-1} = L$ independently. This was true regardless of whether respiration was accounted for. Moreover, the daily areal biomass productivity per unit footprint of open pond P_{op} without respiration reached a plateau at about 0.07 kg/m^2/day for $X_0a_{op}^{-1}$ larger than 0.05

kg/m^2. However, the daily areal biomass productivity per unit footprint of open pond P_{op} with respiration featured a maximum at 0.045 kg/m^2/day for $X_0 a_{op}^{-1} =$ 0.035 kg/m^2. For $X_0 a_{op}^{-1} <$ 0.035 kg/m^2, the incident irradiance was not entirely absorbed by microalgae as some photons were absorbed at the bottom of the open pond and were wasted and productivity suffered. By contrast, for $X_0 a_{op}^{-1} >$ 0.035 kg/m^2, dark region appeared in the open pond thus decreasing the working illuminated volume while the effects of respiration became significant [166].

5.4.2 Vertical flat-plate photobioreactor

Light transfer in a vertical flat-plate photobioreactor oriented north-south with initial mass concentration $X_0 = 0.1$ kg/m^3 was simulated over 12 hours. The vertical flat-plate PBR height H, width W, and thickness L were taken as 2 m, 2 m, and 0.1 m, respectively. The walls were made of 8 mm thick glass panels. The effect of refraction due to mismatch in refractive indices of the air (n = 1.0), the reactor walls (n = 1.49), and the *C. reinhardtii* suspension (n = 1.33) contained in the PBR was investigated. These refraction indices were assumed to be constant over the PAR region. Reflection and refraction were estimated using Fresnel's equations for optically smooth and specularly reflecting surfaces [42].

Figure 5.9 shows the local PAR-averaged fluence rate $G_{PAR}(\mathbf{r})$ along a vertical cross-section of a 0.1 m thick flat-plate PBR accounting for refraction, at 8:00 am, 10:00 am, 12:00 pm (noon), 2:00 pm, 4:00 pm, and 6:00 pm. Three-dimensional effects were apparent between 10:00 am and 2:00 pm when the sun was near its zenith.

Figure 5.10 shows the PAR-averaged local fluence rate $G_{PAR}(x)$ predicted at the centerline of the vertical flat-plate at 10:00 am, 2:00 pm, and 6:00 pm (a) without and (b) with refraction by the PBR walls. Accounting for refraction reduced slightly the local fluence rate due to reflection of the incident solar radiation by the glass wall estimated to be around 4%. The relative difference in *C. reinhardtii* mass concentration after 12 hours was less than 0.1% when considering or ignoring refraction. Therefore, refraction of sunlight by the front and back windows of the PBR had negligible effects on the mass concentration of microalgae and could be ignored in our simulations.

Figure 5.10 also compares numerical results with predictions from the two-flux approximation [Equation (5.21)] and the simplified two-flux approximation [Equations (5.24)]. The maximum relative difference between numerical results and predictions by the two-flux approximation for the local $G_{PAR}(x)$ without refraction ranged between 4 and 22% while the relative differences averaged over the PBR volume were about 2 to 13% depending on the time of the day. The two-flux approximation tended to overpredict $G_{PAR}(x)$ because it was not able to predict the shadow and other multidimensional effects.

Moreover, the average total specific growth rate $\bar{\mu}$ estimated using $G_{PAR}(x)$ predicted by the two-flux approximation [Equation (5.21)] fell within 2 to 10% of its numerically predicted values. Overall, the two-flux approximation predictions of $G_{PAR}(x)$ and the corresponding average total specific growth rate $\bar{\mu}$ in vertical flat-plate PBRs were acceptable. It was used in combination with the Monod model to predict the daily biomass productivity.

Finally, the average total specific growth rate $\bar{\mu}$ in the vertical flat-plate PBR was found to be larger than that of an open pond of identical depth with black walls at all times except at 12:00 pm because the surface area exposed to sunlight was smaller.

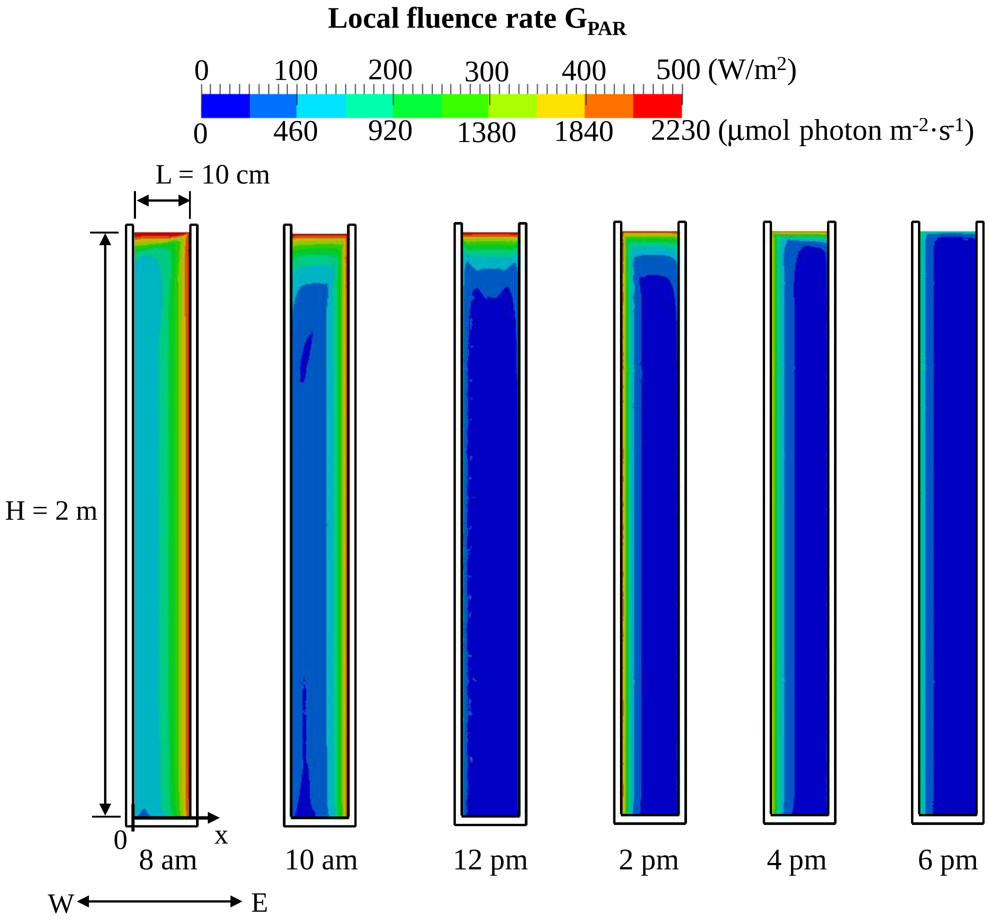

Figure 5.9: Computed PAR-averaged local fluence rate $G_{PAR}(\mathbf{r})$ at 8:00 am, 10:00 am, 12:00 pm, 2:00 pm, 4:00 pm, and 6:00 pm with refraction by the walls in the midplane of a vertical flat-plate located in Los Angeles, USA (34.04°N, 118.15°W) having height $H = 2$ m, width $W = 2$ m, and thickness $L = 0.1$ m with initial mass concentration $X_0 = 0.1$ kg/m^3 on June 21.

(a) Vertical flat-plate without refraction

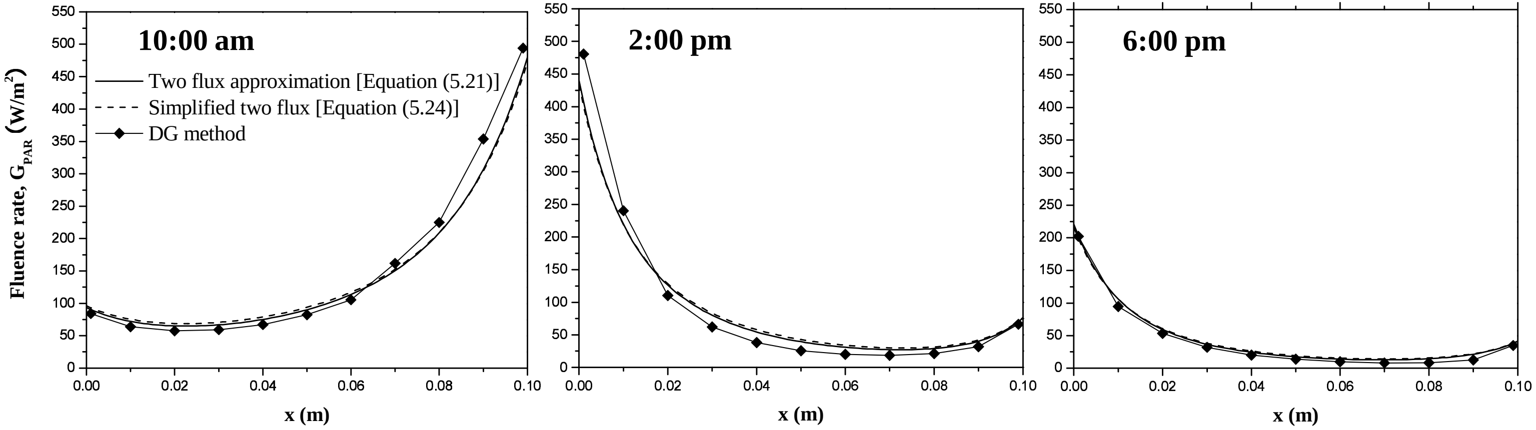

(b) Vertical flat-plate with refraction

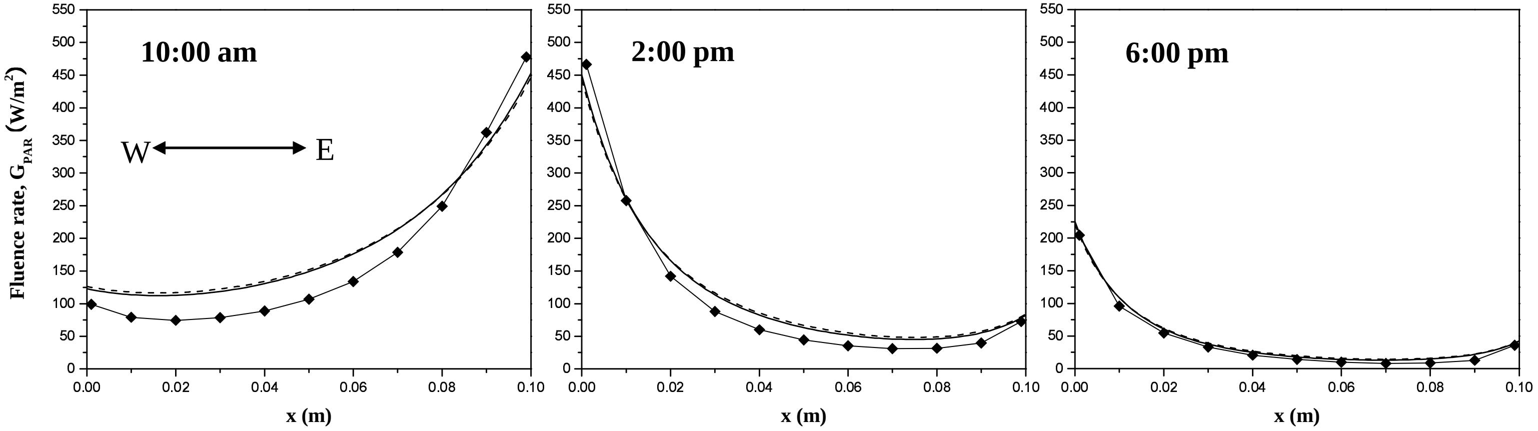

Figure 5.10: PAR-averaged local fluence rate $G_{PAR}(\mathbf{r})$ at 10:00 am, 2:00 pm, and 6:00 pm in the centerline of a vertical flat-plate located in Los Angeles, USA (34.04°N, 118.15°W) predicted by (i) DG method with DOS-ISW, (ii) two-flux approximation [Equation (5.21)], and (iii) simplified two-flux approximation [Equation (5.24)]. The vertical flat-plate (a) without and (b) with refraction by the walls had height $H = 2$ m, width $W = 2$ m, and thickness $L = 0.1$ m with initial mass concentration $X_0 = 0.1$ kg/m^3. $G_{PAR}(\mathbf{r})$ was predicted on June 21.

5.4.3 Tubular photobioreactor

A horizontal tubular photobioreactor oriented in the north-south direction with initial mass concentration $X_0 = 0.1$ kg/m^3 was simulated over 12 hours on June 21. Here, the tubular PBR diameter L was taken as 0.1 m. Figure 5.11 shows the local PAR-averaged fluence rate $G_{PAR}(\mathbf{r})$ over the cross-section of the pipe at different times of the day. It shows significant multidimensional effects. A darker region developed in the center of the tubular PBR under the combined effects of microalgae growth and the setting of the sun. Given the inherent 2D nature of this type of PBRs, the two-flux approximation could not be used.

5.4.4 Comparison of daily biomass productivities

The daily areal biomass productivity per unit surface area exposed to collimated solar irradiance for vertical flat-plate and tubular PBRs, respectively denoted by P_{fp} and P_{tb} (in kg/m^2/day), are also defined by Equation (5.27). The specific illuminated area of flat-plate PBRs of thickness L is expressed as $a_{fp} = 1/L$ and that of tubular PBRs of diameter L is equal to $a_{tb} = 2/L$. In other words,

$$P_{fp} = \frac{(X_f - X_0)L}{t_f} \quad \text{and} \quad P_{tb} = \frac{(X_f - X_0)L/2}{t_f} \tag{5.28}$$

Here also, X_f is the final concentration after a duration t_f of one day.

Figure 5.12 shows the daily areal biomass productivity of open ponds P_{op}, vertical flat-plate P_{fp}, and tubular PBRs P_{tb} as a function of $X_0 a^{-1}$ for different values of their characteristics length L (i.e., depth, thickness, or diameter) varying from 0.05 to 1.0 m and initial concentration X_0 between 0.0 and 5.0 kg/m^3. The daily areal biomass productivity of vertical flat-plate P_{fp} was calculated based on $\bar{\mu}$ estimated with $G_{PAR}(x)$ predicted by the two-flux approximation, ignoring wall refraction, and accounting for respiration. On the other hand, P_{tb} was calculated numerically based on $G_{PAR}(\mathbf{r})$ and $\bar{\mu}$. It is interesting to note that the daily biomass productivities P_{op}, P_{fp}, and P_{tb} nearly overlapped and were unique

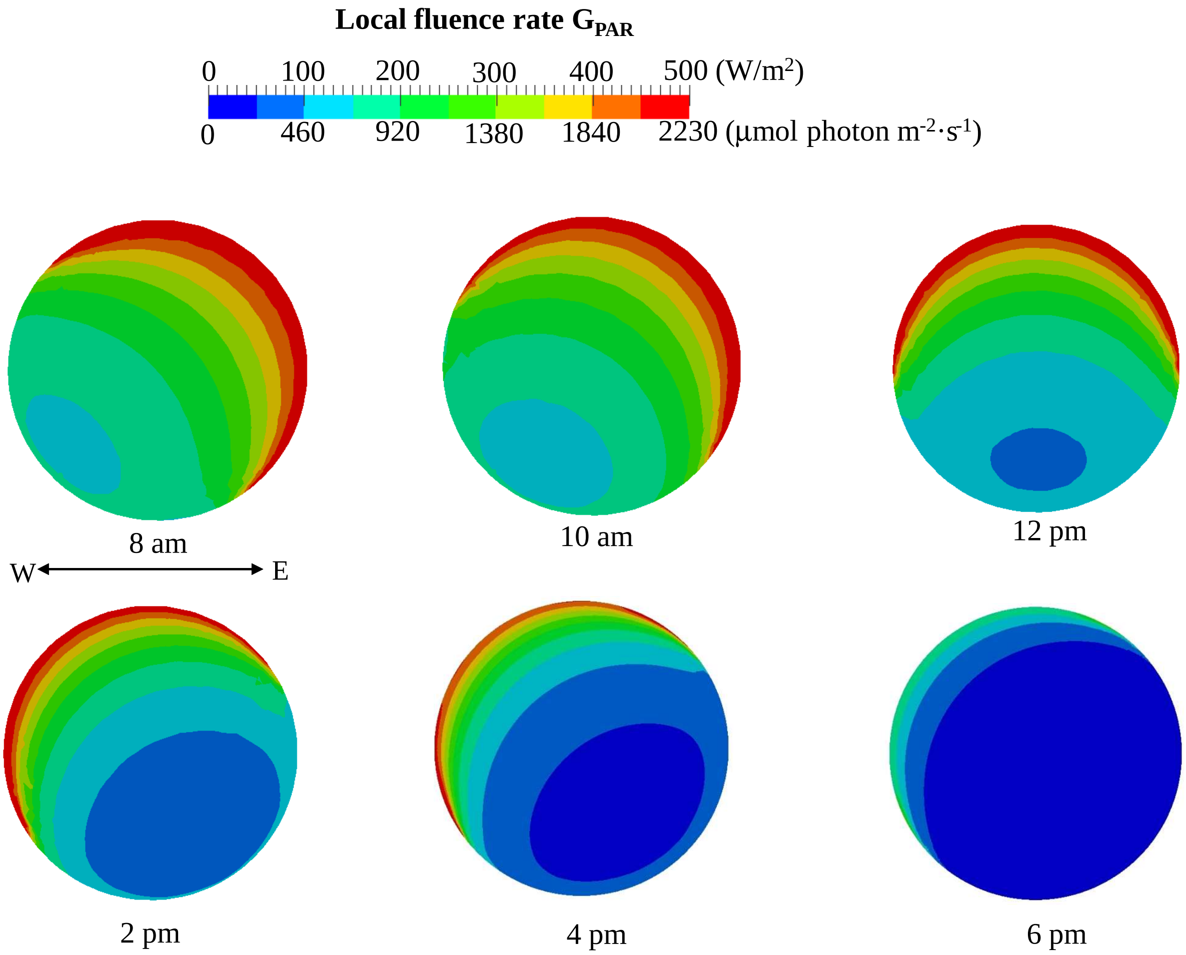

Figure 5.11: Computed local PAR-averaged fluence rate $G_{PAR}(\mathbf{r})$ at 8:00 am, 10:00 am, 12:00 pm, 2:00 pm, 4:00 pm, and 6:00 pm in the cross-section of a north-south oriented tubular photobioreactor located in Los Angeles, USA (34.04°N, 118.15°W) having diameter $L = 0.1$ m with initial mass concentration $X_0 = 0.1$ kg/m^3 on June 21.

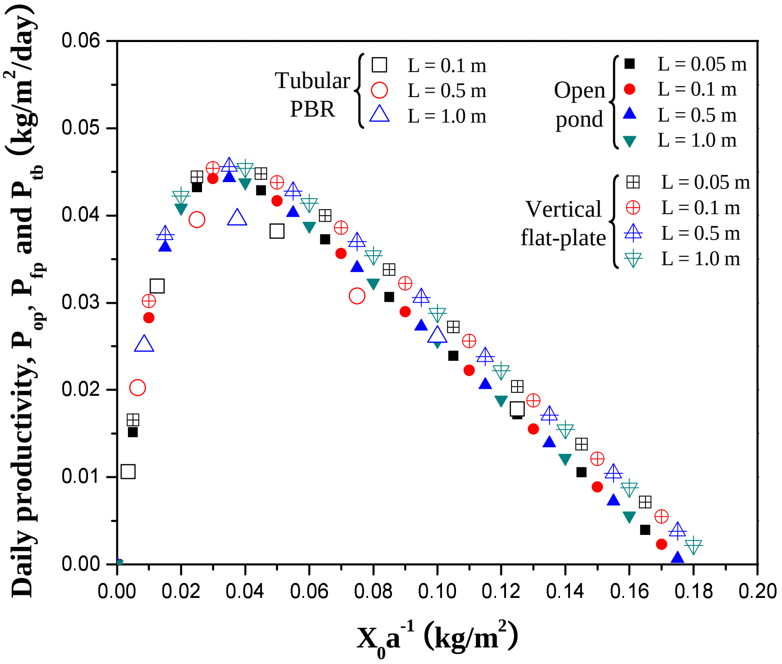

Figure 5.12: Daily areal biomass productivity per unit illuminated surface area exposed to collimated solar irradiance predicted on June 21 in Los Angeles for open ponds P_{op}, vertical flat-plate PBRs P_{fp}, and tubular PBRs P_{tb} for *C. reinhardtii* as function of X_0a^{-1} with depth or diameter L varying from 0.05 to 1.0 m and initial concentration X_0 between 0.1 and 5.0 kg/m^3. Here, $a_{op} = 1/L$, $a_{fp} = 1/L$, and $a_{tb} = 2/L$.

function of X_0a^{-1}. The maximum daily areal productivity per unit illuminated surface area of these PBRs was $P_{max} = 0.045$ kg/m^2/day for $X_0a^{-1} = 0.035$ kg/m^2. Note that the fact that the maximum productivity is identical for PBRs with the same specific illuminated area a irrespective of their geometry has already been predicted by Cornet and Dussap [153] and experimentally validated by Takache *et al.* [158]. Here, we expanded this conclusion by demonstrating that the productivities per unit of illuminated surface area of PBRs are identical (including at their maximum) as long as they feature the same value of optical thickness represented by X_0a^{-1}. These results should be evaluated in combination with the associated capital and operational costs [167]. Shading between cultivation systems should also be considered depending on the specific design configuration.

Finally, the fact that daily biomass productivities P_{op}, P_{fp}, and P_{tb} depend only on the product X_0a^{-1} provides a simple and practical way to design (via a) and to operate these PBRs (via X_0) to achieve maximum productivity in batch mode. However, one may wonder if these results are valid for (i) other types of PBRs, (ii) for continuous operation, (iii) for different light transfer and growth kinetic models, and if they are supported by experimental evidences.

5.4.5 Comparison with experimental data and other models

Pruvost *et al.* [20] cultivated *Neochloris oleoabundans* in vertical flat-plate air-lift PBRs operated in continuous mode with different thicknesses $L = 0.03$ and 0.055 m. The authors also modeled the process using the two-flux approximation to calculate the fluence rate in the PBRs. The growth kinetics model ignored photoinhibition but accounted for respiration and for the effect of dilution to predict the volumetric and areal productivities. The parameters μ_0, K_S, and μ_s were estimated from experimental data as 0.21 hr^{-1}, 90 μmol photon m$^{-2}\cdot$ s^{-1}, and 0.005 hr^{-1}, respectively. Figure 5.13a shows the experimentally measured and predicted daily areal biomass productivity of vertical flat-plate air-lift PBRs reported by Pruvost *et al.* [20]. First, it indicates that the productivity measured experimentally had the same order of magnitude as those predicted in this study. Figure 5.13a also establishes that the areal productivity of continuous air-lift PBRs was also a unique function of X_0a^{-1}.

Moreover, Figure 5.13b shows the simulation results reported by Slegers *et al.* [21] for yearly volumetric biomass production (in kg/m^3/year) for vertical flat-plate PBRs operated in continuous mode with *P. tricornutum* and *T. pseudonana.* Here, the PBR thickness ranged from 0.05 to 0.1 m and concentrations varied

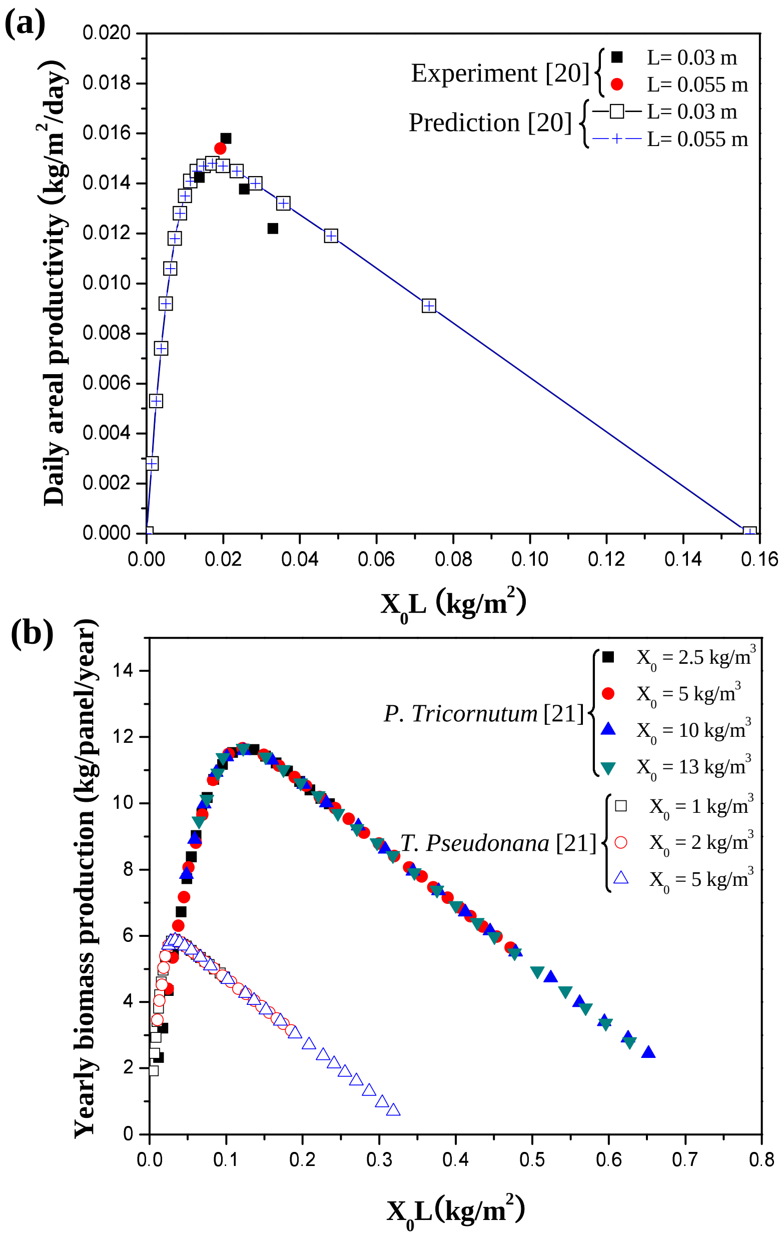

Figure 5.13: (a) Experimentally measured and predicted daily areal biomass productivity as a function of X_0a^{-1} [20] for continuous vertical air-lift flat-plate PBR of thickness L equals to 3 or 5.5 cm with *N. oleoabundans*. (b) Collapse of the predicted yearly volumetric biomass productivity shown in Fig. 3 in Ref. [21] plotted as function of X_0a^{-1} for 1 m tall vertical flat-plate PBRs in continuous operation with L varying from 0.05 to 0.1 m and X_0 between 1.0 and 13.0 kg/m^3 for *P. tricornutum* and *T. pseudonana*.

between 1.0 and 13.0 kg/m^2. It is very interesting to observe that these data obtained independently using different light and kinetics models collapsed also on a single line when plotted as a function of X_0a^{-1}, whereas they were scattered when plotted as a function of $L = 1/a$ (Figure 3 in Ref. [21]).

5.5 Conclusions

This study presented accurate 3D numerical simulations for coupled light transfer and growth kinetics in the most commonly used PBRs exposed to collimated and diffuse sunlight in Los Angeles on June 21. The local fluence rate was predicted on a spectral basis by solving the 3D RTE. The temporal evolution of microalgae mass concentration was predicted by accounting for light saturation, photolimitation, and respiration. In open ponds, the reflecting walls resulted in a more uniform light distribution and increased the local fluence rate. However, the difference in overall biomass concentration after 12 hours was negligible. Similarly, refraction by the container walls, in vertical flat-plate PBRs, had no significant effect on the microalgae concentration. The study demonstrated that the two-flux approximation can be used to estimate the local fluence rate in open (or race) ponds and flat-plate PBRs for all practical purposes including designing, controlling, and operating PBRs. The average specific growth rate should be estimated by volume-averaging the local growth rate [Equations (5.10) to (5.12)] instead of using the volume-averaging fluence rate G_{av} [Equations (5.13) and (5.14)]. This is particularly important for high microalgae concentrations. Cellular respiration significantly affects the daily productivity and should also be accounted for. Finally, the daily areal biomass productivity per illuminated surface area was found to depend uniquely on the initial optical thickness represented by X_0a^{-1} for open ponds and tubular PBRs operated in batch mode. Similar results were obtained for the daily productivity per unit surface area illuminated for flat-plate PBRs.

What's more, the same conclusions were drawn by revisiting both experimental data and numerical simulations reported in the literature for similar and other PBR types cultivating other microorganisms in continuous mode. The parameter X_0a^{-1} is useful and simple for designing (via a) and operating (via X_0) these PBRs at their maximum productivity.

CHAPTER 6

Conclusions and Recommendations

6.1 Summary

This section summarizes the conclusions of the present study and its contributions to the development of photobiological carbon dioxide fixation and fuel production.

6.1.1 GPU-Based Radiative Transfer Equation Solver

- High-order discontinuous Galerkin (DG) method was successfully implemented to solve the radiative transfer equation (RTE) with finite volume (FVM) and discrete ordinates method (DOM) for angular discretization.
- Non-gray gas radiation models such as spectral line-based weighted-sum-of-gray-gases (SLW) and hybrid SNBCK models were incorporated with DG method and validated.
- Radiative transfer in various 3D enclosures was modeled with diffusively or specularly reflecting walls along with diffuse and collimated incident irradiation.
- This study demonstrated that the porting of the DG RTE solver to GPUs had very attractive computational speedup. The speedup was up to 4.0 compared with comparable CPU computing and increased with increasing DG scheme order for 3D square enclosure having cold black walls and containing a gray, absorbing, emitting, and non-scattering medium.

6.1.2 Spectral Optical Properties of Spherical Green Microalgae *C. reinhardtii* CC125 and Its Truncated Chlorophyll Antenna Transformants

- This study presented a methodology to retrieve the spectral refraction and absorption indices of homogeneous spheres from experimentally measured average absorption and scattering cross-sections.

- The methodology was demonstrated with unicellular green microalgae between 400 and 750 nm. The retrieved refraction and absorption indices were continuous function of wavelength with apparent absorption peaks corresponding to those of *in vivo* Chl *a* and *b*. These optical properties can be used to predict the radiation characteristics of the species considered using Lorentz-Mie theory for a given size distribution.

6.1.3 Radiation Characteristics of filamentous Microorganisms

- This study demonstrated that the absorption and scattering cross-sections per unit length of randomly oriented clusters of multiple connected and aligned spheres asymptotically approach those of randomly oriented and infinitely long cylinders with volume equivalent radius as the number of sphere increased.

6.1.4 Modeling and Design Guidelines for Outdoor Photobioreactors

- This study presented 3D numerical simulations for coupled light transfer and growth kinetics in commonly used PBRs exposed to collimated and diffuse sunlight. The temporal evolution of microalgae mass concentration was predicted by accounting for light saturation, photolimitation, and respiration.

- Open ponds with reflecting walls featured more uniform and larger fluence rates. However, the difference in overall biomass concentration after 12 hours was negligible.

- Refraction by the container walls, in vertical flat-plate PBRs, had no significant effect on the microalgae growth and final concentration.
- The two-flux approximation can be used to estimate the local fluence rate in open (or race) ponds and flat-plate PBRs with good accuracy.
- For a given microorganism species, the daily areal biomass productivity per illuminated surface area was found to depend uniquely on the initial optical thickness represented by X_0a^{-1} for open pond and vertical flat-plate and tubular PBRs operated in batch mode.
- The results were also valid for experimental data and numerical simulations reported in the literature for various PBRs cultivating other microorganisms in continuous mode.

6.2 Recommendations for Future Research

Recommendations for future research on photobiological carbon dioxide fixation and fuel production are as follows.

6.2.1 GPU-Based Radiative Transfer Equation Solver

- Line-by-line (LBL) model provides detailed spectral values of transmissivity and absorption coefficient. This model is more accurate than narrow band model and can be combined easily with the radiative transfer equation solver. Obviously, solving the radiative transfer equation line-by-line requires a significant amount of time compared with the narrow band model.

However, computational time can be dramatically reduced by using GPU computing. If the line-by-line calculations using GPU can take as much time as narrow band calculations with central processing unit (CPU), the combination will provide an accurate method for a reasonable computational time without any approximation in the gas radiation models.

6.2.2 Spectral Optical Properties of Spherical Green Algae *C. reinhardtii* and Its Truncated Chlorophyll Antenna Transformants

- The mass fractions of the three pigments Chl *a*, Chl *b*, and photoprotective carotenoids (PPC) were retrieved from the retrieved absorption index k_λ using Equation (3.4). The previously retrieved k_λ and that predicted using the fitted pigment mass fractions were in fair agreement. It indicates that a new model is required to predict the accurate absorption index with mass fractions of the pigments.

- The lipid content in microorganisms is a very important parameter to select promising species for biofuel production. However, the extraction and measurement of lipid content are difficult and time-consuming. Therefore, the retrieved refraction index could be used to estimate the lipid content of microorganisms. Equation (3.3) could be further developed for not only intracellular carbon concentration but also lipid content.

6.2.3 Radiation Characteristics of Filamentous Microorganisms

- Current version of the T-matrix code [22] cannot predict the radiation characteristics with size parameters larger than 10. However, many microorganisms and various aggregates of spherical particles feature large size parameter. Therefore, the code needs to be modified to handle large size parameters.

- Based on the results of the present study, the refractive and absorption indices of filamentous cyanobacteria should be retrieved by combining the Lorentz-Mie theory code for infinitely long and randomly oriented cylinders with the inverse mathod developed in Chapter 3.

6.2.4 Modeling and Design Guidelines for Outdoor Photobioreactors

- Photobioreactors containing microorganisms are often assumed to be well mixed so that the microorganism mass concentration is uniform. That is likely valid for benchtop or laboratory scale photobioreactors. However, achieving uniform mixing is an important challenge for large scale PBRs. Then, the local mass concentration of microalgae in the PBR can be predicted by coupling not only the radiative transfer and growth kinetics solver but also a computational fluid dynamics (CFD) solver able to predict the turbulent mixing. Then, the flow rate of medium, mass concentration, mixing mechanism, and the PBR geometries can be optimized to achieve maximum productivity.

- PBRs are often assumed to be operated at constant temperature. In fact, PBRs should be maintained at optimum temperature to achieve maximum productivity. However, outdoor PBRs suffer from large temperature fluctuation during the day. Solar radiation and weather cycle can significantly affect the temperature of PBRs [168]. These temperature fluctuations also influence the growth kinetics [169]. Therefore, the controls of temperature such as cooling and heating are needed for the maximum productivity. The temperature of PBRs could be predicted and optimized by using radiative and convective heat transfer analysis.

APPENDIX A

Spectral Optical Properties Data of microalgae

A.1 *Chlamydomonas reinhardtii* CC125

Table A.1: Spectral Optical Properties Data of *Chlamydomonas reinhardtii* CC125 in the spectral range from 400 to 750 nm.

λ (nm)	n_λ	k_λ	λ (nm)	n_λ	k_λ
400	1.35677	0.00347	510	1.35545	0.00208
410	1.35525	0.00411	520	1.35621	0.00132
420	1.35406	0.00464	530	1.35650	0.00094
430	1.35303	0.00516	540	1.35671	0.00083
436	1.35257	0.00535	550	1.35685	0.00079
440	1.35257	0.00535	560	1.35701	0.00080
450	1.35327	0.00469	570	1.35709	0.00095
460	1.35321	0.00446	580	1.35708	0.00113
470	1.35281	0.00466	590	1.35719	0.00130
476	1.35266	0.00474	600	1.35732	0.00141
480	1.35274	0.00470	610	1.35736	0.00159
490	1.35331	0.00423	620	1.35751	0.00179
500	1.35441	0.00315	630	1.35758	0.00188

Continued on next page

Table A.1 – continued

λ (nm)	n_λ	k_λ	λ (nm)	n_λ	k_λ
640	1.35746	0.00227	700	1.36172	0.00082
650	1.35694	0.00331	710	1.36257	0.00028
660	1.35654	0.00411	720	1.36311	0.00012
670	1.35545	0.00564	730	1.36356	0.00005
676	1.35544	0.00593	740	1.36393	0.00005
680	1.35597	0.00563	750	1.36449	0.00001
690	1.35939	0.00264			

A.2 *Chlamydomonas reinhardtii tla1*

Table A.2: Spectral Optical Properties Data of *Chlamydomonas reinhardtii tla1* in the spectral range from 400 to 750 nm.

λ (nm)	n_λ	k_λ	λ (nm)	n_λ	k_λ
400	1.35761	0.00200	476	1.35466	0.00267
410	1.35665	0.00244	480	1.35474	0.00264
420	1.35576	0.00282	490	1.35511	0.00230
430	1.35503	0.00317	500	1.35571	0.00167
436	1.35457	0.00330	510	1.35635	0.00107
440	1.35457	0.00327	520	1.35671	0.00066
450	1.35507	0.00278	530	1.35700	0.00049
460	1.35501	0.00256	540	1.35721	0.00040
470	1.35461	0.00266	550	1.35725	0.00041

Continued on next page

Table A.2 – continued

λ (nm)	n_λ	k_λ	λ (nm)	n_λ	k_λ
560	1.35741	0.00041	670	1.35725	0.00314
570	1.35749	0.00049	676	1.35734	0.00330
580	1.35768	0.00058	680	1.35797	0.00311
590	1.35779	0.00067	690	1.36059	0.00143
600	1.35782	0.00073	700	1.36232	0.00043
610	1.35796	0.00084	710	1.36277	0.00015
620	1.35811	0.00095	720	1.36311	0.00005
630	1.35818	0.00099	730	1.36336	0.00002
640	1.35816	0.00120	740	1.36362	0.00001
650	1.35804	0.00173	750	1.36409	0.00001
660	1.35784	0.00221			

A.3 *Chlamydomonas reinhardtii tlaX*

Table A.3: Spectral Optical Properties Data of *Chlamydomonas reinhardtii tlaX* in the spectral range from 400 to 750 nm.

λ (nm)	n_λ	k_λ	λ (nm)	n_λ	k_λ
400	1.35781	0.00325	440	1.35447	0.00556
410	1.35685	0.00397	450	1.35497	0.00463
420	1.35586	0.00465	460	1.35491	0.00429
430	1.35503	0.00530	470	1.35461	0.00445
436	1.35457	0.00557	476	1.35456	0.00448

Continued on next page

Table A.3 – continued

λ (nm)	n_λ	k_λ	λ (nm)	n_λ	k_λ
480	1.35464	0.00441	630	1.35808	0.00159
490	1.35501	0.00385	640	1.35826	0.00193
500	1.35571	0.00281	650	1.35794	0.00280
510	1.35635	0.00181	660	1.35774	0.00358
520	1.35691	0.00114	670	1.35715	0.00515
530	1.35730	0.00083	676	1.35724	0.00543
540	1.35721	0.00071	680	1.35777	0.00514
550	1.35735	0.00068	690	1.36049	0.00234
560	1.35751	0.00069	700	1.36222	0.00076
570	1.35749	0.00082	710	1.36287	0.00025
580	1.35768	0.00097	720	1.36331	0.00015
590	1.35779	0.00109	730	1.36376	0.00008
600	1.35792	0.00119	740	1.36423	0.00004
610	1.35796	0.00134	750	1.36459	0.00002
620	1.35811	0.00152			

A.4 *Chlamydomonas reinhardtii tla1-CW^+*

Table A.4: Spectral Optical Properties Data of *Chlamydomonas reinhardtii tla1-CW^+* in the spectral range from 400 to 750 nm.

λ (nm)	n_λ	k_λ	λ (nm)	n_λ	k_λ
400	1.35677	0.00347	410	1.35525	0.00411

Continued on next page

Table A.4 – continued

λ (nm)	n_λ	k_λ	λ (nm)	n_λ	k_λ
420	1.35406	0.00464	590	1.35719	0.00130
430	1.35303	0.00516	600	1.35732	0.00141
436	1.35257	0.00535	610	1.35736	0.00159
440	1.35257	0.00535	620	1.35751	0.00179
450	1.35327	0.00469	630	1.35758	0.00188
460	1.35321	0.00446	640	1.35746	0.00227
470	1.35281	0.00466	650	1.35694	0.00331
476	1.35266	0.00474	660	1.35654	0.00411
480	1.35274	0.00470	670	1.35545	0.00564
490	1.35331	0.00423	676	1.35544	0.00593
500	1.35441	0.00315	680	1.35597	0.00563
510	1.35545	0.00208	690	1.35939	0.00264
520	1.35621	0.00132	700	1.36172	0.00082
530	1.35650	0.00094	710	1.36257	0.00028
540	1.35671	0.00083	720	1.36311	0.00012
550	1.35685	0.00079	730	1.36356	0.00005
560	1.35701	0.00080	740	1.36393	0.00005
570	1.35709	0.00095	750	1.36449	0.00001
580	1.35708	0.00113			

References

[1] M. Morweiser, O. Kruse, B. Hankamer, and C. Posten, "Developments and perspectives of photobioreactors for biofuel production", *Applied Microbiology and Biotechnology*, vol. 87, pp. 1291–1301, 2010.

[2] R. Bidigare, M. Ondrusek, J. Morrow, and D. Kiefer, "In vivo absorption properties of algal pigments", *Ocean Optics X*, vol. 1302, pp. 290–301, 1990.

[3] H. Berberoğlu, A. Melis, and L. Pilon, "Radiation characteristics of *Chlamydomonas reinhardtii* CC125 and its truncated chlorophyll antenna transformants *tla1*, *tlaX*, and *tla1-CW*$^+$", *International Journal of Hydrogen Energy*, vol. 33, pp. 6467–6483, 2008.

[4] Protist information Server, "*Anabaena cylindrica*", `http://protist.i.hosei.ac.jp/pdb/Images/Prokaryotes/Nostocaceae/Anabaena/Anabaena$_11$b.html`.

[5] Israel Seambiotic Ltd., Tel Aviv, "Open ponds", `http://grin.hq.nasa.gov/ABSTRACTS/GPN-2000-000058.html`.

[6] Israel Alga Technologies (Algatech), Kibbutz Ketura, "Tubular photobioreactors", `http://www.algatech.com/`.

[7] AZ Arizona state university, Glendale, "Vertical flat-plate photobioreactors", `http://biofuels.asu.edu/biomaterials.shtml`.

[8] CA Exxon Mobile / Synthetic Genomics, La Jolla, "Polybag photobioreactors", `http://news.exxonmobil.com`.

[9] V. Goutière, F. Liu, and A. Charette, "An assessment of real-gas modelling in 2D enclosures", *Journal of Quantitative Spectroscopy and Radiative Transfer*, vol. 64, pp. 299–326, 2000.

[10] F. Liu, G.J. Smallwood, and O.L. Gulder, "Application of the statistical narrow-band correlated-k method to low-resolution spectral intensity and radiative heat transfer calculations - effects of the quadrature scheme", *International Journal of Heat and Mass Transfer*, vol. 43, no. 17, pp. 3119–3135, 2000.

[11] P.J. Coelho, "Fundamentals of a new method for the solution of the radiative transfer equation", *International Journal of Thermal Sciences*, vol. 44, pp. 809–821, 2005.

[12] T.-K. Kim and H. Lee, "Effect of anisotropic scattering on radiative heat transfer in two-dimensional rectangular enclosures", *International Journal of Heat and Mass Transfer*, vol. 31, pp. 1711–1721, 1988.

[13] D.N. Trivic, T.J. O'Brien, and C.H. Amon, "Modeling the radiation of anisotropically scattering media by coupling mie theory with finite volume method", *International Journal of Heat and Mass Transfer*, vol. 47, no. 26, pp. 5765 – 5780, 2004.

[14] G. Kamel, B.M. Naceur, M. Rachid, and S. Rachid, "Formulation and testing of the FT_n finite volume method for radiation in 3-D complex inhomogeneous participating media", *Journal of Quantitative Spectroscopy and Radiative Transfer*, vol. 98, pp. 425–445, 2006.

[15] S. Jendoubi, H.S. Lee, and T.-K. Kim, "Discrete ordinate solutions for radiatively participating media in a cylindrical enclosure", *Journal of Thermophysics and Heat Transfer*, vol. 7, no. 2, pp. 213–219, 1993.

[16] H. Berberoğlu, J. Yin, and L. Pilon, "Light transfer in bubble sparged photobioreactors for H_2 production and CO_2 mitigation", *International Journal of Hydrogen Energy*, vol. 32, pp. 2273 – 2285, 2007.

[17] S.C. Lee, "Radiative transfer through a fibrous medium: Allowance for fiber orientation", *Journal of Quantitative Spectroscopy and Radiative Transfer*, vol. 36, pp. 253–263, 1986.

[18] S. Fouchard, J. Pruvost, B. Degrenne, M. Titica, and J. Legrand, "Kinetic modeling of light limitation and sulfur deprivation effects in the induction of hydrogen production with *Chlamydomonas reinhardtii*: Part I. model development and parameter identification", *Biotechnology and Bioengineering*, vol. 102, pp. 232–245, 2009.

[19] M. Janssen, L. De Bresser, T. Baijens, J. Tramper, L.R. Mur, J.F.H. Snel, and R.H. Wijffels, "Scale-up aspects of photobioreactors: effects of mixing-induced light/dark cycles", *Journal of Applied Phycology*, vol. 12, pp. 225–237, 2000.

[20] J. Pruvost, G. Van Vooren, B. Le Gouic, A. Couzinet-Mossion, and J. Legrand, "Systematic investigation of biomass and lipid productivity by microalgae in photobioreactors for biodiesel application", *Bioresource Technology*, vol. 102, pp. 150 – 158, 2011.

[21] P.M. Slegers, R.H. Wijffels, G. van Straten, and A.J.B. van Boxtel, "Design scenarios for flat panel photobioreactors", *Applied Energy*, vol. 88, pp. 3342 – 3353, 2011.

[22] D.W. Mackowski and M.I. Mishchenko, "A multiple sphere T-matrix Fortran code for use on parallel computer clusters", *Journal of Quantitative Spectroscopy and Radiative Transfer*, vol. 112, pp. 2182–2192, 2011.

[23] M. I. Mishchenko and L. D. Travis, "Light scattering by polydispersions of randomly oriented spheroids with sizes comparable to wavelengths to observation", *Applied Optics*, vol. 33, pp. 7206–7225, 1994.

[24] L. Pilon, H. Berberoğlu, and R. Kandilian, "Radiation transfer in photobiological carbon dioxide fixation and fuel production by microalgae", *Journal of Quantitative Spectroscopy and Radiative Transfer*, vol. 112, pp. 2639 – 2660, 2011.

[25] K. Skjånes, P. Lindblad, and J. Muller, "BioCO_2 - a multidisciplinary, biological approach using solar energy to capture CO_2 while producing H_2 and high value products", *Biomolecular Engineering*, vol. 24, pp. 405–413, 2007.

[26] J.H. Yoon, S.J. Sim, M.S. Kim, and T.H. Park, "High cell density culture of *Anabaena variabilis* using repeated injections of carbon dioxide for the production of hydrogen", *International Journal of Hydrogen Energy*, vol. 27, pp. 1265–1270, 2002.

[27] IPPC, ", in *Climate Change 2007: Impacts, Adaptation and Vulnerability. Contribution of Working Group II to the Fourth Assessment Report of the Intergovernmental Panel on Climate Change*, Cambridge, UK, 2007, Cambridge University Press.

[28] A. Kumar, S. Ergas, X. Yuan, A. Sahu, Q. Zhang, J. Dewulf, F.X. Malcata, and H. van Langenhove, "Enhanced CO_2 fixation and biofuel production via microalgae: recent developments and future directions", *Trends in Biotechnology*, vol. 28, pp. 371–380, 2010.

[29] J.R. Bolton and D.O. Hall, "The maximum efficiency of photosynthesis", *Photochemistry and Photobiology*, vol. 53, pp. 545–548, 1991.

[30] J.A. Asenjo and J.C. Merchuk, *Bioreactor System Design*, Marcel Dekker, New York, NY, 1995.

[31] L. Barsanti and P. Gualtieri, *Algae: Anatomy, Biochemistry, and Biotechnology*, CRC Press, Boca Raton, FL, 2005.

[32] C.U. Ugwu, H. Aoyagi, and H. Uchiyama, "Photobioreactors for mass cultivation of algae", *Bioresource Technology*, vol. 99, pp. 4021 – 4028, 2008.

[33] C. Posten, "Design principles of photo-bioreactors for cultivation of microalgae", *Engineering in Life Sciences*, vol. 9, pp. 165–177, 2009.

[34] B. Ke, *Photosynthesis, Photobiochemistry and Photobiophysics*, Kluwer Academic Publishers, Dordrecht, The Netherlands, 2001.

[35] E.H. Harris, *The Chlamydomonas Sourcebook - Volume 1*, Academic Press, San Diego, CA, 1989.

[36] M. Jonasz and G.R. Fournier, *Light Sscattering by Particles in Water: Theoretical and Experimental Foundations*, Academic Press, San Diego, CA, 2007.

[37] A. Melis, L. Zhang, M. Forestier, M.L. Ghirardi, and M. Seibert, "Sustained photobiological hydrogen gas production upon reversible inactivation of oxygen evolution in the green alga C*hlamydomonas reinhardtii*", *Plant Physiology*, vol. 117, pp. 129–139, 2000.

[38] J.E. Polle, S.D. Kanakagiri, and A. Melis, "tla1, a DNA insertional transformant of the green alga *Chlamydomonas reinhardtii* with a truncated light-harvesting chlorophyll antenna size", *Planta*, vol. 217, pp. 49–59, 2003.

[39] L. Pottier, J. Pruvost, J. Deremetz, J.-F. Cornet, J. Legrand, and C.G. Dussap, "A fully predictive model for one-dimensional light attenuation by C*hlamydomonas reinhardtii* in a torous photobioreactor", *Biotechnology and Bioengineering*, vol. 91, pp. 569–582, 2005.

[40] W.D.P. Stewart and P. Rowell, "Effects of l-methionine-dl-sulphoximine on the assimilation of newly fixed NH_3, acetylene reduction and heterocyst production in *Anabaena Cylindrica*", *Biochemical And Biophysical Research Communications*, vol. 65, pp. 846–856, 1975.

[41] D.O. Hall, S.A. Markov, Y. Watanabe, and K.K. Rao, "The potential applications of cyanobacterial photosynthesis for clean technologies", *Photosynthesis Research*, vol. 46, pp. 159–167, 1995.

[42] M.F. Modest, *Radiative Heat Transfer*, Academic Press, San Diego, CA, 2003.

[43] H. Berberoğlu and L. Pilon, "Experimental measurement of the radiation characteristics of *Anabaena variabilis* ATCC 29413-U and *Rhodobacter sphaeroides* ATCC 49419", *International Journal of Hydrogen Energy*, vol. 32, pp. 4772–4785, 2007.

[44] M. Jonasz and G.R. Fournier, *Light Sscattering by Particles in Water: Theoretical and Experimental Foundations*, Academic Press, San Diego, CA, 2007.

[45] A. Bricaud and A. Morel, "Light attenuation and scattering by phytoplanktonic cells: A theoretical modeling", *Applied Optics*, vol. 25, pp. 571–580, 1986.

[46] I.S. Suh and C.G. Lee, “Photobioreactor engineering: Design and performance”, *Biotechnology and Bioprocess Engineering*, vol. 8, pp. 313–321, 2003.

[47] N.J. Kim, I.S. Suh, B.K. Hur, and C.G. Lee, “Simple monodimensional model for linear growth rate of photosynthetic microorganisms in flat-plate photobioreactors”, *Journal of Microbiology and Biotechnology*, vol. 12, pp. 962–971, 2002.

[48] J. Sheehan, T. Dunahay, J. Benemann, and P. Roessler, “A look back at the u.s. department of energy’s aquatic species program - biodiesel from algae”, Tech. Rep. NREL/TP-580-24190, 1998.

[49] W. F. Herget and J. D. Brasher, “Remote measurement of gaseous pollutant concentrations using a mobile Fourier transform interferometer system”, *Applied Optics*, vol. 18, no. 20, pp. 3404–3420, 1979.

[50] N. Getoff, “Control of greenhouse gases emission by radiation-induced formation of useful products. utilization of CO_2”, *Radiation Physics and Chemistry*, vol. 75, no. 4, pp. 514 – 523, 2006.

[51] H. Berberoğlu, P.S. Gomez, and L. Pilon, “Radiation characteristics of *Botryococcus braunii*, *Chlorococcum littorale*, and *Chlorella sp.* used for CO_2 fixation and biofuel production”, *Journal of Quantitative Spectroscopy and Radiative Transfer*, vol. 110, pp. 1879–1893, 2009.

[52] M.P. Mengüç and R. Viskanta, “Radiative-transfer in 3-dimensional rectangular enclosures containing inhomogeneous, anisotropically scattering media”, *Journal of Quantitative Spectroscopy and Radiative Transfer*, vol. 33, pp. 533–549, 1985.

[53] R. Viskanta, “Computation of radiative transfer in combustion systems”, *International Journal of Numerical Methods for Heat & Fluid Flow*, vol. 18, no. 3/4, pp. 415–442, 2008.

[54] R. Viskanta and M. P. Mengüç, “Radiation heat transfer in combustion systems”, *Progress in Energy and Combustion Science*, vol. 13, no. 2, pp. 97–160, 1987.

[55] R. M. Huffaker, “Current research on infrared radiation from rocket exhaust”, *Journal of Quantitative Spectroscopy and Radiative Transfer*, vol. 8, no. 1, pp. 87 – 104, 1968.

[56] A.A. Alexeenko, N.E. Gimelshein, D.A. Levin, R.J. Collins, R.Rao, G.V. Candler, S.F. Gimelshein, J.D. Hong, and T.Schilling, “Modeling of flow and radiation in the Atlas plume”, *Journal of Thermophysics and Heat Transfer*, vol. 16, no. 1, 2002.

[57] K. N. Liou, *An Introduction to Atmospheric Radiation*, Academic Press, San Diego, CA, 2nd edition, 2002.

[58] M.K. Denison and B.W. Webb, "A spectral line-based weighted-sum-of-gray-gases model for arbitrary RTE solvers", *ASME Journal of Heat Transfer*, vol. 115, pp. 1004–1012, 1993.

[59] M.K. Denison and B.W. Webb, "An absorption-line blackbody distribution function for efficient calculation of total gas radiative transfer", *Journal of Quantitative Spectroscopy and Radiative Transfer*, vol. 50, no. 5, pp. 499–510, 1993.

[60] M.K. Denison and B.W. Webb, "Development and application of an absorption-line balckbody distribution function for CO_2", *International Journal of Heat and Mass Transfer*, vol. 38, no. 10, pp. 1813–1821, 1995.

[61] M.K. Denison and B.W. Webb, "The spectral line-based weighted sum of gray gases model in nonisothermal nonhomogeneous media", *ASME Journal of Heat Transfer*, vol. 117, pp. 359–365, 1995.

[62] L. S. Rothman, I. E. Gordon, A. Barbe, and D. Chris Benner *et al.*, "The HITRAN 2008 molecular spectroscopic database", *Journal of Quantitative Spectroscopy and Radiative Transfer*, vol. 110, no. 9-10, pp. 533–572, 2009.

[63] V.P. Solovjov and B.W. Webb, "SLW modeling of radiative transfer in multicomponent gas mixtures", *Journal of Quantitative Spectroscopy and Radiative Transfer*, vol. 65, no. 4, pp. 655–672, 2000.

[64] A.A. Lacis and V. Oinas, "A description of the correlated-k distribution method for medeling nongray gaseous absorption, thermal emmision, and multiple scattering in vertically inhomogeneous atomspheres", *Journal of Geophysical Research-Atomspheres*, vol. 96, pp. 9027–9063, 1991.

[65] A. Soufiani and J. Taine, "High temperature gas radiative property parameters of statistical narrow-band model for H_2O, CO_2 and CO, and correlated-k model for H_2O and CO_2", *International Journal of Heat and Mass Transfer*, vol. 40, no. 4, pp. 987–991, 1997.

[66] W.H. Reed and T.R. Hill, "Triangular mesh method for the neutron transport equation", Tech. Rep. LA-UR-73-479, Los Alamos Scientific Laboratory Report, Los Alamos, NM, 1973.

[67] J. Hesthaven and T. Warburton, *Nodal Discontinuous Galerkin Methods: Algorithms, Analysis, and Applications*, Springer, New York, NY, 2008.

[68] X. Cui and B.Q. Li, "A discontinuous finite-element formulation for multidimensional radiative transfer in absorbing, emitting, and scattering media", *Numerical Heat Transfer Part B-Fundamentals*, vol. 46, pp. 399–428, 2004.

[69] C. Aussourd, “Styx: A multidimensional AMR S_n scheme”, *Nuclear Science and Engineering*, vol. 143, pp. 281–290, 2003.

[70] C. Fuhrer and R. Rannacher, “Error analysis for the finite element approximation of a radiative transfer model”, *RAIRO Mathematical Modeling and Numerical Analysis*, vol. 30, pp. 743–762, 1996.

[71] J.M. Zhao and L.H. Liu, “Discontinuous spectral element method for solving radiative heat transfer in multidimensional semitransparent media”, *Journal of Quantitative Spectroscopy and Radiative Transfer*, vol. 107, pp. 1–16, 2007.

[72] A. Klockner, T. Warburton, J. Bridge, and J.S. Hesthaven, “Nodal discontinuous Galerkin methods on graphics processors”, *Journal of Computational Physics*, vol. 228, no. 21, pp. 7863–7882, 2009.

[73] X. Cui and B.Q. Li, “Discontinuous finite element solution of 2-D radiative transfer with and without axisymmetry”, *Journal of Quantitative Spectroscopy and Radiative Transfer*, vol. 96, pp. 383–407, 2005.

[74] A.T. Patera, “A spectral element method for fluid dynamics laminar-flow in a channel expansion”, *Journal of Computational Physics*, vol. 54, pp. 468–488, 1984.

[75] O. Balima, A. Charette, and D. Marceau, “Comparison of light transport models based on finite element and the discrete ordinates methods in view of optical tomography applications”, *Journal of Computational and Applied Mathematics*, vol. 234, no. 7, pp. 2259–2271, 2010.

[76] O. Balima, Y. Favennec, J. Boulanger, and A. Charette, “Optical tomography with the discontinuous galerkin formulation of the radiative transfer equation in frequency domain”, *Journal of Quantitative Spectroscopy and Radiative Transfer*, vol. 113, no. 10, pp. 805–814, 2012.

[77] N. Bell and M. Garland, “Efficient sparse matrix-vector multiplication on CUDA”, *NVIDIA Technical Report*, 2008.

[78] E. Elsen, P. LeGresley, and E. Darve, “Large calculation of the flow over a hypersonic vehicle using a GPU”, *Journal of Computational Physics*, vol. 227, pp. 10148–10161, 2008.

[79] A. Corrigan, F. Camelli, R. Lohner, and J. Wallin, “Running unstructured grid-based CFD solvers on modern graphics hardware”, *International Journal for Numerical Methods in Fluids*, vol. 66, pp. 221–229, 2011.

[80] E.H. Phillips, Y.Zhang, R.L. Davis, and J.D. Owens, "Rapid aerodynamic performance prediction on a cluster of graphics processing units", *Proceedings of the 49th AIAA Aerospace Sciences Meeting and Exhibit*, vol. 565, 2009.

[81] NVIDIA Corporation, *CUDA Computed Unified Device Architecture, Programming Guide, version 2.2*, 2009.

[82] R. Barrett, M. Berry, T.F. Chan, J. Demmel, J. Donato, J. Dongarra, V. Eijkhout, R. Pozo, C. Romine, and H. Van der Vorst, *Templates for the Solution of Linear Systems: Building Blocks for Iterative Methods, 2nd Edition*, SIAM,Philadelphia, PA, 1994.

[83] Y. Saad, *Iterative Methods for Sparse Linear Systems*, SIAM, Philadelphia, PA, 2003.

[84] F.H. Lee, K.K. Phoon, K.C. Lim, and S.H. Chan, "Performance of Jacobi preconditioning in Krylov subspace solution of finite element equations", *International Journal for Numerical and Analytical Methods in Geomechanics*, vol. 26, no. 4, pp. 341–372, 2002.

[85] Khronos OpenCL Working Group, "The OpenCL Specification, version 1.0.29.2008", URL: http://khronos.org/registry/cl/specs/opencl-1.0.29.pdf.

[86] D.N. Trivic and C.H. Amon, "Modeling the 3-D radiation of anisotropically scattering media by two different numerical methods", *International Journal of Heat and Mass Transfer*, vol. 51, pp. 2711–2732, 2008.

[87] P.J. Coelho, J.M. Goncalves, M.G. Carvalho, and D.N. Trivic, "Modeling of radiative heat transfer in enclosures with obstacles", *International Journal of Heat and Mass Transfer*, vol. 41, no. 4-5, pp. 745–756, 1998.

[88] D.Y. Byun, S.W. Baek, and M.Y. Kim, "Investigation of radiative heat transfer in complex geometries using blocked-off, multiblock, and embedded boundary treatments", *Numerical Heat Transfer, Part A*, vol. 43, pp. 807–825, 2003.

[89] G. Mie, "Beiträge zur Optik trüber Medien, speziell kolloidaler Metallösungen", *Annalen der Physik*, vol. 25, pp. 377–445, 1908.

[90] M. I. Mishchenko and L. D. Travis, "Capabilities and limitations of a current fortran implementation of the t-matrix method for randomly oriented, rotationally symmetric scatterers", *Journal of Quantitative Spectroscopy and Radiative Transfer*, vol. 60, pp. 309–324, 1998.

[91] K.J. Daniel, N.M. Laurendeau, and F.P. Incropera, “Prediction of radiation absorption and scattering in turbid water bodies”, *ASME Journal of Heat Transfer*, vol. 101, pp. 63–67, 1979.

[92] B.M. Agrawal and M.P. Mengüç, “Forward and inverse analysis of single and multiple scattering of collimated radiation in an axisymmetric system”, *International Journal of Heat and Mass Transfer*, vol. 34, pp. 633–647, 1991.

[93] D. Stramski and C.D. Mobley, “Effect of microbial particles on oceanic optics: a database of single-particle optical properties”, *Limnology and Oceanography*, vol. 42, pp. 538–549, 1997.

[94] R.R. Bidigare, R.C. Smith, K.S. Baker, and J. Marra, “Oceanic primary production estimates from measurements of spectral irradiance and pigment concentrations”, *Global Biogeochemical Cycles*, vol. 1, pp. 171–186, 1987.

[95] A. Quirantes and S. Bernard, “Light scattering by marine algae: two-layer spherical and nonspherical models”, *Journal of Quantitative Spectroscopy and Radiative Transfer*, vol. 89, pp. 311–321, 2004.

[96] S. Bernard, T.A. Probyn, and R.G. Barlow, “Measured and modelled optical properties of particulate matter in the southern benguela”, *South African Journal of Science*, vol. 97, pp. 410–420, 2001.

[97] D. Stramski, A. Bricaud, and A. Morel, “Modeling the inherent optical properties of the ocean based on the detailed composition of planktonic community”, *Applied Optics*, vol. 40, pp. 2929–2945, 2001.

[98] C.F. Bohren and D.R. Huffman, *Absorption and scattering of light by small particles*, John Wiley & Sons, New York, 1998.

[99] H.C. Van De Hulst, *Light Scattering by Small Particles*, Wiley, New York, NY, 1957.

[100] A. Bricaud, J. Ronald, V. Zaneveld, and J.C. Kitchen, “Backscattering efficiency of coccolithophorids: use of a three-layered sphere model”, *Proceedings of SPIE*, vol. 1750, pp. 27–33, 1992.

[101] J. Ronald, V. Zaneveld, and J.C. Kitchen, “The variation in the inherent optical properties of phytoplankton near an absorption peak as determined by various models of cell structure”, *Proceedings of SPIE*, vol. 100, pp. 13309–13320, 1995.

[102] M.I. Mishchenko, J.W. Hovenier, and L.D. Travis, *Light Scattering by Nonspherical Particles*, Academic Press, San Diego, CA, 2000.

[103] A. Bricaud, A.L. Bédhomme, and A. Morel, "Optical properties of diverse phytoplanktonic species: experimental results and theoretical interpretation", *Journal of Plankton Research*, vol. 10, pp. 851–873, 1988.

[104] A. Morel and Y.H. Ahn, "Optics of heterotrophic nanoflagellates and ciliates: a tentative assessment of their scattering role in oceanic waters compared to those of bacterial and algal cells", *Journal of Marine Research*, vol. 49, pp. 177–202, 1991.

[105] D. Stramski, A. Morel, and A. Bricaud, "Modeling the light attenuation and scattering by spherical phytoplanktonic cells: a retrieval of the bulk refractive index", *Applied Optics*, vol. 27, pp. 3954–3957, 1988.

[106] F.D. Bryant, B.A. Seiber, and P. Latimer, "Absolute optical cross sections of cells and chloroplasts", *Archives of Biochemistry and Biophysics*, vol. 135, pp. 79–108, 1969.

[107] R.E. Green, H.M. Sosik, R.J. Olson, and M.D. Durand, "Flow cytometric determination of size and complex refractive index for marine particles: comparison with independent and bulk estimates", *Applied Optics*, vol. 42, pp. 526–541, 2003.

[108] R.W. Spinrad and J.F. Brown, "Relative real refractive index of marine microorganisms: a technique for flow cytometric stimation", *Applied Optics*, vol. 25, pp. 1930–1934, 1986.

[109] P. Gerhardt, T. C. Beaman, T. R. Corner, J. T. Greenamyre, and L. S. Tisa, "Photometric immersion refractometry of bacterial spores", *Journal of Bacteriology*, vol. 150, pp. 643–648, 1982.

[110] M. Jonasz, G. Fournier, and D. Stramski, "Photometric immersion refractometry: a method for determining the refractive index of marine microbial particles from beam attenuation", *Applied Optics*, vol. 36, pp. 4214–4225, 1997.

[111] R. Barer and S. Joseph, "Refractometry of living cells. part I: Basic principles", *Quarterly Journal of Microscopical Science*, vol. 96, pp. 399–423, 1954.

[112] M.D. DuRand and R.J. Olson, "Diel patterns in optical properties of the chlorophyte *Nannochloris sp.*: Relating individual-cell to bulk measurements", *Limnology and Oceanography*, vol. 43, pp. 1107–1118, 1998.

[113] J.-F. Cornet, C.G. Dussap, and G. Dubertret, "A structured model for simulation of cultures of the cyanobacterium *Spirulina platensis* in photobioreactors: I. Coupling between light transfer and growth kinetics", *Biotechnology and Bioengineering*, vol. 40, pp. 817–825, 1992.

[114] J.-F. Cornet, C.G. Dussap, J.B. Gross, C. Binois, and C. Lasseur, "A simplified monodimensional approach for modeling coupling between radiant light transfer and growth kinetics in photobioreactors", *Chemical Engineering Science*, vol. 50, pp. 1489–1500, 1995.

[115] L. J. Wang and C. L. Weller, "Recent advances in extraction of nutraceuticals from plants", *Trends in Food Science & Technology*, vol. 17, pp. 300–312, 2006.

[116] A. Hosikian, S. Lim, R. Halim, and M. K. Danquah, "Chlorophyll extraction from microalgae: A review on the process engineering aspects", *International Journal of Chemical Engineering*, vol. 2010, pp. 11, 2010.

[117] R.J. Porra, W.A. Thompson, and P.E. Kriedemann, "Determination of accurate extinction coefficients and simultaneous equations for assaying chlorophylls a and b extracted with four different solvents: verification of the concentration of chlorophyll standards by atomic absorption spectroscopy", *Biochimica et Biophysica Acta (BBA) - Bioenergetics*, vol. 975, pp. 384 – 394, 1989.

[118] R. Ritchie, "Consistent sets of spectrophotometric chlorophyll equations for acetone, methanol and ethanol solvents", *Photosynthesis Research*, vol. 89, pp. 27–41, 2006.

[119] L.M. Duysens, "The flattening of the absorption spectra of suspensions as compared to that of solutions", *Biochimica et Biophysica Acta*, vol. 19, pp. 1–12, 1956.

[120] A. Quirantes and S. Bernard, "Light-scattering methods for modelling algal particles as a collection of coated and/or nonspherical scatterers", *Journal of Quantitative Spectroscopy and Radiative Transfer*, vol. 100, pp. 315–324, 2006.

[121] M.E. Baird, "Numerical approximations of the mean absorption cross-section of a variety of randomly oriented microalgal shapes", *Journal of Mathmatical Biology*, vol. 47, pp. 325–336, 2003.

[122] W.S. Rasband, "Image j", U.S. National Institute of Health, Bethesda, Maryland, USA, http://rsb.info.nih.gov/ij/, 1997-2007.

[123] H. Berberoğlu, J. Yin, and L. Pilon, "Simulating light transfer in a bubble sparged photobioreactor for simultaneous hydrogen fuel production and CO_2 mitigation", *International Journal of Hydrogen Energy*, vol. 32, pp. 2273–2285, 2007.

[124] E. Eroglu and A. Melis, ""density equilibrium" method for the quantitative and rapid in situ determination of lipid, hydrocarbon, or biopolymer content

in microorganisms", *Biotechnology and Bioengineering*, vol. 102, pp. 1406–1415, 2009.

[125] T. Baeck, *Genetic Algorithms in Theory and Practice*, The Oxford University Press, Oxford, UK, 1996.

[126] P. Charbonneau, "Genetic algorithms in astronomy and astrophysics", *The Astrophysical Journal*, vol. 101, pp. 309, 1995.

[127] P. Charbonneau and B. Knapp, "A User's guide to PIKAIA 1.0", Tech. Rep. NCAR Technical Note 418+IA, National Center for Atmospheric Research, 1995.

[128] P. Charbonneau, "An Introduction to Genetic Algorithms for Numerical Optimization", Tech. Rep. NCAR Technical Note 450+IA, National Center for Atmospheric Research, 2002.

[129] P. Charbonneau, "Release Notes for PIKAIA 1.2", Tech. Rep. NCAR Technical Note 451+STR, National Center for Atmospheric Research, 2002.

[130] A. Morel and A. Bricaud, "Inherent optical properties of algal cells including picoplankton: Theoretical and experimental results", *In Photosynthetic picoplankton. Can. Bull. Fish. Aquat. Sci.*, pp. 521–560, 1986.

[131] O. Zhernovaya, O. Sydoruk, V. Tuchin, and A. Douplik, "The refractive index of human hemoglobin in the visible range", *Physics in Medicine and Biology*, vol. 56, pp. 4013–4021, 2011.

[132] G.M. Hale and M.R. Querry, "Optical constants of water in the 200-nm to 200-μm wavelength region", *Applied Optics*, vol. 12, pp. 555–563, 1973.

[133] X. Ma, J.Q. Lu, R.S. Brock, K.M. Jacobs, P. Yang, and H.H. Hu, "Determination of complex refractive index of polystyrene microspheres from 370 to 1610 nm", *Physics of Medical Biology*, vol. 48, pp. 4165–4172, 2003.

[134] I. D. Nikolov and C. D. Ivanov, "Optical plastic refractive measurements in the visible and the near-infrared regions", *Applied Optics*, vol. 39, pp. 2067–2070, 2000.

[135] D.W. Mackowski and M.I. Mishchenko, "Calculation of the t matrix and the scattering matrix for ensembles of spheres", *Journal of the Optical Society of Americal A*, vol. 13, pp. 2266–2278, 1996.

[136] D.W. Mackowski, "Calculation of total cross sections of multiple-sphere clusters", *Journal of the Optical Society of Americal A*, vol. 11, no. 11, pp. 2851–2861, 1994.

[137] H.A. Yousif and E. Boutros, "A FORTRAN code for the scattering of EM plane waves by an infinitely long cylinder at oblique incidence", *Computer Physics Communications*, vol. 69, pp. 406 – 414, 1992.

[138] S.C.Lee, "Scattering phase function for fibrous media", *International Journal of Heat and Mass Transfer*, vol. 33, pp. 2183–2190, 1990.

[139] J. Pruvost, J. Legrand, P. Legentilhomme, and A. Muller-Feuga, "Simulation of microalgae growth in limiting light conditions: Flow effect", *AIChE Journal*, vol. 48, pp. 1109–1120, 2002.

[140] F.G. Acién Fernández, F. García Camacho, J.A. Sánchez Pérez, J.M. Fernández Sevilla, and E. Molina Grima, "A model for light distribution and average solar irradiance inside outdoor tubular photobioreactors for the microalgal mass culture", *Biotechnology and Bioengineering*, vol. 55, pp. 701–714, 1997.

[141] J.-F. Cornet, C.G. Dussap, P. Cluzel, and G. Dubertret, "A structured model for simulation of cultures of the cyanobacterium *Spirulina platensis* in photobioreactors: II. Identification of kinetic parameters under light and mineral limitations", *Biotechnology and Bioengineering*, vol. 40, pp. 826–834, 1992.

[142] Z.C. Wheaton and G. Krishnamoorthy, "Modeling radiative transfer in photobioreactors for algal growth", *Computers and Electronics in Agriculture*, vol. 87, pp. 64 – 73, 2012.

[143] S. Aiba, "Growth kinetics of photosynthetic microorganisms", *Advances in Biochemical Engineering/Biotechnology*, vol. 23, pp. 85–156, 1982.

[144] J. Dauchet, S. Blanco, J.-F. Cornet, M. El Hafi, V. Eymet, and R. Fournier, "The practice of recent radiative transfer Monte Carlo advances and its contribution to the field of microorganisms cultivation in photobioreactors", *Journal of Quantitative Spectroscopy and Radiative Transfer*, pp. –, 2012.

[145] J. Pruvost, J. F. Cornet, V. Goetz, and J. Legrand, "Theoretical investigation of biomass productivities achievable in solar rectangular photobioreactors for the cyanobacterium arthrospira platensis", *Biotechnology Progress*, vol. 28, pp. 699–714, 2012.

[146] X. He, E. Lee, L. Wilcox, R. Munipalli, and L. Pilon, "A high-order accurate GPU-based radiative transfer equation solver for combustion and propulsion applications", *Numerical Heat Transfer Part B-fundamentals*, 2012 (accepted).

[147] J.S. Hesthaven and L. Koblinger, *Nodal Discontinuous Galerkin Methods: Algorithms, Analysis, and Applications*, Springer, New York, NY, 2007.

[148] I.J. Dunn, E. Heinzle, J. Ingham, and J.E. Prenosil, *Biological Reaction Engineering: Dynamic Modelling Fundamentals with Simulation Examples*, Wiley-VCH, 2^{nd} edition, 2003.

[149] E.M. Grima, J.M.F. Sevilla, J.A.S. Perez, and F.G. Camacho, "A study on simultaneous photolimitation and photoinhibition in dense microalgal cultures taking into account incident and averaged irradiances", *Journal of Biotechnology*, vol. 45, pp. 59 – 69, 1996.

[150] M.J. Barbosa, J. Hoogakker, and R.H. Wijffels, "Optimisation of cultivation parameters in photobioreactors for microalgae cultivation using the A-stat technique", *Biomolecular Engineering*, vol. 20, pp. 115–123, 2003.

[151] J.A. Asenjo and J.C. Merchuk, *Bioreactor System Design*, Marcel Dekker, New York, NY, 1995.

[152] J.F. Cornet and J. Albiol, "Modeling photoheterotrophic growth kinetics of *Rhodospirillum rubrum* in rectangular photobioreactors", *Biotechnology Progress*, vol. 16, pp. 199–207, 2000.

[153] J.F. Cornet and C.G. Dussap, "A simple and reliable formula for assessment of maximum volumetric productivities in photobioreactors", *Biotechnology Progress*, vol. 25, pp. 424–435, 2009.

[154] T.E. Murphy and H. Berberoğlu, "Effect of algae pigmentation on photobioreactor productivity and scale-up: A light transfer perspective", *Journal of Quantitative Spectroscopy and Radiative Transfer*, vol. 112, pp. 2826 – 2834, 2011.

[155] R.J. Geider, H.L. MacIntyre, and T.M. Kana, "A dynamic model of photoadaptation in phytoplankton", *Limnology and Oceanography*, vol. 41, pp. 1–15, 1996.

[156] Q. Huang, L. Yao, T. Liu, and J. Yang, "Simulation of the light evolution in an annular photobioreactor for the cultivation of *Porphyridium cruentum*", *Chemical Engineering Science*, vol. 84, pp. 718 – 726, 2012.

[157] A. Muller-Feuga, R. Le Guédes, and J. Pruvost, "Benefits and limitations of modeling for optimization of *Porphyridium cruentum* cultures in an annular photobioreactor", *Journal of Biotechnology*, vol. 103, pp. 153 – 163, 2003.

[158] H. Takache, G. Christophe, J.-F. Cornet, and J. Pruvost, "Experimental and theoretical assessment of maximum productivities for the microalgae chlamydomonas reinhardtii in two different geometries of photobioreactors", *Biotechnology Progress*, vol. 26, pp. 431–440, 2010.

[159] H. Berberoğlu and L. Pilon, "Maximizing solar to H_2 energy conversion efficiency of outdoor photobioreactors using mixed cultures", *International Journal of Hydrogen Energy*, vol. 35, pp. 500–510, 2010.

[160] E. Lee, R.-L. Heng, and L. Pilon, "Spectral optical properties of selected photosynthetic microalgae producing biofuels", *Journal of Quantitative Spectroscopy and Radiative Transfer*, vol. 114, pp. 122 – 135, 2013.

[161] C. Gueymard, "Smarts code, version 2.9.2 user's direct beam spectral irradiance data for photovoltaic cell manual", Solar Consulting Services, URL = http://rredc.nrel.gov/solar/models/SMARTS, 2002.

[162] W.A. Fiveland and R.A. Wessel, "Numerical model for predicting performance of three-dimensional pulverized-fuel fired furnaces", *ASME Journal of Engineering for Gas Turbines and Power*, vol. 110, pp. 117–126, 1988.

[163] E.H. Chui and G.D. Raithby, "Computation of radiant-heat transfer on a nonorthogonal mesh using the finite-volume method", *Numerical Heat Transfer Part B-Fundamentals*, vol. 23, pp. 269–288, 1993.

[164] H.-S. Li, G. Flamant, and J.-D. Lu, "A new discrete ordinate algorithm for computing radiative transfer in one-dimensional atmospheres", *Journal of Quantitative Spectroscopy and Radiative Transfer*, vol. 83, pp. 407–421, 2004.

[165] A. Morel and R.C. Smith, "Relation between total quanta and total energy for aquatic photosynthesis", *Limnology and Oceanography*, vol. 19, pp. 591–600, 1974.

[166] H. Takache, J. Pruvost, and J.-F. Cornet, "Kinetic modeling of the photosynthetic growth of *Chlamydomonas reinhardtii* in a photobioreactor", *Biotechnology Progress*, vol. 28, no. 3, pp. 681–692, 2012.

[167] D. Chaumont, "Biotechnology of algal biomass production: a review of systems for outdoor mass culture", *Journal of Applied Phycology*, vol. 5, pp. 593–604, 1993.

[168] V. Goetz, F. Le Borgne, J. Pruvost, G. Plantard, and J. Legrand, "A generic temperature model for solar photobioreactors", *Chemical Engineering Journal*, vol. 175, pp. 443 – 449, 2011.

[169] J. Sheng, H.W. Kim, J.P. Badalamenti, C. Zhou, S. Sridharakrishnan, R. Krajmalnik-Brown, B.E. Rittmann, and R. Vannela, "Effects of temperature shifts on growth rate and lipid characteristics of synechocystis sp. pcc6803 in a bench-top photobioreactor", *Bioresource Technology*, vol. 102, pp. 11218 – 11225, 2011.